

UNDERSTANDING SATELLITE GALAXIES THROUGH THE KINEMATICS  
OF THE SMALL MAGELLANIC CLOUD IN THE AGE OF HST AND GAIA

Paul Jeffrey Zivick  
Lynchburg, Virginia

B.S. Astronomy & Astrophysics, The Ohio State University, 2011

M.S. Astronomy, University of Virginia, 2013

A Dissertation Presented to the Graduate  
Faculty of the University of Virginia  
in Candidacy for the Degree of  
Doctor of Philosophy

Department of Astronomy

University of Virginia  
May 2020

Committee Members:

Nitya J. Kallivayalil  
Steven R. Majewski  
Shane W. Davis  
David A. Nichols

© Copyright by  
Paul Jeffrey Zivick  
All rights reserved  
April 15, 2020

## Abstract

With the advent of modern all-sky surveys, the number of known Milky Way (MW) satellite galaxies has expanded well beyond the original eleven classical satellites. One key use of this catalog of objects has been to test predictions of cosmological cold dark matter simulations on the smallest scales in the universe. However, these tests rely on modeling of the density profiles of the satellite galaxies. To build the most accurate model, three dimensional motions of the stars in the satellite are required, a measurement only now becoming possible with the new era of precision astrometry, led by work with the Hubble Space Telescope (HST) and the Gaia Space Telescope. We use data from both of these observatories to study one of the brightest nearby satellites, the Small Magellanic Cloud (SMC), to both understand its own history with the MW and its companion the Large Magellanic Cloud (LMC) and develop a novel kinematic modeling technique for application to the broader MW satellite population.

Given the SMC's irregular nature and large spatial extent across the sky, we require broad spatial sampling to thoroughly study its kinematics. To provide this, we observe 30 new fields in the SMC using HST, producing a new proper motion catalog for analysis. Using this catalog, we improve the known systemic motion of the SMC and constrain the minimum separation distance in its last interaction with the LMC to roughly 7 kpc. This places the center of the SMC passing directly through the disk of the LMC, indicating a highly turbulent interaction. Internal kinematics reveal coherent outward motion in the southeastern side of the SMC in the direction of the Magellanic Bridge, consistent with the scenario of ongoing tidal disruption.

The Gaia Data Release 2 (DR2) expanded our proper motion catalogs to well over a billion stars across the MW with proper motions, including many thousands

in the direction of the Magellanic Clouds. We use this database to present the first kinematic characterization of the stellar component of the Magellanic Bridge. This analysis reveals in the young stars a roughly linearly increasing relative motion from the SMC towards the LMC, at velocities above 100 km/s, suggesting an active outflow of stars (and gas) from the SMC towards the LMC. We compare these kinematics against numerical simulations of the interactions between the SMC and LMC and find good agreement for a recent direct collision scenario, consistent with our original HST work.

However, significant uncertainties remain in our understanding of the full internal kinematics of the SMC. We present a new analysis of this system using the large DR2 catalog, attempting to account for both possible coherent rotation within the SMC and a tidal expansion component due to the LMC, as suggested by both our Bridge and earlier HST results. To capture the full 3D information present in the observations (as the proper motions are measured for stars at varying depths along the line of sight), we generate a toy 3D model of the SMC and create mock data for comparisons to the DR2 catalog. We find a need for an updated center of mass location and systemic motion for the older stellar population compared to earlier averaged measurements for the SMC, with the older stars located further from the LMC and moving away from the LMC faster than the younger stars. Taken together, we can understand this as a Bullet Cluster-like scenario where existent old stellar populations in the SMC and LMC passed through relatively unscathed while the gas violently collided, imparting different kinematics on the stars formed post-interaction. Intriguingly, we find a need for a non-zero rotation throughout much of the SMC, at a relatively high inclination angle, in addition to accounting for the tidal expansion in the SMC RGs caused by recent interactions with the LMC.

We present a similar analysis for the red supergiant (RSG) population in the SMC, whose age closely coincides with the time of last interaction between the SMC and LMC. We find compelling evidence for the existence of coherent rotation in a subpopulation of the RSGs, potentially mapping onto a previously measured age bimodality in the SMC Classical Cepheid population. The rotation signal appears when the internal kinematics are studied assuming the systemic properties for the SMC RG population, suggesting that the gas within the SMC may have been relatively unperturbed before the most recent interaction. The small area of rotation may also provide new leverage on improving the constraints on the mass ratios of the Magellanic system as it could place a hard boundary on where the gas remained fully bound to the SMC.

Taken as a whole, the analysis of the SMC has led to the creation of a modeling framework capable of accounting for compounding kinematic mechanisms (like rotation and tidal expansion) and developing intuition for understanding the broader MW satellite population in a truly 3D manner.

## Acknowledgements

*"I don't know. You tell me, Paul."*

*- Matt Pryal*

First, I would like to acknowledge the traditional custodians of the land on which UVa and the Department of Astronomy is built, the Monacan Nation, and pay my respects to their elders past and present.

For my personal acknowledgements, it has to start with my family, without whom none of this would have been possible. Grandmom and Granddad, you two have been a never ending source of support and love, and I know I wouldn't be here without it. David, I can't imagine there's a stepdad out there who has done a better or more earnest job making a stepson feel like a real son, and I count my lucky stars I get to be that stepson. Dad, I blame you for accidentally starting me down the astronomy path when you talked about your new job at NRAO all those many years ago, and I can't thank you enough for innumerable phone calls filled with impossibly sage advice. Mom, I'm still not sure who was more excited when I decided to come back to Virginia for graduate school, but I can't imagine the last five years playing out any differently. No matter how impossible life/grad school/whatever may have seemed, knowing I could hop in the car and have dinner at home has meant more to me than I could possibly put into words.

Of course family can mean more than just people related by blood, so I have to thank my Charlottesville family for the love and support over these last five years. Sean and Molly, it has been wonderful sharing a beer and conversation on countless relaxed nights with y'all. Spider Robby, I'm not sure I've ever bonded so quickly with a friend over the course of a single night, and it's been a true pleasure seeing that bond grow these past four years. Brian, it's hard to believe we've lived together for

five years, through compromise chairs, unexpected dogs, and all. Knowing that I had a constant friend and roommate certainly made grad school a smoother experience than it would've otherwise been. Rudy, I know you're up in Harrisonburg so it doesn't quite count, but it has been an incredible joy reconnecting over a love of competitive card games and board games along with some fairly spontaneous travel experiences (looking at you, Denver). Thankful and Riley (and Ezreal too), I've lost track of how much time I have spent at your home, and I know I'll never be able to fully repay you for the warmth and acceptance you have shown me. Matt, one day we're going to start that podcast, and it'll be an Spotify chart topper. And if we never do, then we will still have had some truly life-affirming conversations over a beer or two at Nelly's. And Katrina, you joined this party a little later than the others, but I can't imagine having finished grad school without you there with me every step of the way nor can I envision being this excited to move to Texas without you. Academia might be a crazy journey, but I can't think of a better copilot to navigate it with.

Thank you to all of the grad students in the department, both past and present, who helped to make it a welcoming environment. Thank you to my fantastic cohort with our (optimistically) monthly dinners and support among each other. Thank you to far too many other incredible folks that I've met here in Charlottesville to name. Whether that has been Courtney's cabin trips (with more people than I thought could go to a cabin), to Lauren spearheading unforgettable trips to Foxfield, to Trey talking about other Jupiter, all of you wonderful people have left an indelible mark on me.

Professionally, I have to start with my incredible advisor, Nitya. I still remember the feeling of excitement I felt listening to you talk about the research projects you envisioned for the group when I visited as a prospective student. It was that same excitement which made the choice to come to UVa an easy one (and that pushed

me to email you only a few weeks after accepting about joining the group). I think I can say with some degree of confidence that not every advisor would want their third year grad student to fly across the country to Los Angeles then entrust them with a major role on a significant and time sensitive paper (*Gaia* DR2, what a time). Looking back, that experience, that excitement around racing to finish our analysis, has formed a foundational part of my graduate school experience. Truly, whether as an astronomer, a mentor, a communicator, a professional, or one of the other countless roles I have seen you in, you have been beyond an exemplary model that I can only hope to follow.

As a (deeply) non-exhaustive list of other folks who have had a significant impact upon my career: Roeland, thank you for your always invaluable insights into both the science and the framing of the science for readers and TACs (not to mention the way-too-many letters of recommendation for postdoc applications). Gurtina, thank you for your support and encouragement across the many papers and projects (and also for the way-too-many letters too). Gail and Rachael, thank you for shepherding a young high school student who knew absolutely nothing about astronomy onto a path to becoming an actual astronomer. Tobias, thank you for ingraining into a young grad student the importance of being careful with statistics and errors (even if I may still slip up from time to time). Tony and all the fantastic HSTPROMO folks, thank you for your support and patience with a steady stream coding and *HST*-related questions. Hannah, it's been truly rewarding working with you in Nitya's group, and I know you will excel next year when you become the senior grad student in the group! Thank you to the rest of my thesis committee, Steve and Shane, who have been a great source of feedback and advice in guiding the arc of my PhD. Thank you to the folks across Grounds that I've had the chance to work with through Grad Council or

GPC work. I wasn't expecting to learn more about higher education administration in graduate school, but I'm certainly glad I did. And a monumental thank you to all the folks in the department, from David and his Herculean efforts in keeping the department IT running to Whitney and her organizing so many wonderful events in the department, we are lucky to have so many folks who make the department better in countless ways each day.

Now I believe I have run more than a bit over for what an acknowledgements section ought to be, so I will finish by saying thank you to the reader about to open this thesis. As a fair warning, you may become sick of the words "satellite" and "kinematics" by the end of this, but I hope you find it thought-provoking (or at least passably interesting).

# Table of contents

<b>List of Figures</b>	<b>xix</b>
<b>List of Tables</b>	<b>xx</b>
<b>1 Introduction</b>	<b>1</b>
1.1 Milky Way Satellites . . . . .	1
1.1.1 Background . . . . .	1
1.1.2 Implications for $\Lambda$ CDM . . . . .	2
1.1.3 Measuring MW Satellite Kinematics . . . . .	6
1.2 The Magellanic Clouds . . . . .	7
1.3 The Small Magellanic Cloud . . . . .	10
<b>2 The Proper Motion Field of the Small Magellanic Cloud: Kinematic Evidence for its Tidal Disruption</b>	<b>13</b>
2.1 Introduction . . . . .	14
2.2 Data & Analysis . . . . .	17
2.2.1 Description of Observations . . . . .	17
2.2.2 Analysis of WFC3/UVIS Observations . . . . .	18
2.2.3 Two Epoch Results . . . . .	23
2.3 Proper Motion Results . . . . .	27
2.3.1 Model Design & Analysis . . . . .	27
2.3.2 Center of Mass Results . . . . .	32
2.4 Internal Kinematics . . . . .	33
2.4.1 Full Star Sample . . . . .	33
2.4.2 Red vs Blue Stellar Motion . . . . .	39
2.5 Orbit Implications . . . . .	40
2.5.1 Methodology . . . . .	43
2.5.2 Impact parameter and timing of the last SMC-LMC encounter	45
2.6 Discussion & Conclusions . . . . .	48
2.6.1 Conclusions for PMs . . . . .	48
2.6.2 Conclusions for Implied Orbit . . . . .	50
2.6.3 Future Work . . . . .	51

<b>3</b>	<b>The Proper Motion Field Along the Magellanic Bridge: a New Probe of the LMC-SMC Interaction</b>	<b>55</b>
3.1	Introduction . . . . .	56
3.2	Data Selection . . . . .	58
3.2.1	<i>Gaia</i> DR2 Data . . . . .	58
3.2.2	<i>HST</i> Data . . . . .	61
3.3	Data Analysis & Model Comparisons . . . . .	64
3.3.1	Data Analysis . . . . .	64
3.3.2	H I and Stellar Comparisons . . . . .	67
3.3.3	Model Comparisons . . . . .	69
3.4	Discussion & Conclusions . . . . .	71
<b>4</b>	<b>Deciphering the Kinematic Structure of the Small Magellanic Cloud through its Red Giant Population</b>	<b>85</b>
4.1	Introduction . . . . .	86
4.2	Data Selection . . . . .	90
4.2.1	Gaia DR2 Selection . . . . .	90
4.2.2	Radial Velocity Cross-Matching . . . . .	93
4.3	Data Analysis . . . . .	97
4.3.1	Observational Data . . . . .	97
4.3.2	Mock Data Creation . . . . .	100
4.3.3	Comparison Quantification . . . . .	106
4.4	Model-to-Data Comparison Results . . . . .	109
4.4.1	Best-fit Results . . . . .	109
4.4.2	Existing Proposed Scenarios . . . . .	111
4.5	Conclusions and Discussion . . . . .	115
<b>5</b>	<b>Exploring the Kinematics of the “Young” Stars of the Small Magellanic Cloud</b>	<b>121</b>
5.1	Introduction . . . . .	122
5.2	Data Selection . . . . .	125
5.2.1	Gaia DR2 Selection . . . . .	125
5.2.2	Radial Velocity Cross-Matching . . . . .	128
5.3	Data Analysis . . . . .	130
5.3.1	Systemic Properties . . . . .	130
5.3.2	Internal Kinematics . . . . .	131
5.3.3	Radial Velocity Structure . . . . .	135
5.4	Implications and Future Work . . . . .	139
<b>6</b>	<b>Summary</b>	<b>144</b>
6.1	Satellites in a New Age of Astrometry . . . . .	144
6.2	Outstanding $\Lambda$ CDM Challenges . . . . .	147

# List of Figures

1.1	Distribution of known MW satellites. This image is from a movie produced by Marcel S. Pawlowski for Bullock & Boylan-Kolchin (2017)	3
1.2	The Large Magellanic Cloud can be seen to the upper right of the Milky Way, and the Small Magellanic Cloud can be seen on the far right side of the image. <i>Credit:ESO/H. Stockebrand</i> . . . . .	9
2.1	B-band image covering $4^\circ \times 6^\circ$ from the Digital Sky Survey of the SMC (with 47 Tuc to the right) where north is up and east is to the left in the image. The LMC, northeast of the SMC, is located off the panel to the upper left. The green circles indicate the locations of our new reference QSOs from Kozłowski et al. (2013). The cyan squares show the quasars used in NK13 and Kallivayalil et al. (2006b), and the magenta diamonds indicate the positions of the stars used in vdMS16.	19
2.2	Median standard deviation of the source positions for all fields used in the analysis. The green points represent the median of all stellar sources in a field. The crosses represent measurements for the first epoch of observations and the diamonds represent the second epoch. .	21
2.3	Example of all sources in the vicinity of the known position of the quasar. Black points represent all sources in the field, green diamonds represent the sources within 7 arcseconds of the known QSO position, and the red square represents the QSO. (Top) Color Magnitude Diagram for the field. (Bottom) Proper motion divided by the scatter in position in the pixel frame, described further in Section 2.2.3. . . . .	22
2.4	Positions in the master reference frame of the QSO from each individual dither (black triangles) for Field 1 with the average for each epoch marked by green circle. The "motion" is the inverse of the average motion of the stars, as we measure the QSO position relative to the stellar frame. . . . .	24
2.5	The measured proper motions for each field (green), along with the earlier measurements by NK13 (cyan) and vdMS16 (magenta). . . . .	29

2.6	The motions inferred for each quasar (green points), corrected for the reflex motion, as compared to the median motions for the stars (black points). The median uncertainty for the stars is shown. That the stars cluster close to zero and that the average of the stars is still closer to zero indicates that the transformations have worked as intended. . . .	30
2.7	The residual motion vectors calculated after subtracting our adopted COM motion determined in this study. Similar to Figure 2.1 the green, cyan, and magenta measurements are this study, NK13, and vdMS16, respectively. The boxes indicate the uncertainty in the motion for that field where a vector that exceeds its box corresponds to a residual vector of greater than one $\sigma$ . A reference vector of $100 \text{ km s}^{-1}$ is shown at the bottom right, and the two centers used for the models are shown as well with the H I derived center marked by the dashed orange circle and the Ripepi et al. (2017) center marked by the dashed red circle. For orientation, north is up and east is to the right. . . . .	35
2.8	The locations of the two centers tested: the H I derived center (dashed orange circle) and the Ripepi et al. (2017) center (dashed red circle). Three areas with potential kinematic signatures are also marked. The regions considered to be the Counter-Bridge and Western Halo are marked by the cyan ellipses, and the direction towards the Magellanic Bridge is marked by the cyan vector. For orientation, north is up and east is to the right. . . . .	36
2.9	Amplitudes for the radial (top) and tangential (bottom) components of the residual motions for the H I center, $V_{\text{rot}}$ free model, as a function of distance from the center. For calculating the error-weighted mean, we exclude any fields not consistent with zero to within twice the observational error. The resulting error-weighted mean is indicated by the red line and the error of the weighted mean is shaded above and below the line. . . . .	37
2.10	The composite CMD for all new SMC fields. The dividing lines for the red and blue subpopulations, examined in Figure 2.11, are marked at $(F606W - F814W) = 0.45$ and $F606W < 21 \text{ mag}$ . . . . .	41
2.11	Residual proper motions in the E-W (top) and N-S (bottom) directions for all fields with enough red and blue stars for the transformations. There are essentially no statistically significant differences between the different populations. . . . .	42

- 2.12 The LMC-SMC separation at their last encounter as a function of the time of the last encounter, color-coded by the present-day relative velocities between the LMC and SMC (in  $\text{km s}^{-1}$ ). The panel on the left shows results for integrations assuming a MW virial mass of  $10^{12} M_{\odot}$  and an LMC halo mass of  $1.8 \times 10^{11} M_{\odot}$ , on the lower (larger) end of MW (LMC) mass possibilities in the literature. The panel on the right is for a heavier MW virial mass of  $2 \times 10^{12} M_{\odot}$  and a lighter LMC halo mass of  $3.7 \times 10^{10} M_{\odot}$ , on the larger(lower) end of possible MW(LMC) masses. The red star indicates the mean value in each case. Impact parameters higher than 20 kpc are found to be highly unlikely. Impact parameters as small as 2.5 kpc and as recent as 100 Myr are possible, but a bulls-eye hit (0 kpc impact parameter) is unlikely. . . . . 46
- 3.1 *Gaia* source density count around the Magellanic System with cuts made as described in 3.2.1 for astrometric quality. The green crosses mark the locations of the assumed centers of the LMC and SMC, and the red box indicates the area examined further for Bridge dynamics. (0,0) is defined as the kinematic center of the SMC. . . . . 75
- 3.2 Color-Magnitude Diagram of the selected Bridge region. All stars in the region are marked in gray. The blue colored points indicate the stars selected by our mask as main sequence stars, and the orange-red colored points indicate the red giant mask. From left to right the PARSEC isochrones are 10 Myr (solid blue line), 30 Myr (dashed dark blue line), and 800 Myr (solid red line), all more metal-rich than  $[M/H] > -0.65$ . . . . . 76
- 3.3 Proper motion diagram for the selected Bridge stars. All stars present in the region are marked in gray. The blue lines indicate the PM region identified as belonging to the Magellanic system. The light green square indicates the PM of the SMC and the light green star indicates the PM of the LMC. . . . . 77
- 3.4 Bridge region with the main sequence (MS) population marked in blue and the red giant population (RG) marked in orange-red. The frame has been rotated such that the  $x$ -axis now lies along the line between the assumed centers for the LMC and SMC, where (0,0) is the center of the SMC. The area comparable to Model 2 (discussed in 3.3.3) has been outlined in black for easier comparison, and the locations of the *HST* fields are marked with brown stars. The RG population has been randomly subsampled down to the level of the MS stars to allow for easier comparison of the spatial correlations. . . . . 78

- 3.5 Color-magnitude (top) and proper motion diagrams (bottom) for the three *HST* fields. Stars selected as belonging to the Magellanic Bridge are plotted in red while non-members are plotted in gray. In the top panels, we overplot isochrones with metallicities  $[\text{Fe}/\text{H}] = -1.0$  and ages 0.25, 1, 3, 5, and 10 Gyr to represent stellar populations expected in these regions. Distances of 62, 62, and 50 kpc were adopted respectively for BG1, BG2, and BG3. We applied reddening to the isochrones based on the  $E(B - V)$  values estimated from interpolating the reddening maps of Schlegel et al. (1998), and the total absorption values were adopted from Table 6 of Schlafly & Finkbeiner (2011). . . . . 79
- 3.6 Vector field of the residual PMs of the stellar populations in the Bridge relative to the SMC COM PM. The RG stars are displayed in orange-red, and the MS stars in blue. The *HST* fields are marked in brown. The locations of each population are displayed in the background for reference. The median vectors are created from  $0.5^\circ \times 0.5^\circ$  bins and are only calculated if five or more stars are present. A reference vector of  $1 \text{ mas yr}^{-1}$  is provided at the top of the figure in black. The largest *Gaia* vector has a length of  $1.01 \text{ mas yr}^{-1}$ . . . . . 80
- 3.7 (Left) Relative proper motions of the stars in the Bridge along the  $x$ -axis as a function of angular distance from the center of the SMC. All MS stars selected as part of the Bridge are displayed in gray. To understand the typical motion as a function of distance across the Bridge, the data are binned every 0.2 degrees, and the resulting error-weighted average PM in each bin is displayed in blue along with the standard error for weighted averages. The systematic errors of the *Gaia* DR2 catalog are not displayed. The motions of the *HST* fields are marked in brown and the LMC-disk PMs by the light green region on the lefthand side of the plot. The vertical dashed line indicates the limit of comparison to Model 2, and the horizontal dashed line at  $0 \text{ mas yr}^{-1}$  is a guide for the eye. (Right) Same as for the left plot but for the motion along the  $y$ -axis. . . . . 81

- 3.8 (Left) Relative proper motions of the older stars in the Bridge along the  $x$ -axis as a function of angular distance from the center of the SMC. All RG stars selected as part of the Bridge are displayed in gray. To understand the typical motion as a function of distance across the Bridge, the data are binned every 0.2 degrees, and the resulting error-weighted average PM in each bin is displayed in orange-red along with the standard error for weighted averages. The systematic errors of the *Gaia* DR2 catalog are not displayed. The motions of the *HST* fields are marked in brown and the LMC-disk PMs by the light green region on the lefthand side of the plot. The vertical dashed line indicates the limit of comparison to the models, and the horizontal dashed line is at 0 mas yr<sup>-1</sup> as a guide for the eye. (Right) Same as for the left plot but for the motion along the  $y$ -axis. . . . . 82
- 3.9 (Top) H I gas intensity map from Putman et al. (2003) with lines of constant RA and Dec provided for reference. The LMC is the large structure in the middle left of the panel and the SMC is located below and to the right of the LMC with the Bridge stretching between them. (Bottom) The H I map transformed into our working frame with the location of the selected MS stars overplotted in blue. . . . . 83
- 3.10 (Left) Error-weighted average relative PMS along the Bridge in the  $x$ -axis direction, calculated as described in Section 3.3.1 for the RG (orange-red) and MS (blue) stars. The motions of the *HST* fields are marked by the brown squares and the LMC-disk PMs by the light green region on the lefthand side of the plot. The predicted motions from the two models are plotted here as well (purple for Model 1, lime-green for Model 2). The average error for the models is on the order of  $\sim 0.1$  mas yr<sup>-1</sup>. Model 2 allows for a direct collision between the SMC and LMC while Model 1 assumes they do not. At the start of the Bridge ( $\sim 2$  degrees from the SMC) Models 1 and 2 begin diverging, with Model 2 motions having a similar trend as both the observed RG and MS star motions. (Right) Same as the left plot but for motion along the  $y$ -axis. Near the start of the Bridge, Models 1 and 2 do not provide significant discriminating power. However, as Model 1 continues for the length of the Bridge, we observe a clear divergence from the data for both the RG and MS stars on approach to the LMC-side of the Bridge. . . . . 84

4.1	<i>Gaia</i> DR2 sources after initial astrometric cuts have been applied to the data, displayed in a Cartesian coordinate system as outlined in Gaia Collaboration et al. (2018c). The zero point is set to the best-fit center for the RG population (the red “x”), described in Section 4.2. The inferred kinematic center from H I gas is marked by the blue star, and the geometric center derived from the RR Lyrae population is marked by the green square. The SMC Wing can be seen on the eastern (left) side of the SMC, heading towards the Magellanic Bridge and the LMC. We also note the empty patch on the right side of the figure as the location of 47 Tuc, which has been removed from our sample by our astrometric criteria. . . . .	91
4.2	Color-Magnitude Diagram of all sources present in Figure 4.1. Two separate stellar sequences have been marked: the main sequence (MS) stars in blue on the left side and the red giants (RG) on the right side. The top of the red clump can be observed near (1.0, 18.0), but due to worsening astrometric performance near $G \sim 18$ , we have chosen not to examine it further. All sources that have been matched to an existing RV measurement (described in Section 4.2.2) are marked in green, which can be seen to mostly sample the RGs but do extend to the sequence blueward of the RGs, likely a red supergiant population in the SMC. . . . .	94
4.3	All SMC main sequence (MS, blue) and red giant (RG, red) stars from Figure 4.2 in the same field of view and Cartesian coordinate system as Figure 4.1. The MS stars have a clear spatial structure to them, tracing the optical main body of the SMC and stretching into the Wing, while the RGs have a significantly more well-behaved structure, appearing to be roughly azimuthally isotropic with a radial dependence for the density. . . . .	95
4.4	Distribution of the PMs of the RG and MS samples. The PM center of the RGs, measured with a simple Gaussian fit, is marked by the black “X”. The RG PM is clearly offset from where one would place the MS center, though the asymmetric extension of the MS PMs towards the left side of the figure would make it difficult to accurately assess the systemic MS PM. . . . .	96
4.5	Spatial locations of all RG stars (same Cartesian frame as in Figure 4.1) selected for analysis. The stars possessing a measured RV are marked in green. The resulting distribution of RV stars does favor the interior of the SMC but coverage is available for much of the RG distribution. . . . .	98

- 4.6 The average residual PM vectors of the SMC RGs as a function of location in the SMC. The gray points mark all RG stars used in the averaging. The solid black lines indicate the original Cartesian coordinate system, and the dashed black line marks the rotated frame where the  $x$ -axis lies along the major axis of the SMC RG distribution. The dark red vector marks the relative velocity, as projected on the sky, between the LMC systemic motion and the SMC systemic motion,  $\mu_{\text{LMC-SMC}}$ . Clear outward motion can be seen on the eastern side of the SMC, consistent with the direction of  $\mu_{\text{LMC-SMC}}$ , while coherent rotation appears to be located in the center of the SMC. . . . . 101
- 4.7 **(Top)** All RG stars in our selected sample plotted using our Cartesian frame. The small, tightly clumped dark areas in the plot are believed to be globular clusters or other stellar associations belonging to the SMC. **(Bottom)** All model stars, scaled to qualitatively match the observational data, plotted in our Cartesian frame. The central under-density present in the data has been artificially created in the model in an effort to reflect observations. . . . . 103
- 4.8 Residual PMs plotted against spatial position in the SMC geometric major/minor axis frame. The gray points are all of the RG stars in the same. The stars are binned accordingly to the spatial sampling, which is about 0.08 degrees in X and 0.06 degrees in Y. A simple average is taken for each bin, marked by the orange-red point, and the standard deviation of the bin is shown as the error bar. **(Left)** Residual PM in Y (which points roughly along the axis of relative LMC-SMC motion) as a function of position in X (which spans the major axis of the SMC, with the positive X direction north of the Magellanic Bridge). **(Right)** Residual PM in Y as a function of position in Y. . . . . 108
- 4.9 Residual PM vectors for the best-fit model to the data (specifics can be found in Table 4.1), displayed in the same format as Figure 4.6. Unlike the data, the residual vectors are limited to the area encompassed by a single 2D Gaussian function that had been fit to the original RG distribution. . . . . 112
- 4.10 **(Left)** Spatial positions of the *Gaia* sample with cross-matched RVs, color coded by the residual RV (after removing the SMC systemic RV and correcting for viewing perspective). The non-RV stars for each respectively stellar population are marked by the grey points in the background. **(Right)** Bin-averaged residual RVs from the best-fit model. . . . . 113

- 4.11 Residual PMs as a function of spatial position for all permutations of  $PM_X/PM_Y$  and  $X/Y$ . The light grey points are the mock RG stars from the kinematic models. The orange-red points are the measured *Gaia* RG residual PM averages, and the purple points are the averaged residual PMs for the mock RG stars. The model presented here is the best-fit model to the data (specific parameters are listed in Table 4.1). 114
- 4.12 Residual PM vector plots for the *Gaia* RG stars (orange-red, top left), the best-fit model (top right), the model inferred by D14 (bottom left), and the model inferred by DT19 (bottom right). The frame and vectors are displayed in the same manner as Figure 4.6. The *Gaia*-measured residual PMs have been limited to only the bins that have measured PMs in the mock SMC data. One can readily observe the departures from the *Gaia* data in both the D14 and DT19 models that fail to capture the behavior on the eastern edge of the SMC, while the tidal+rotation best-fit model is able to capture both that structure while also managing to describe the finer interior motions. . . . . 117
- 5.1 *Gaia* DR2 sources after initial astrometric cuts have been applied to the data, displayed in a Cartesian coordinate system as outlined in Gaia Collaboration et al. (2018c). For each plot, the zero point is set to the best-fit center for the RG population found in Z20 (the “x”, red in top left), and the inferred kinematic center from H I gas is marked by the square (blue in top left). (top left) All stars in the *Gaia* sample are displayed. The SMC Wing can be seen on the eastern (left) side of the SMC, heading towards the Magellanic Bridge and the LMC. We also note the empty patch on the right side of the figure as the location of 47 Tuc, which has been removed from our sample by our astrometric criteria. (top right) The red giant population as identified in Figure 5.2. (bottom left) The red supergiant population. (bottom right) The main sequence population. . . . . 127
- 5.2 Color-Magnitude Diagram of all sources present in the top left panel of Figure 5.1. Three separate stellar sequences have been marked: the main sequence (MS) stars in light blue on the left side, the red supergiants (RSG) in green near the center, and the red giants (RG) on the right side. All sources that have been matched to an existing RV measurement (described in Section 5.2.2) are marked in dark blue, which can be seen to mostly sample the RGs but do extend into the RSGs. . . . . 129
- 5.3 Binned spatial distribution of the SMC RSG population. The H I and RG centers (blue square and red “x”) from Figure 5.1 are displayed for reference along with the center from a 2D Gaussian fit to the RSG data (green diamond). . . . . 132

- 5.4 Binned PM distribution of the SMC RSG population. The systemic PM for the RGs is marked by the red “x”, the systemic PM assumed for H I models is marked by the blue square, and the mean location from a 2D Gaussian fit to the RSG PM data (green diamond). . . . . 133
- 5.5 Averaged residual PM vectors in a Cartesian coordinate system, every 0.2 degrees for easier display of the kinematic behavior. The dark red vector indicates the direction of relative LMC-SMC motion, assuming the RG systemic PM from Z20. For both plots, the assumed kinematic center and systemic PM are the same, and the solid black line provides a guide for the eye for the  $x$ - and  $y$ -axes. **(Left)** RSG *Gaia* PM vectors are marked in green. The dashed black line indicates the rotated coordinate system used for the spatial-kinematic quantification, as described in Section 5.3.2. **(Right)** Residual PM vectors (in purple) for the best-fit kinematic model to the SMC RG population from Z20 as a demonstration of the capabilities and limitations of the current modeling. 136
- 5.6 Averaged residual PM vectors in the same Cartesian frame as displayed in Figure 5.5. To gain a clearer insight into the central internal kinematic of the SMC RSGs, the field of view has been shrunk to only encompass the inner 4 degrees. The relative LMC-SMC vector and dashed black lines are the same as the previous Figure. . . . . 137
- 5.7 Residual PMs plotted against spatial position in the SMC RG geometric major/minor axis frame. The gray points are all of the RSG stars in the same. The stars are binned accordingly to the spatial sampling, which is about 0.13 degrees in X and 0.07 degrees in Y. A simple average is taken for each bin, marked by the green point, and the standard deviation of the bin is shown as the error bar. **(Top Left)** Residual PM in X (which spans the major axis of the SMC, with the positive X direction north of the Magellanic Bridge) as a function of position in X. **(Top Right)** Residual PM in X as a function of spatial position in Y (which is roughly along the axis of the relative LMC-SMC motion). **(Bottom Left)** Residual PM in Y as a function of spatial position in X. **(Bottom Right)** Residual PM in Y as a function of position in Y. 138
- 5.8 Spatial positions of the *Gaia* sample with cross-matched RVs, color coded by the residual RV (after removing the SMC systemic RV and correcting for viewing perspective). The non-RV stars for each respective stellar population are marked by the grey points in the background. **(Left)** All RSGs with residual RVs. **(Right)** All RGs with residual RVs. . . . . 140

# List of Tables

2.1	New SMC Observations and Results. . . . .	26
2.2	Previous SMC Observations and Results. . . . .	28
2.3	SMC Best-Fit Parameters. . . . .	53
2.4	SMC Center of Mass Proper Motions. . . . .	53
2.5	Galactocentric Velocities . . . . .	54
3.1	<i>HST</i> Target Fields and Observations . . . . .	61
3.2	Proper Motion Average and Dispersion for the Magellanic Bridge Stars in the <i>HST</i> Fields . . . . .	64
4.1	Rotation Model Parameters. . . . .	116
4.2	Best-Fit Model Values & Uncertainties. . . . .	116
5.1	SMC Systemic Model Properties. . . . .	143

# Chapter 1

## Introduction

### 1.1 Milky Way Satellites

#### 1.1.1 Background

One hundred years ago, the astronomical community held what is now known as The Great Debate: the argument over whether our Milky Way (MW) comprised the whole of the universe or if some of the nebula seen in the night sky were other “island universes.” In the hundred years that followed, the existence of these “island universes,” or galaxies as we now refer to them, quickly became the accepted paradigm in the community, and we made great strides in learning more about them. This extended to learning more about the volume of space around the MW where we came to realize that significantly smaller galaxies than our MW, these dwarf galaxies, likely orbited around us.

At the turn of the 21st century, we had discovered 11 of these “satellite” galaxies, now referred to as the “classical” MW satellites, with many discovered via inspection of photographic plates. However, as we progressed into the new century, we entered

into a new era of MW astronomy, one led by all-sky survey utilizing advanced CCD instruments to gather deeper exposures on short time scales than previously possible. The Sloan Digital Sky Survey (SDSS) led the way in this effort, and with the swathes of new data, the number of known MW satellite galaxies doubled within the first five years of SDSS being active. This trend continued with the Dark Energy Survey (DES), which pushed even fainter than SDSS, leading to the discovery of more MW satellites (Koposov et al. 2015; Drlica-Wagner et al. 2015). The rapid explosion of satellite discoveries has slowed in recent years, but new satellites continue to be found as more surveys are conducted across the world (Homma et al. 2018, 2019, e.g.,). To date, we know of more than 50 MW satellite candidates, across a range of size and distance (see Figure 1.1 for a plot of known MW satellites).

### 1.1.2 Implications for $\Lambda$ CDM

As we have discovered more of these satellite galaxies, our understanding of their place and significance in the universe has evolved in parallel. The basic paradigm used to model structure in the universe is the  $\Lambda$ -Cold Dark Matter ( $\Lambda$ CDM) model, where today the energy density of the universe is spread across the three components of dark energy, dark matter, and baryonic matter. On large scales ( $> 1$  Mpc),  $\Lambda$ CDM appears to explain the observed distribution and structure of galaxy well. However, in recent years as improved mass-resolution simulations became possible, new disagreements between simulation and observation on smaller scales, like the MW and its surrounding satellites, have appeared. The four key problems, which will be discussed in brief detail below, are: “missing satellites,” “core vs cusp,” “too big to fail,” and “satellite planes.”

The first problem, the “missing satellites” problem, stems from the mismatch in

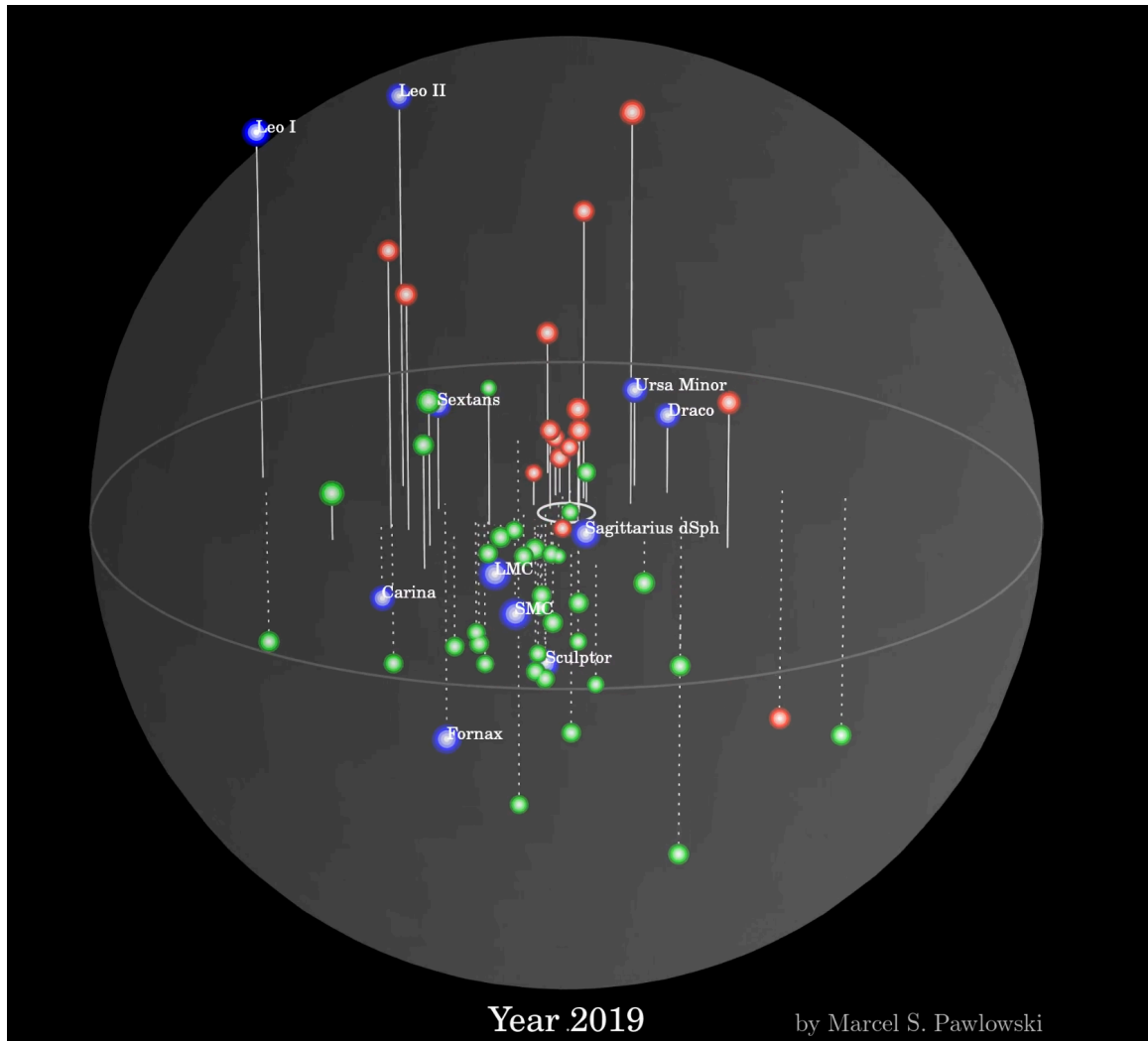


Fig. 1.1.— Distribution of known MW satellites. This image is from a movie produced by Marcel S. Pawlowski for Bullock & Boylan-Kolchin (2017). The classical MW satellites are indicated by the blue points, the SDSS-discovered satellites are marked by red points, and all satellites discovered with DES onwards are marked by green.

observed numbers of MW satellites versus the (far larger) observed number dark matter halos in numerical simulations. In high resolution simulations, clumps of dark matter form at every possible mass scale, with no apparent mass cut off (e.g., Garrison-Kimmel et al. 2014). As a result, based on expectations from dark-matter-only simulations, one would anticipate finding potentially thousands of satellite galaxies surrounding a galaxy with the mass of the MW. But we do not observe this, having just now reached 50 observed satellites. One possible solution lies in the possibility that as the dark matter halo mass gets smaller, it becomes easier to disrupt the formation of the galaxy (e.g., Sawala et al. 2016). Combined with the idea of “abundance matching,” where one assumes the largest satellite halo in the simulation corresponds to the largest observed halo, the previous discrepancy between simulations and observations appears to be resolved, at least to the scale of the classical satellites (Garrison-Kimmel et al. 2017). However, work remains in investigating whether this extends to the lowest mass MW satellites, often referred to as the “ultra-faint dwarfs” (UFDs).

The second problem, “core vs cusp,” deals with the expected distribution of dark matter in halos. Under normal  $\Lambda$ CDM, one expects to find a steeply rising density of dark matter, a “cusp-y” shape, as one approaches the center of the halo (Navarro et al. 2010). For larger galaxies, like the MW, the fraction of baryons (and feedback associated with the baryons like supernovae) is expected to be large enough to smooth the density profile from a “cusp” into a “core.” However, in many available studies of galaxies that should be primarily dark matter-dominated, the measured rotation curves are consistent with constant densities (“cores”) in the center of the galaxy (e.g., de Blok et al. 2008). Moving forward, continuing to push lower on the mass (both halo mass and stellar mass) scale for galaxies to measure rotation curves will prove a

crucial constraint in answering this question.

The third problem, “too big to fail,” deals with a consequence of the potential above solution to the missing satellites. In assigning the largest halo to the largest observed satellite, one should be able to make predictions regarding the rotation curve measured in the satellite (Boylan-Kolchin et al. 2011). So far this prediction does not seem to hold true. Comparisons with recent  $\Lambda$ CDM simulations consistently find central densities significantly denser than those observed in the bright MW satellites (Boylan-Kolchin et al. 2012). Simulations do contain dark matter halos with a mass in line with the mass inferred from the MW satellite rotation curves, but it raises the question of why wouldn’t the very largest halos be able to form galaxies as well? Studies pushing further into the Local Group have detected this same inconsistency among other host-satellite systems (Tollerud et al. 2014). Similar to the “core vs cusp” problem, continuing to characterize galaxies further down the mass scale will play a vital role in understanding the full extent of the disagreement.

The final and most recent problem, “satellite planes,” deals with the low probability in  $\Lambda$ CDM of satellite galaxies around a host galaxy forming into a coherent order. In the very early days of discovering MW satellites, it was observed that the satellites did not appear to have a random distribution to them, as might be naturally expected (Kunkel & Demers 1976). As there were a relatively small number of satellites known, this problem did not stand out as a fundamental issue. However, as more 3D motions for MW satellites were measured, along with an increase in the total known number of satellites and improved simulations/expectations for satellite distributions in  $\Lambda$ CDM, this non-spherical distribution remained (Pawlowski et al. 2012). Beyond simply appearing anisotropic, the satellites seem to have a preferential alignment of their orbital poles, with the structure being dubbed the “vast polar

structure” (VPOS) (Pawlowski et al. 2013). Even with the most recent PMs available for a large fraction of MW satellites, upwards of 40% of MW satellites seem to align with VPOS. As of yet, no competitive solution has been proposed, but more work will be required to push fainter to find satellite systems around other host galaxies to increase the total sample of host/satellite systems to better identify the degree to which the MW may be an outlier.

In each of these cases, improved kinematic information for the MW satellites will be foundational and instructive in improving our constraints on small-scale agreements (or disagreements) with  $\Lambda$ CDM.

### 1.1.3 Measuring MW Satellite Kinematics

However, it has been a slow process in attempting to determine the full 3D kinematics of MW satellite galaxies. While we have been able to measure the radial velocities (RVs) of the satellites for decades (e.g., Feast et al. 1961), measuring the motion in the plane of the sky, or the proper motion (PM), has proven more difficult. Part of this is simply the physical distance to many of these objects, which results in the PMs for many of the MW satellites being on the order of milliarcseconds per year ( $\text{mas yr}^{-1}$ ). To make such a precision measurement requires some combination of time (the more time passes, the larger the apparent motion) and angular resolution. The better the resolution, the less time is required to be able to detect the motion. Conversely, even with ground-based telescopes, given a long enough baseline of time, PM measurements can be made.

Indeed, as astronomy entered into the CCD era, multiple attempts were made at measuring PMs for MW satellites, such as the Large Magellanic Cloud (e.g., Pedreros et al. 2002). Even in the best cases though (e.g., a ten-year baseline, enough

member stars in the image to outweigh statistical noise), the errors were often large, ranging from 20% to 50% of the measured PM. It was not until the application of the *Hubble Space Telescope* (*HST*) that true high precision PMs were realized. Using the High Resolution Camera and only a two year baseline, Kallivayalil et al. (2006b) measured the PM of the LMC to highest precision of any MW satellite to that point. From then, *HST* became a leading source of MW satellite PMs, from the Magellanic Clouds (Kallivayalil et al. 2013) to further afield satellites like Leo I (Sohn et al. 2013).

This remained the case for just over a decade until the introduction of the *Gaia* Data Release 2 (DR2) (Gaia Collaboration et al. 2018b). The *Gaia* Space Telescope (Gaia Collaboration et al. 2016a,b) was designed as a follow up telescope to the original European astrometry satellite, *Hipparcos*. *Gaia* aimed to measure parallaxes for all relatively bright stars within the nearest 10 kpc of the Sun and PMs for a huge volume of stars around the MW. And it delivered with DR2. The published catalog contained PMs for more than one billion stars, and immediately enabling a range of astrometry experiments. This extended to the MW satellites, where the new DR2 catalog was cross-matched with lists of known spectroscopic members of the satellites to measure the systemic PM for the system (Fritz et al. 2017b). In total, with DR2 almost 40 PMs were measured for the MW satellite system and opened a new window into understanding these dwarf galaxies.

## 1.2 The Magellanic Clouds

This astrometric revolution extended to two of the largest MW satellites: the Large and Small Magellanic Clouds (LMC and SMC, respectively). Observable from the southern hemisphere, the Clouds are close enough and bright enough to be visible with the naked eye on a dark night (Figure 1.2 shows a picture of them alongside the

MW). It should be acknowledged that long before the Clouds gained their current moniker, they were well known and involved in stories of countless cultures across the southern hemisphere of the world. To the Sotho, a Bantu ethnic group of Southern Africa, view the dwarf galaxies as being the tracks of celestial beasts (from African ethnoastronomy, Astronomical Society of Southern Africa). For the Adelaide people, an Australian indigenous group, the Clouds were referred to as “Ngakallamurro,” translated as “paroquet-ashes,” which told the story of a group of birds lured into the sky by a constellation, only to instead be roasted (from Australian Indigenous Astronomy). If a group of people in the Southern hemisphere had stories about the sky above them, then the Clouds were surely featured somewhere.

From the viewpoint of Western astronomy, the Clouds offer an intriguing laboratory for testing our ideas and understanding of galaxy formation, as they represent the closest example we have of an active galaxy merger. For a significant period of time in studying the Clouds, the common paradigm was the Clouds had been in orbit around the MW for an extended period of time, which led to the formation of the Magellanic Stream, a trail of neutral hydrogen gas stretching nearly all the way around the MW. However, from the first *HST* PM measurement of the Clouds (Kallivayalil et al. 2006b), this understanding began to change with the measured PMs placing the the Clouds on first in-fall into the MW (Besla et al. 2007), creating new challenges in explaining the structure we observe. Since then, new observations of the Clouds have revealed more about them.

For the LMC, it has proven a more straightforward system to understand kinematically. Given its appearance as a slightly irregular disk with a bright bar and previous RV studies (e.g., van der Marel et al. 2002), rotation had been measured but the exact geometry remained degenerate given only one direction of the velocity



Fig. 1.2.— The Large Magellanic Cloud can be seen to the upper right of the Milky Way, and the Small Magellanic Cloud can be seen on the far right side of the image.  
*Credit:ESO/H. Stockebrand*

was known. Using an expanded number of *HST* fields, full rotation geometry was revealed, including identifying the kinematic center from the rotation, which coincided with the known H I center (Kallivayalil et al. 2013; van der Marel & Kallivayalil 2014). Later work has reinforced this idea of relatively well-behaved kinematics in the interior of the LMC, however evidence for a more dramatic interaction with the SMC can be found further out in the LMC (e.g., Choi et al. 2018b,a; Nidever et al. 2018; Mackey et al. 2018).

Perhaps the most exciting LMC result came shortly after the DR2 publication. One consequence of  $\Lambda$ CDM is that because of the hierarchical nature of the dark matter halos (that there should be halos inside of halos inside of halos), we should expect to observe satellite galaxies that possess their own satellites. As the largest MW satellite, with the recent explosion in known UFDs in the vicinity of the LMC, and that it appears to be on its first in-fall into the MW, the LMC was a natural candidate for being able to definitively satellites that originally belonged to it (Sales et al. 2011, 2017). Using numerical simulations of MW and LMC-like analogues interacting along with the new *Gaia* PMs, Kallivayalil et al. (2018) analyzed the angular momentum and locations of the UFDs, finding that four of them (Horologium I, Carina II, Carina III, and Hydrus I) were consistent with originally belonging to the LMC. This represents the first kinematically-driven detection of satellites of satellites, reinforcing a core concept of the  $\Lambda$ CDM paradigm.

### 1.3 The Small Magellanic Cloud

The smaller of the two Clouds, the SMC has an argument to be perhaps the most kinematically complex MW satellite. There is no lack of evidence to support the idea that the two galaxies have undergone at least one major interaction and are

likely continuing to undergo tidal interactions. Perhaps the most dramatic piece of evidence for this is the trail of stars and gas that appears to connect the two galaxies: the Magellanic Bridge. Studies have found evidence for both young stars, presumably formed in situ (Harris 2007), and intermediate-age stars in the Bridge (e.g., Bagheri et al. 2013; Nidever et al. 2013). Even old stellar populations have been detected in the vicinity of, but not aligned with, the gaseous Bridge (e.g., Belokurov & Koposov 2016; Deason et al. 2016), adding support to the idea that the SMC is being tidally stripped by the LMC.

*HST* PMs of the LMC and SMC supported this scenario, finding that the Clouds have recently collided (roughly  $\sim 150$  Myr ago) with a separation between the centers of only  $\sim 7.5$  kpc (Zivick et al. 2018). With the extent of the LMC radius known to be upwards of 15 kpc, this would place the center of the SMC passing directly through LMC disk. New studies utilizing *Gaia* DR2 data have found similarly turbulent kinematics for the SMC, with an ongoing discussion in the literature surrounding the existence or non-existence of rotation in the SMC.

Depending on the tracer used (e.g., gas, old stars, young stars) and the size of the window around the SMC being considered, the inferred rotation varied wildly. Older stellar tracers, using only RVs before *Gaia* PMs were available, found some amount of rotation in the SMC (Dobbie et al. 2014), though more recent efforts combining RVs and PMs have proved inconclusive (De Leo et al. 2020). Even for the RV studies of the neutral H I gas, which was originally believed to have coherent rotation in the SMC (Stanimirović et al. 2004), more recent work, using young stars to attempt to trace the gas, suggests that the kinematics are more complex than could be inferred from just the RV field (Murray et al. 2019).

Despite this complexity, or rather because of this complexity, the SMC serves as

an ideal testbed for developing a new 3D kinematic model for understanding MW satellites. With its size and brightness, it provides an unparalleled rich data set that can be used to explore how the underlying velocity components (systemic motion, random dispersion, rotation, and tidal expansion) are projected from physical space into our observed space. With the size and resolution, the SMC even offers the opportunity to investigate population-dependent kinematics to provide insight on how to approach identifying and properly separating the potentially contaminating populations. This model in turn, combined with improvements in future *Gaia* data releases, could be applied to other bright MW satellites. Sound physical understanding of the kinematics of these satellites would in turn unlock new insights into a range of topics from galaxy formation and evolution to providing new constraints on cosmological questions.

## Chapter 2

# The Proper Motion Field of the Small Magellanic Cloud: Kinematic Evidence for its Tidal Disruption

The following text originally appeared in *The Astrophysical Journal*, Volume 864, Issue 1, and has been lightly edited for this format.

### Summary

We present a new measurement of the systemic proper motion of the Small Magellanic Cloud (SMC), based on an expanded set of 30 fields containing background quasars and spanning a  $\sim 3$  year baseline, using the *Hubble Space Telescope* Wide Field Camera 3 (*HST* WFC3). Combining this data with our previous 5 *HST* fields, and an additional 8 measurements from the *Gaia*-Tycho Astrometric Solution Catalog, brings us to a total of 43 SMC fields. We measure a systemic motion of  $\mu_W = -0.82 \pm 0.02$  (random)  $\pm 0.10$  (systematic) mas yr $^{-1}$  and  $\mu_N = -1.21 \pm 0.01$  (random)  $\pm 0.03$  (systematic) mas yr $^{-1}$ . After subtraction of the systemic motion, we find little evidence for rotation, but find an ordered mean motion radially away

from the SMC in the outer regions of the galaxy, indicating that the SMC is in the process of tidal disruption. We model the past interactions of the Clouds with each other based on the measured present-day relative velocity between them of  $103 \pm 26$  km s<sup>-1</sup>. We find that in 97% of our considered cases, the Clouds experienced a direct collision  $147 \pm 33$  Myr ago, with a mean impact parameter of  $7.5 \pm 2.5$  kpc.

## 2.1 Introduction

Our understanding of the Small and Large Magellanic Clouds (SMC and LMC) has evolved greatly in the age of space-based proper motion (PM) measurements. The *HST* PM measurements by Kallivayalil et al. (2006b) were used to demonstrate that the Clouds had not orbited the Milky Way (MW) multiple times as expected but instead were likely on their first infall into the MW (Besla et al. 2007). With the supporting results from Piatek et al. (2008), this view of the Clouds became the new paradigm and has driven our understanding of their evolution.

Since then, the evolution of the LMC has proved more tractable to understanding. Using a longer baseline and the then new Wide Field Camera 3 (WFC3), Kallivayalil et al. (2013, hereafter NK13) significantly improved the PM errors for 26 LMC fields. Using the decreased uncertainties, van der Marel & Kallivayalil (2014) were able to make a direct measurement of the PM rotation curve of the LMC in the plane of the sky. A follow-up examination of the center of mass (COM) PM of the LMC and its rotation curve using PMs from the Tycho-*Gaia* Astrometric Solution (TGAS) Catalog (Lindegren et al. 2016), which combines *Gaia* Data Release 1 (Gaia Collaboration et al. 2016a,b) with the *Hipparcos* Tycho-2 Catalogue (Høg et al. 2000), supported this finding (van der Marel & Sahlmann 2016; hereafter vdMS16), suggesting that the inner region of the LMC is a relatively well-behaved system. Further out the

picture becomes more complicated with increasing evidence for more complicated substructures in the periphery of the LMC (Nidever et al. 2018; Choi et al. 2018b; Choi et al. 2018a; Mackey et al. 2018).

The structure and dynamics of the SMC has not proved to be as easy to understand. NK13 had results for only 5 fields, enough to attempt a measurement of the COM PM, but not enough to describe the internal kinematics. vdMS16 analyzed PMs for eight individual stars in the SMC from the TGAS Catalog (Lindgren et al. 2016), but the resulting residual motions were not indicative of any coherent motion. A third COM PM was measured by Cioni et al. (2016) as a by-product of their work on 47 Tuc did not provide any additional insight into the internal workings of the SMC.

Line of sight (LOS) motion studies have attempted to fill this gap. Stanimirović et al. (2004) found a rotation signature in the H I gas in the SMC with the line of nodes, defined as the line joining the points of maximum and minimum relative velocity, parallel to the visible major axis of the SMC and a dynamical center located in the northeastern section of the SMC. A study of the red giants in the SMC by Harris & Zaritsky (2006) suggested that the older population was dynamically separate from the neutral gas, having a very weak rotation signature and a much more significant velocity dispersion, suggesting a spheroidal rather than disk structure for the SMC. However, Dobbie et al. (2014) conducted a broader investigation of the red giant population, extending beyond the central area considered by Harris & Zaritsky (2006), and found instead a rotation signature of  $20\text{--}40 \text{ km s}^{-1} \text{ kpc}^{-1}$ , although their line of nodes did not agree with that found by Stanimirović et al. (2004). To complicate the picture further, Evans & Howarth (2008) found a similar rotation curve to Dobbie et al. (2014) but in the young, massive star population (O, B, and A stars). A slight

velocity gradient was also found for the OB stars by Lamb et al. (2016). While one could argue that the red giant population could be dynamically decoupled from the underlying neutral gas, one would not expect the same to have happened for the young stars. Dobbie et al. (2014) proposed an inclined disk to help explain the differences, but further kinematic evidence is needed to fully evaluate this possibility.

Because of the interest in the nature of the past mutual interactions of the Clouds, many photometric studies have searched for tidal debris at large radii from the Clouds, or evidence for SMC stars in the stream of H I gas linking the LMC and SMC, referred to as the Magellanic Bridge. There is evidence for both young stars, presumably formed *in situ* (Harris 2007), and intermediate-age stars in the Bridge (Nidever et al. 2013; Bagheri et al. 2013; Skowron et al. 2014; Noël et al. 2015). Even old stellar populations have been detected in the vicinity of, but not aligned with, the gaseous Bridge (Belokurov & Koposov 2016; Deason et al. 2016; Belokurov et al. 2017; Carrera et al. 2017), adding support to the idea that the SMC is being tidally stripped by the LMC.

Dias et al. (2016) studied the ages of star clusters throughout the SMC, finding clear age and metallicity gradients consistent with tidal interactions between the LMC and SMC. These results are supported by numerical models of the Magellanic system which predict that the SMC should be constantly churning and only at large radii would there potentially be a coherent rotation signature (Besla et al. 2012). A comprehensive study of the classical Cepheids in the SMC (Ripepi et al. 2017) found a complex geometric structure, with the near side forming a rough spheroidal shape before gradually shifting into a more linear shape, adding more detail to the SMC but presenting yet another potentially conflicting stellar structure.

In order to address the still sparse PM-coverage of the SMC, we obtained two

epochs of *HST* data with WFC3/UVIS for 30 fields in the SMC, focusing on obtaining data in the outer regions. Combined with the data already available from NK13 and vdMS16 for the interior of the SMC, this provides a broader kinematic view of the SMC. In this paper, we present the results from this combined dataset, and their implications for the orbital history of the SMC.

The paper is organized as follows. In Section 2.2 we discuss the quality of the data, our process for creating an astrometric reference frame, and how we quantify the uncertainties in the PMs for each field. We use these motions in Section 2.3, in conjunction with a dynamical model similar to the one in van der Marel et al. (2002), to analyze the measured PMs under various model assumptions. This produces a set of best fit parameters, including measurements of the overall COM PM for the SMC and a measurement of the rotational velocity. In Section 2.4, we subtract the best-fit COM motion to study the internal motions of the SMC, both for all stars and by stellar type. We use the newly determined COM PM to constrain the SMC’s past orbit, and examine its interactions with the LMC and MW in Section 2.5. Finally, we discuss the overall ramifications of the new SMC data for our understanding of the Magellanic system and where future studies will allow for further improvements in Section 2.6.

## 2.2 Data & Analysis

### 2.2.1 Description of Observations

Kozłowski et al. (2013) spectroscopically confirmed the presence of nearly 200 QSOs behind the SMC. From this set of QSOs, we selected 30 of the brightest QSOs ( $17.7 \leq V \leq 20.1$  mag) to provide an inertial reference frame across the two epochs of

observations. The QSOs were also selected to provide roughly uniform coverage of the SMC, over an approximately 16 square degree patch of sky (see Figure 2.1). Such a uniform sampling was required to better sample the kinematic behavior of the SMC. Kozłowski et al. (2013) were unable to observe their candidates in the NW corner of the SMC, leaving us with no spectroscopically confirmed QSOs to target, limiting our target fields to the central body and the southern and eastern periphery.

Both epochs of data were collected with the *HST* WFC3/UVIS, with the first epoch beginning observations in 2013 and the second epoch beginning in 2016, to provide a roughly 3 year baseline for each field (see Table 2.1). In the first epoch, 4 observations were collected with the F606W filter using a custom DITHER-BOX pattern to provide for optimal sampling of the point-spread function (PSF). The exposure times for each field ranged in length from 2 minutes to 6 minutes to achieve a signal-to-noise of  $\geq 200$  for the QSOs. Two additional short-exposure observations were obtained with the F814W filter to make color-magnitude diagrams (CMDs), to separate SMC and field stars, and to assist in identifying the QSO (see Section 2.2.2). For the second epoch, 6 dithered observations were collected with the F606W filter, and no observations were made with F814W filter as the astrometric transformations were only to be made with the F606W data. The orientation of the instrument was required to be the same for both observations of each field in order to minimize systematic errors.

### 2.2.2 Analysis of WFC3/UVIS Observations

For our analysis, we used the bias-subtracted, dark-subtracted, flat-fielded, and CTE-corrected images (`_flc.fits`) provided by the Space Telescope Science Institute (STScI) data reduction pipeline. The individual dithered images provide better astrometry

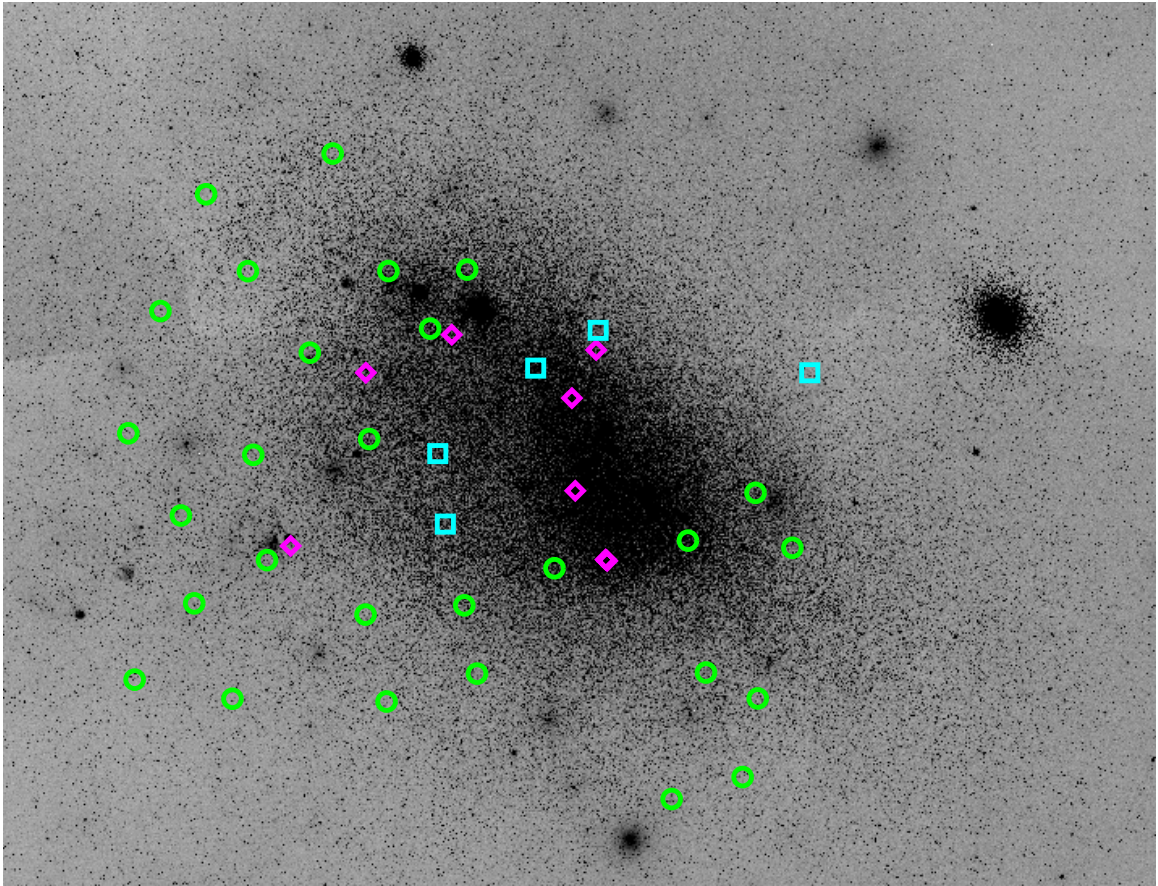


Fig. 2.1.— B-band image covering  $4^\circ \times 6^\circ$  from the Digital Sky Survey of the SMC (with 47 Tuc to the right) where north is up and east is to the left in the image. The LMC, northeast of the SMC, is located off the panel to the upper left. The green circles indicate the locations of our new reference QSOs from Kozłowski et al. (2013). The cyan squares show the quasars used in NK13 and Kallivayalil et al. (2006b), and the magenta diamonds indicate the positions of the stars used in vdMS16.

than the standard MultiDrizzle data product (`_drc.fits`), as noted in Anderson & King (2004). However, unlike the drizzled images, these data are not corrected for geometric distortion. To address this, we apply the known geometric distortion solution for WFC3/UVIS (Bellini et al. 2011) to the positions of the sources rather than correcting the images. These positions were measured using an empirically built PSF library for WFC3/UVIS, constructed similarly to the process described in Anderson & King (2006).

Once a list of sources was created from each individual image the pixel positions were converted into the WCS frame using the information contained within the `_flc` headers. The 30 brightest objects were selected from each list and matched using the WCS solution from the headers with a healthy tolerance of twenty arcseconds. This tolerance was chosen after a series of manual trials. We then used the brightest six matched objects as the initial constraints to linearly transform all sources into the reference frame of the first epoch.

Within a given field, the number of common sources varied from roughly 100 in the sparse fields towards the outer edges of the SMC to more than 1000 in the fields closer towards the visible body of the SMC. For the final transformations and iterations, we required that every source was detected in all ten dithered images, four from the first epoch and six from the second epoch, to simplify the uncertainty estimate.

The positional errors of the matched stars increase slowly as a function of magnitude, beginning at  $F606W \sim 20$ . For the iterative linear transformations a minimum error of 0.005 pixels was added to all sources brighter than 20 mag, measured from the median scatter for all sources with  $18 < F606W < 20$ , in order to avoid overweighting the transformation. The median scatter is roughly consistent across all fields (as seen in Figure 2.2).

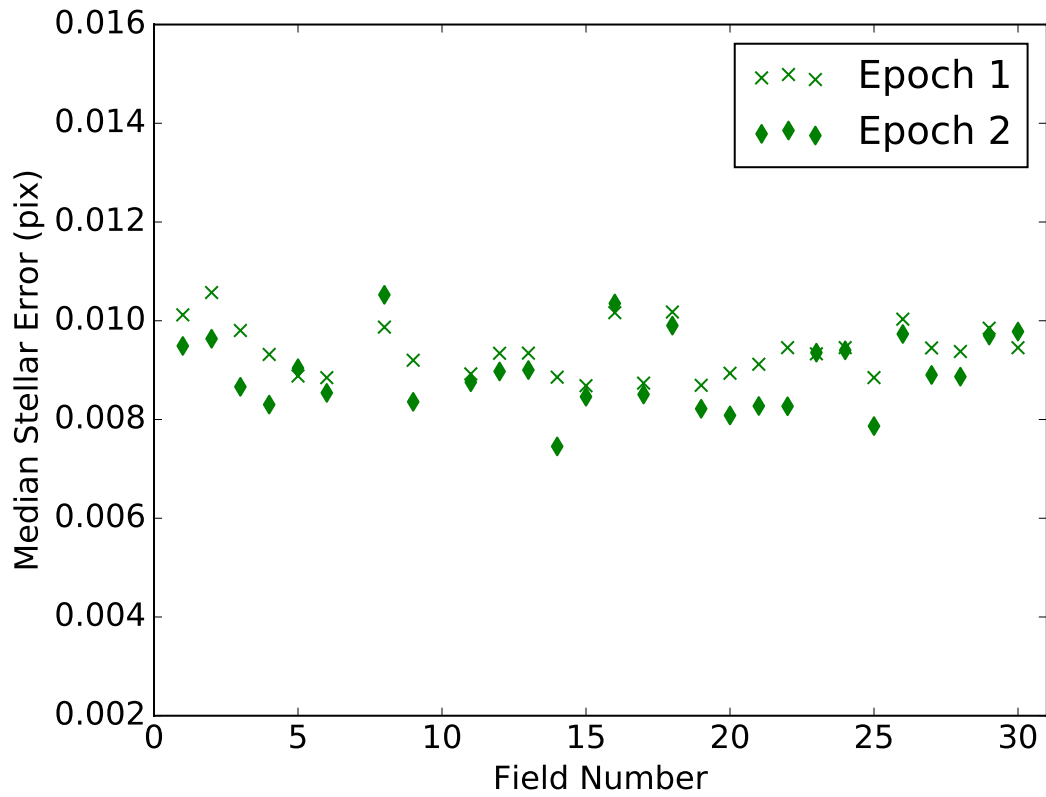


Fig. 2.2.— Median standard deviation of the source positions for all fields used in the analysis. The green points represent the median of all stellar sources in a field. The crosses represent measurements for the first epoch of observations and the diamonds represent the second epoch.

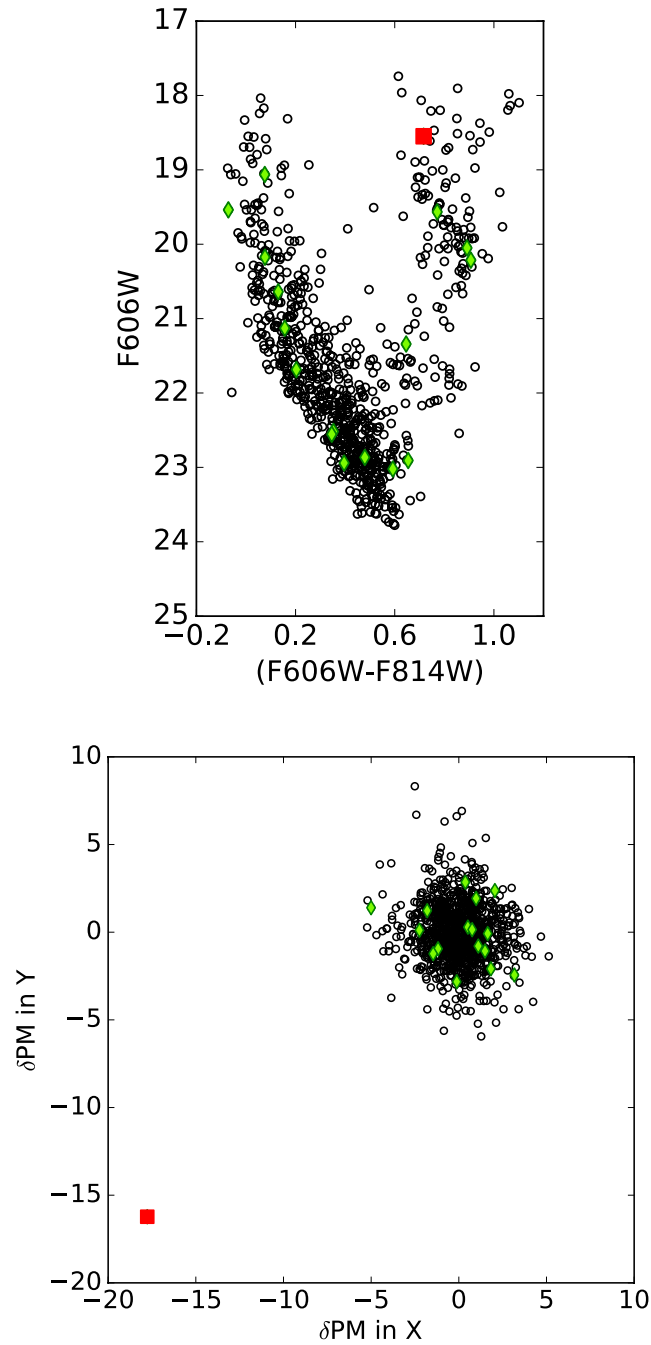


Fig. 2.3.— Example of all sources in the vicinity of the known position of the quasar. Black points represent all sources in the field, green diamonds represent the sources within 7 arcseconds of the known QSO position, and the red square represents the QSO. (Top) Color Magnitude Diagram for the field. (Bottom) Proper motion divided by the scatter in position in the pixel frame, described further in Section 2.2.3.

The next step is to identify the QSO. Using the known location of the QSO, we select all candidate objects within several arcseconds. From there, using a combination of the photometric and kinematic properties of the objects, we are able to identify the QSO, as demonstrated in Figure 2.3. Note that in our analysis, the SMC stars have zero average motion by construction, so the reflex motion of the QSO with respect to the stars is our measured signal, as can be seen with the red point in Figure 2.3. For Fields 7 and 10 we were unable to measure the motion of the QSOs. For Field 7, a foreground star overlapped the QSO, and for Field 10, the host galaxy was resolved, both situations causing a large scatter in position. In the second case, the host galaxy of the QSO was resolved and the uncertainty from fitting the galaxy with a Sersic profile and point source was larger than the expected proper motion signal.

### 2.2.3 Two Epoch Results

Once the initial transformation using the first six common sources was performed, each iteration thereafter applied stricter constraints on which sources were to be considered SMC sources. For each source, all dither positions in a given epoch were averaged together with the standard deviation of the positions used as the estimate for the positional uncertainty. The averaged positions between the epochs were subtracted from each other, with this difference then divided by the total error of the source (the standard deviation from each epoch added in quadrature) to create the  $\delta$ PM for the source, a measure of the statistical significance of the motion. Using these two measurements, thresholds were iteratively decreased, beginning with a one pixel tolerance and a  $\delta$ PM of 50 and ending with requiring all used sources to move less than 0.1 pixels and have a  $\delta$ PM less than 5, over an average of five steps.

The final motion for the field is the difference of the average positions of the QSO

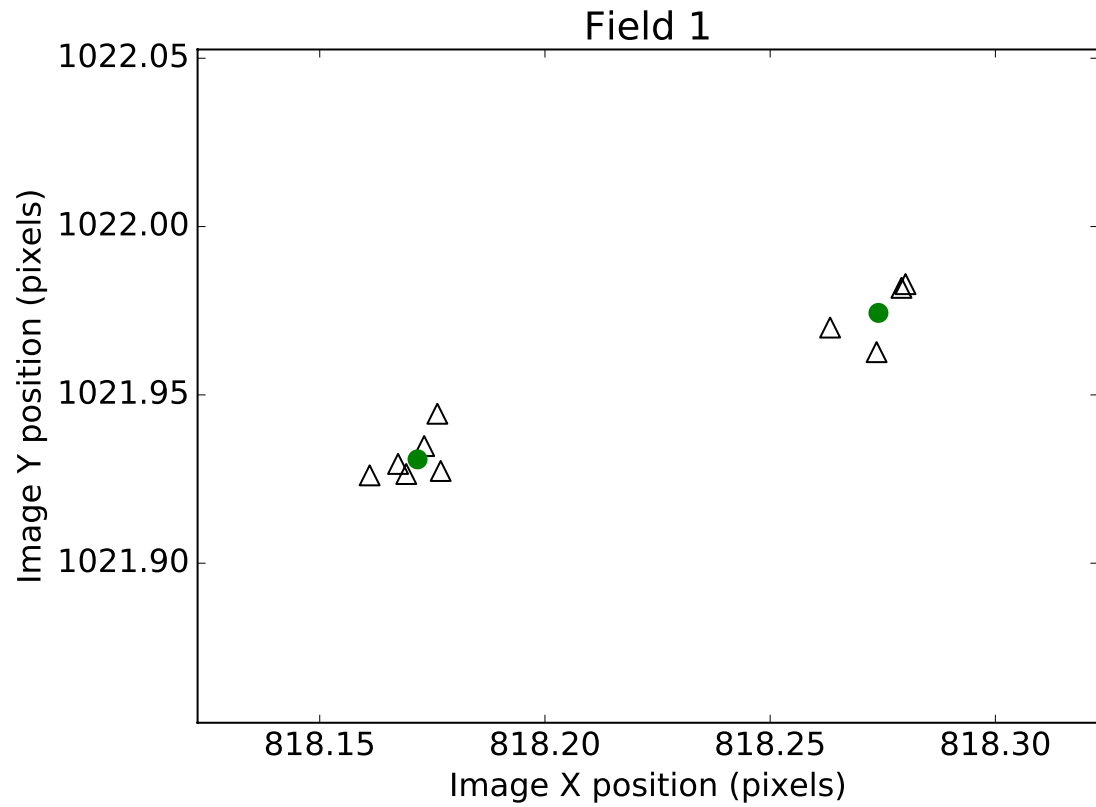


Fig. 2.4.— Positions in the master reference frame of the QSO from each individual dither (black triangles) for Field 1 with the average for each epoch marked by green circle. The "motion" is the inverse of the average motion of the stars, as we measure the QSO position relative to the stellar frame.

in the two epochs with the scatter from the individual images providing an estimate of the uncertainties. Figure 2.4 shows an example for the quasar in Field 1. This difference is then divided by the baseline for the observations of the field, converted to milliarcseconds (mas), and decomposed into the WCS frame using the Position Angle for the observation and then inverted to provide the motion of the stars, rather than the reflex motion of the QSO. We defined a local reference frame of  $\mu_W$  and  $\mu_N$  to account for the impact of declination ( $\delta$ ) on the apparent motion in right ascension ( $\alpha$ ), with  $\mu_W \equiv -(d\alpha/dt)\cos(\delta)$  and  $\mu_N \equiv d\delta/dt$ . The resulting PMs for all successfully measured fields, as well as prior PM measurements for the SMC, are shown in Figure 2.5.

For the final error estimate in each field, we begin with the error in the pixel frame, which has two components. The first component is the standard deviation of the QSO positions, with the error for each epoch added in quadrature,  $\delta\text{PM}_{\text{QSO}}$ . The second component is the scatter in the difference in position between epochs for all stars used in the transformation,  $\sigma_{\langle PM \rangle}$ . By construction, this value should be zero as the stars are aligned to themselves, so the deviation from zero acts as an estimate for the accuracy of the transformation. These two components were added together in quadrature and then converted to  $\mu_W$  and  $\mu_N$ , including a covariance term for the errors to account for the rotation relative to the pixel frame.

Figure 2.6 demonstrates that the transformations worked as intended. The stellar motions cluster around zero (with the median stellar error displayed below the cluster for reference), and the motions derived from the QSOs clearly separate from the motions of the SMC member stars in each field relative to one another.

Table 2.1: New SMC Observations and Results.

ID	R.A.		Decl.		New SMC Proper Motions							
					$\Delta$ time	$N$	PM of Field as Observed					
							$\mu_W$	$\mu_N$	$\delta\mu_W$	$\delta\mu_N$		
h	m	s	Deg	'	''	(yr)		(mas yr <sup>-1</sup> )				
SZ1	0	37	4.7	-73	22	29.6	2.968	710	-0.669	-1.339	0.064	0.067
SZ2	0	38	57.5	-74	10	0.9	2.966	364	-0.436	-1.211	0.068	0.067
SZ3	0	39	47.8	-74	34	44.8	2.993	134	-0.576	-1.471	0.042	0.042
SZ4	0	39	57.6	-73	6	3.6	2.966	978	-0.711	-1.246	0.097	0.102
SZ5	0	42	59.0	-74	2	44.6	2.966	541	-0.568	-1.265	0.100	0.093
SZ6	0	44	40.3	-73	21	51.8	2.962	1095	-0.676	-1.319	0.066	0.055
SZ8	0	45	16.8	-74	42	31.1	2.937	245	-0.657	-1.265	0.049	0.053
SZ9	0	54	23.0	-73	31	0.2	2.974	1475	-0.760	-1.161	0.074	0.083
SZ11	1	0	5.7	-71	57	23.4	2.970	740	-0.770	-1.278	0.070	0.068
SZ12	1	0	18.3	-74	3	22.8	2.999	339	-0.869	-1.127	0.048	0.090
SZ13	1	1	4.7	-73	41	59.9	2.957	563	-0.742	-1.306	0.082	0.076
SZ14	1	2	44.9	-72	15	21.9	2.986	842	-0.863	-1.244	0.034	0.073
SZ15	1	5	22.5	-71	56	49.9	2.989	512	-0.996	-1.197	0.058	0.067
SZ16	1	7	15.6	-74	10	45.3	2.956	157	-0.892	-1.266	0.062	0.063
SZ17	1	7	21.6	-72	48	45.6	2.988	845	-0.830	-1.144	0.040	0.032
SZ18	1	8	25.4	-73	43	17.3	3.004	400	-0.757	-1.339	0.064	0.060
SZ19	1	8	34.8	-71	19	15.5	2.995	232	-0.801	-1.208	0.073	0.092
SZ20	1	11	3.0	-72	20	36.2	2.995	400	-0.901	-1.387	0.056	0.051
SZ21	1	14	45.3	-71	53	40.8	2.989	152	-0.927	-1.239	0.068	0.077
SZ22	1	15	18.7	-73	23	54.6	2.995	237	-0.840	-1.145	0.058	0.054
SZ23	1	15	34.1	-72	50	49.3	2.952	186	-1.000	-1.185	0.071	0.076
SZ24	1	17	1.0	-71	28	35.9	3.012	105	-0.995	-1.264	0.077	0.080
SZ25	1	18	54.5	-74	5	44.8	2.991	75	-0.917	-1.145	0.057	0.066
SZ26	1	20	52.4	-72	3	13.3	2.976	110	-0.902	-1.255	0.056	0.054
SZ27	1	20	56.1	-73	34	53.5	2.987	107	-1.098	-1.196	0.064	0.049
SZ28	1	21	8.4	-73	7	13.1	2.935	89	-0.994	-1.103	0.103	0.093
SZ29	1	24	5.8	-72	39	46.9	2.962	95	-0.869	-1.153	0.110	0.099
SZ30	1	26	2.7	-73	56	3.8	2.979	72	-1.118	-1.307	0.100	0.106

Note. — The identifier used for each data point (the fields or Gaia star ID), and R.A./Decl. of reference source (Columns 1, 2, and 3). Column 4 lists the time baseline, in years, between the epochs used to calculate the PM. Column 5 lists the number of stars used in the final transformations after all cuts and iterations have been applied. Columns 6-9 list the observed PMs and errors.

## 2.3 Proper Motion Results

### 2.3.1 Model Design & Analysis

Including the PM measurements from NK13 and vdMS16 with our new sample, we have a total of 41 data points for describing the motion of the SMC. This affords us the opportunity to consider the complicating factor of motions internal to the SMC when attempting to determine the COM motion. As can be seen from Figure 2.7, residual motions are present and significant.

We fix the radial velocity of the SMC at  $v_{\text{sys}} = 145.6 \pm 0.6 \text{ km s}^{-1}$  (Harris & Zaritsky 2006) and the distance modulus at  $m - M = 18.99 \pm 0.1$  (Cioni et al. 2000). We additionally consider the impact of viewing perspective (projection effects of the 3D COM motion) in the same manner as van der Marel et al. (2002). While the SMC only subtends  $\sim 5$  degrees on the sky, this effect can contribute up to  $\leq 0.16 \text{ mas yr}^{-1}$ , a non-negligible fraction of the measured PMs.

For the SMC center, we test two different positions: the H I kinematical center at  $(\alpha, \delta) = (16.25^\circ, -72.42^\circ)$  (Stanimirović et al. 2004) and the center determined by the structure of the Cepheid population of the SMC at  $(\alpha, \delta) = (12.54^\circ, -73.11^\circ)$  (Ripepi et al. 2017). With the growing body of work suggesting a disconnect between the stellar motions and the underlying H I gas, we felt it prudent to examine the new stellar geometric center in addition to the more traditional H I dynamical center. The locations of both of these centers are shown in Figure 2.8. For the centers, we use a fixed uncertainty of  $0^\circ.2$  for the position.

As discussed in Section 2.1, multiple LOS studies have found evidence for rotation in the SMC. To address this possibility, we test for two different rotation scenarios in our model. For one, we constrain the rotation velocity,  $V_{\text{rot}} = 0 \pm 40 \text{ km s}^{-1}$ ,

Table 2.2: Previous SMC Observations and Results.

ID	R.A.			Decl.			New SMC Proper Motions		PM of Field as Observed			
							$\Delta$ time	$N$	$\mu_W$	$\mu_N$	$\delta\mu_W$	$\delta\mu_N$
Kallivayalil et al. (2013) Proper Motions												
S1	0	51	17.0	-72	16	51.3	1.9	42	-0.682	-1.288	0.100	0.100
S2	0	55	34.7	-72	28	33.9	7.6	25	-0.722	-1.214	0.032	0.024
S3	1	2	14.5	-73	16	26.6	7.7	36	-0.679	-0.974	0.026	0.028
S4	0	36	39.7	-72	27	42.0	2.8	10	-0.460	-1.114	0.109	0.109
S5	1	2	34.7	-72	54	23.8	6.8	30	-0.806	-1.199	0.017	0.038
van der Marel & Sahlmann (2016) Proper Motions												
3934	0	50	31.6	-73	28	42.6	-	1	-0.541	-1.304	0.177	0.177
3945	0	50	38.4	-73	28	18.1	-	1	-0.668	-1.160	0.154	0.148
4004	0	51	24.6	-72	22	58.4	-	1	-0.670	-1.165	0.148	0.143
4126	0	52	51.2	-73	6	53.6	-	1	-0.667	-1.291	0.132	0.116
4153	0	53	4.9	-72	38	0.2	-	1	-0.821	-1.231	0.131	0.130
4768	1	1	17.0	-72	17	31.2	-	1	-1.144	-1.239	0.151	0.143
5267	1	7	18.2	-72	28	3.7	-	1	-0.849	-1.262	0.152	0.144
5714	1	13	30.5	-73	20	10.3	-	1	-0.992	-1.182	0.091	0.082

Note. — Same as Table 2.1.

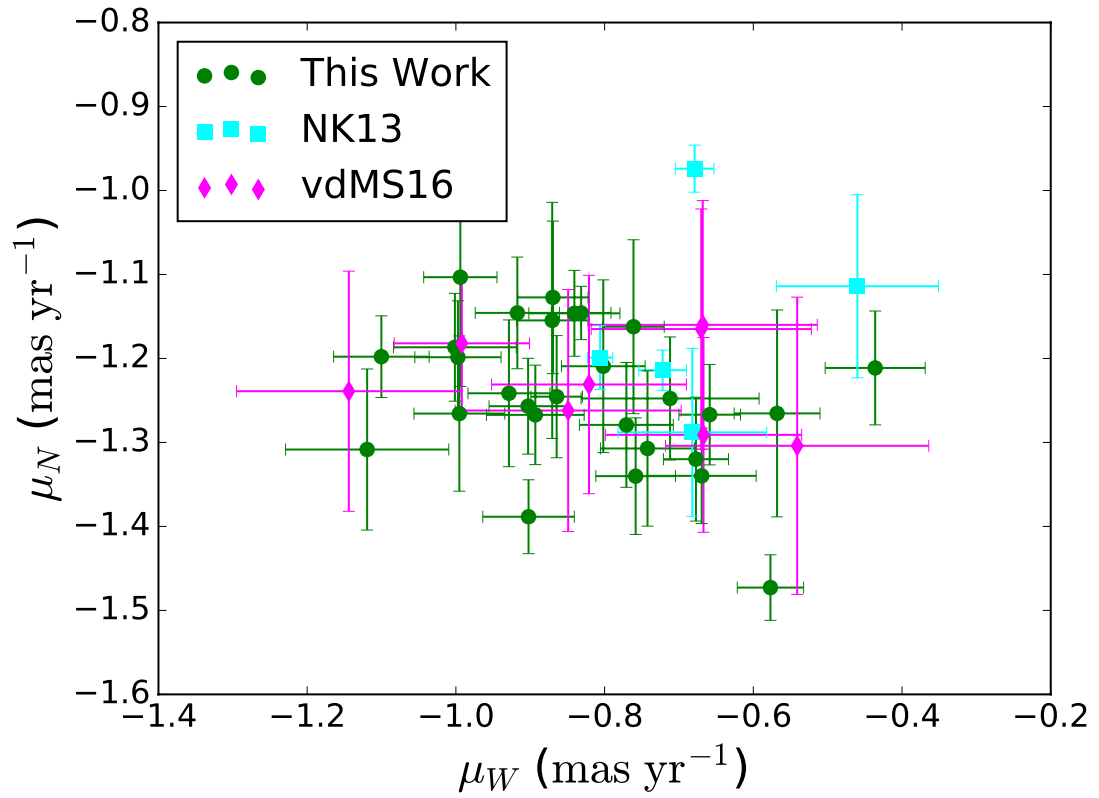


Fig. 2.5.— The measured proper motions for each field (green), along with the earlier measurements by NK13 (cyan) and vdMS16 (magenta).

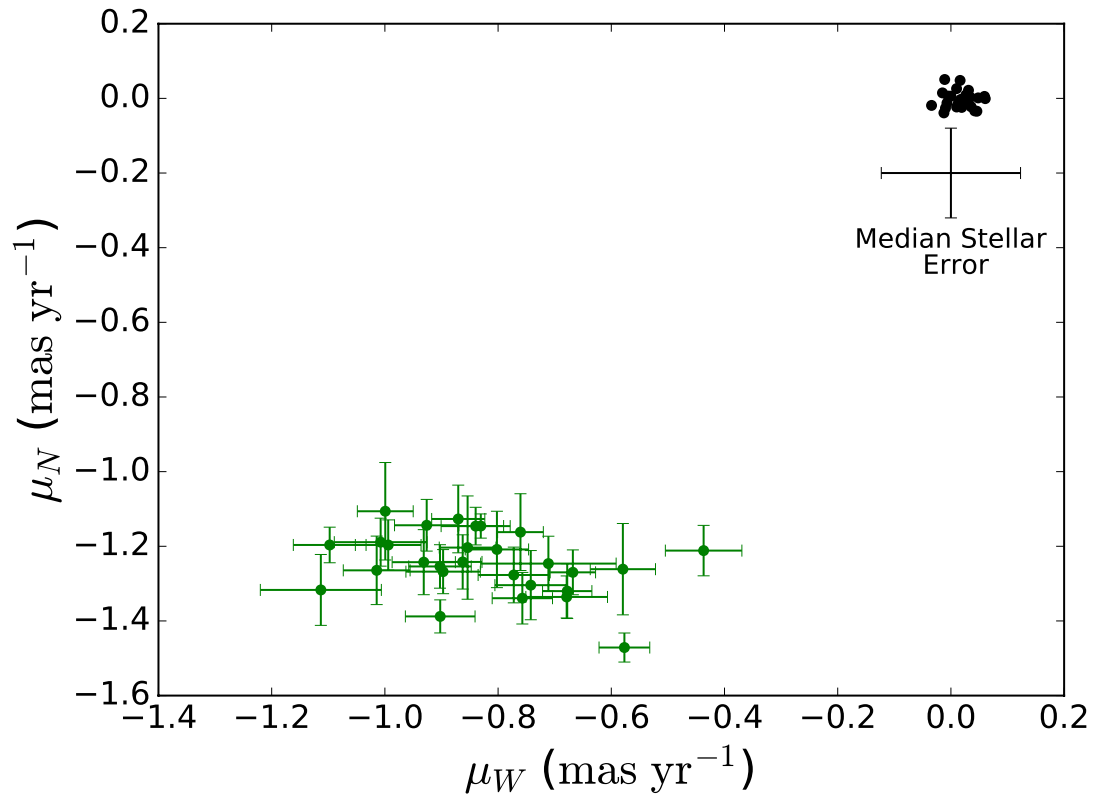


Fig. 2.6.— The motions inferred for each quasar (green points), corrected for the reflex motion, as compared to the median motions for the stars (black points). The median uncertainty for the stars is shown. That the stars cluster close to zero and that the average of the stars is still closer to zero indicates that the transformations have worked as intended.

and for the second option, we allow  $V_{\text{rot}}$  to be a free parameter. For both, we treat the rotation as rising out to a radius of 0.6 kpc and then constant after that. As a fifth case, we also test for allowing both  $V_{\text{rot}}$  and the center position to be free fit parameters. However, we find that the data are unable to provide a useful constraint on the center position, converging to a center close to the H I center but with an uncertainty of 4 degrees.

Most of the LOS studies focused on the innermost two degrees of the SMC, an area that we do not sample well. Instead, most of our statistical leverage comes from the outer regions of the SMC. As we are limited in our sampling density, we opt to keep the inclination of the model near  $0^\circ$ . In total, we have four cases to test, two choices of the SMC center and two options for its internal rotation about each center.

For the COM PM itself, we leave it as a free parameter, optimized by minimizing the model's  $\chi^2$  with respect to the data. The fit statistic is the same as used by van der Marel & Kallivayalil (2014),

$$\chi_{\text{PM}}^2 \equiv \sum_{i=1}^M [(\mu_{W,\text{obs},i} - \mu_{W,\text{mod},i}) / \Delta\mu_{W,\text{obs},i}]^2 + [(\mu_{N,\text{obs},i} - \mu_{N,\text{mod},i}) / \Delta\mu_{N,\text{obs},i}]^2, \quad (2.1)$$

The resulting parameters for the minimized  $\chi^2$  model are used to create mock data, using a Monte Carlo approach. As in NK13, these mock data are used to estimate the uncertainties in the best-fit parameters for the model. Each set of mock data are given uncertainties, drawn from the the observational uncertainties but scaled by a factor of  $(\chi_{\text{min}}^2 / N_{\text{dof}})^{1/2}$  to compensate for any underestimate of the uncertainties, where  $N_{\text{dof}} = N_{\text{data}} - N_{\text{param}} + N_{\text{fixed}}$ , and  $\chi_{\text{min}}^2$  is the minimum fit statistic for the model. We generate and fit multiple sets of mock data, and then we use the dispersion

in the parameters found as an estimate of the random uncertainty.

### 2.3.2 Center of Mass Results

The final best fit parameters for each of the four models are listed in Table 2.3. We see that the choice of the dynamical center does have an effect on the estimated COM PMs, differing by  $\sim 3\sigma$  in  $\mu_W$  and by  $\sim 2\sigma$  in  $\mu_N$ . To reflect this uncertainty in the COM motion, we add a systematic error term to our final PM measurement, which we define as the difference between the best fit PM values for the  $V_{\text{rot}}$  free cases (see the discussion below). For  $\mu_W$  this is  $0.1 \text{ mas yr}^{-1}$ , and for  $\mu_N$  is  $0.03 \text{ mas yr}^{-1}$ . Additionally, the choice of the center seems to affect the likelihood of a detection of a rotation signature when  $V_{\text{rot}}$  is allowed to be free. The H I center converges on  $V_{\text{rot}} = 12 \pm 4 \text{ km s}^{-1}$  (random error only), while the geometrically-determined center is consistent with no rotation,  $V_{\text{rot}} = 0 \pm 4 \text{ km s}^{-1}$  (random error only). When we consider the impact of the systematic error term, both rotation signatures become statistically consistent with no rotation. While the model using the H I center and allowing  $V_{\text{rot}}$  to be free does formally produce the best fit, the differences are not significant (see Table 2.3). This underscores the difficulty of using a simple model to describe the potentially complex nature of the SMC internal kinematics.

We choose the  $V_{\text{rot}}$  free, H I center model for our final estimate and comparison with previous studies (seen in Table 2.4) because it formally has the smallest  $\chi_{\text{min}}^2/N_{\text{dof}}$  and most previous works have adopted the H I dynamical center<sup>1</sup>. All four of our new COM motion estimates are statistically consistent with the prior values found for the SMC given the uncertainties. There is a slight offset between our work and vdMS16 as compared to NK13 and Cioni et al. (2016). In the latter two studies, the

---

<sup>1</sup>We do examine the impact of this choice of dynamical center on our subsequent orbital modeling.

majority of the measurements come from the western half of the SMC, while the first two have more uniform coverage of the whole SMC. This underscores the complex nature of the SMC and the care that must be taken to avoid contamination of the global PM estimate by local motions. As a consistency check, we also consider the 28 new HST fields by themselves. For the two choices of SMC center, and a fixed versus free rotation signal, we find results that agree within the random errors of the full sample. This is perhaps not surprising given that these 28 fields account for the majority of the 41 total measurements considered here.

For the TGAS PM errors, a systematic effect that is not explicitly included is possible spatial correlations in the PM errors (Lindegren et al. 2016). The effect of such correlations would be to underestimate the random error in the weighted average PM of the sample. However, the agreement between the TGAS and HST results shows that any residual systematic errors must be below the random errors. Similarly for the HST data, the main possible residual systematic errors are from the geometric distortion solution and charge transfer efficiency effects. Both are expected from Bellini et al. (2011) and Anderson (2014) to be below our random errors. The main systematic uncertainty, which is larger than our random errors, comes from not being able to establish a dynamical center for the SMC from our data alone.

## 2.4 Internal Kinematics

### 2.4.1 Full Star Sample

We can now subtract the global COM PM, including the perspective motion, to find the internal motions of the SMC. The result is shown in Figure 2.7. In addition to the calculated vectors, the observational error is also shown so that the significance

of a particular vector can be evaluated.

At first glance, there does not appear to be any coherent rotational structure to the residual vectors. As an alternative visualization, we decompose each field into its radial and tangential components,  $\mu_{\text{res,rad}}$  and  $\mu_{\text{res,tan}}$  respectively, as a function of distance from the center, and calculate the error-weighted mean and the error for the weighted mean, shown in Figure 2.9. In calculating the error-weighted mean, we exclude any fields not consistent with zero to within twice the observational error. For the radial component, we find for the H I center  $\bar{\mu}_{\text{res,rad}} = 0.027 \pm 0.010$  mas yr<sup>-1</sup> and for the Ripepi et al. (2017) center  $\bar{\mu}_{\text{res,rad}} = 0.015 \pm 0.010$  mas yr<sup>-1</sup>. For both centers, a radial motion greater than zero is preferred, consistent with a tidally disrupting system. For the tangential component, we find for the H I center  $\bar{\mu}_{\text{res,tan}} = 0.008 \pm 0.010$  mas yr<sup>-1</sup> and for the Ripepi et al. (2017) center  $\bar{\mu}_{\text{res,tan}} = 0.001 \pm 0.010$  mas yr<sup>-1</sup>. If a rotation signal were present, the fields would be offset from zero, but both means are consistent with zero.

In the southwest and southeastern regions, large and statistically significant residuals can be seen. For the southeastern region, this coincides with the direction towards the Magellanic Bridge (shown in Figure 2.8), peaking around 80 km s<sup>-1</sup>. This is the first measured stellar motion away from the SMC and towards the Bridge. In the southwestern region, the strong coherent motions appear to be coincident with the “Western Halo,” identified by Dias et al. (2016). The other potential dynamic signature, the “Counter-Bridge” (e.g., Besla 2011), which is predicted in the northeastern section of the SMC, does not appear as a prominent feature in our data. Either the way, the general finding of ordered mean motion radially away from the SMC in the outer regions of the galaxy, provides kinematic evidence that the SMC is in the process of tidal disruption.

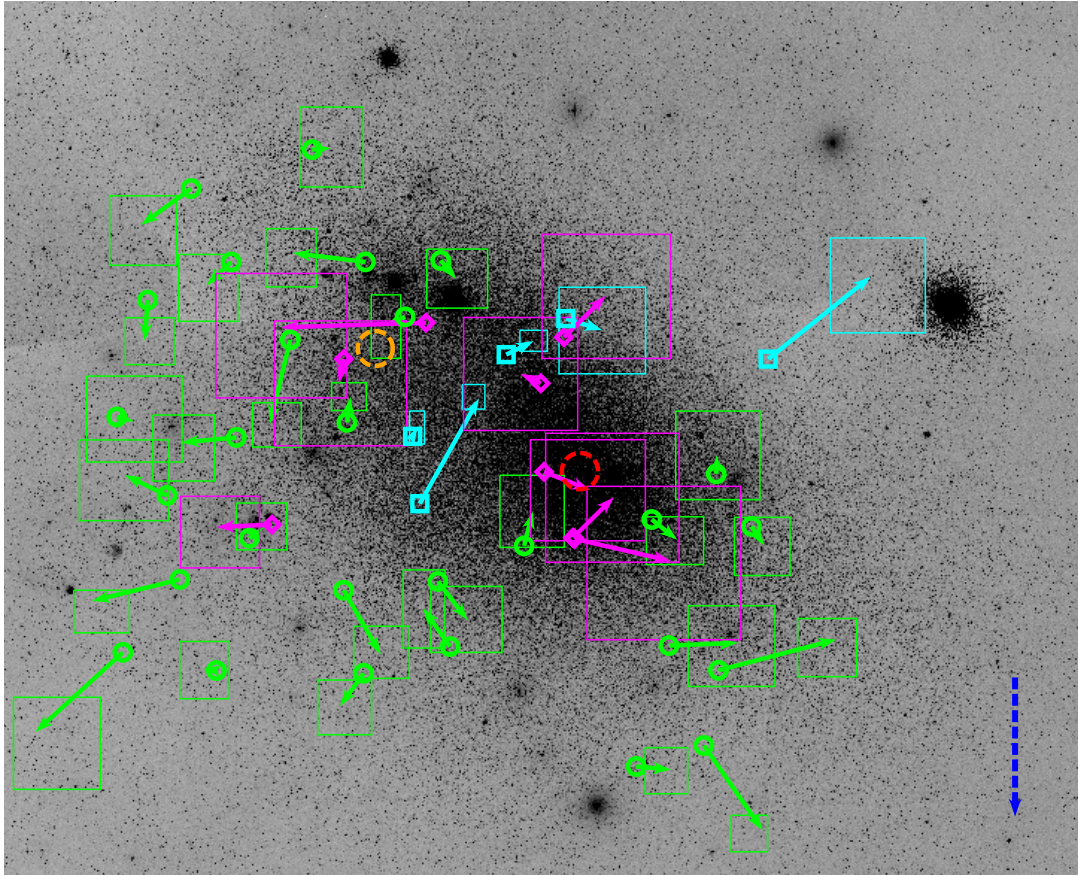


Fig. 2.7.— The residual motion vectors calculated after subtracting our adopted COM motion determined in this study. Similar to Figure 2.1 the green, cyan, and magenta measurements are this study, NK13, and vdMS16, respectively. The boxes indicate the uncertainty in the motion for that field where a vector that exceeds its box corresponds to a residual vector of greater than one  $\sigma$ . A reference vector of  $100 \text{ km s}^{-1}$  is shown at the bottom right, and the two centers used for the models are shown as well with the H I derived center marked by the dashed orange circle and the Ripepi et al. (2017) center marked by the dashed red circle. For orientation, north is up and east is to the right.

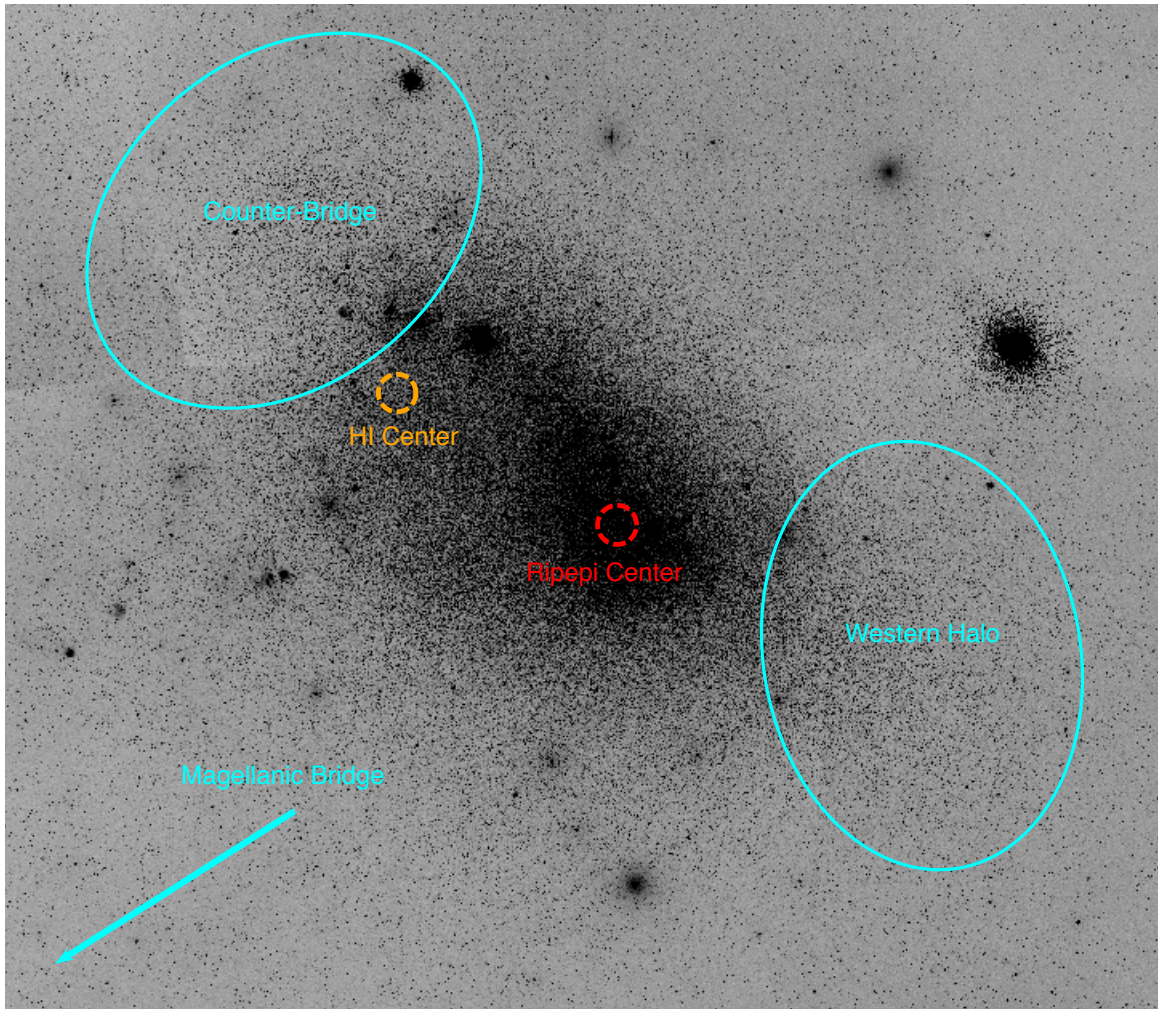


Fig. 2.8.— The locations of the two centers tested: the H I derived center (dashed orange circle) and the Ripepi et al. (2017) center (dashed red circle). Three areas with potential kinematic signatures are also marked. The regions considered to be the Counter-Bridge and Western Halo are marked by the cyan ellipses, and the direction towards the Magellanic Bridge is marked by the cyan vector. For orientation, north is up and east is to the right.

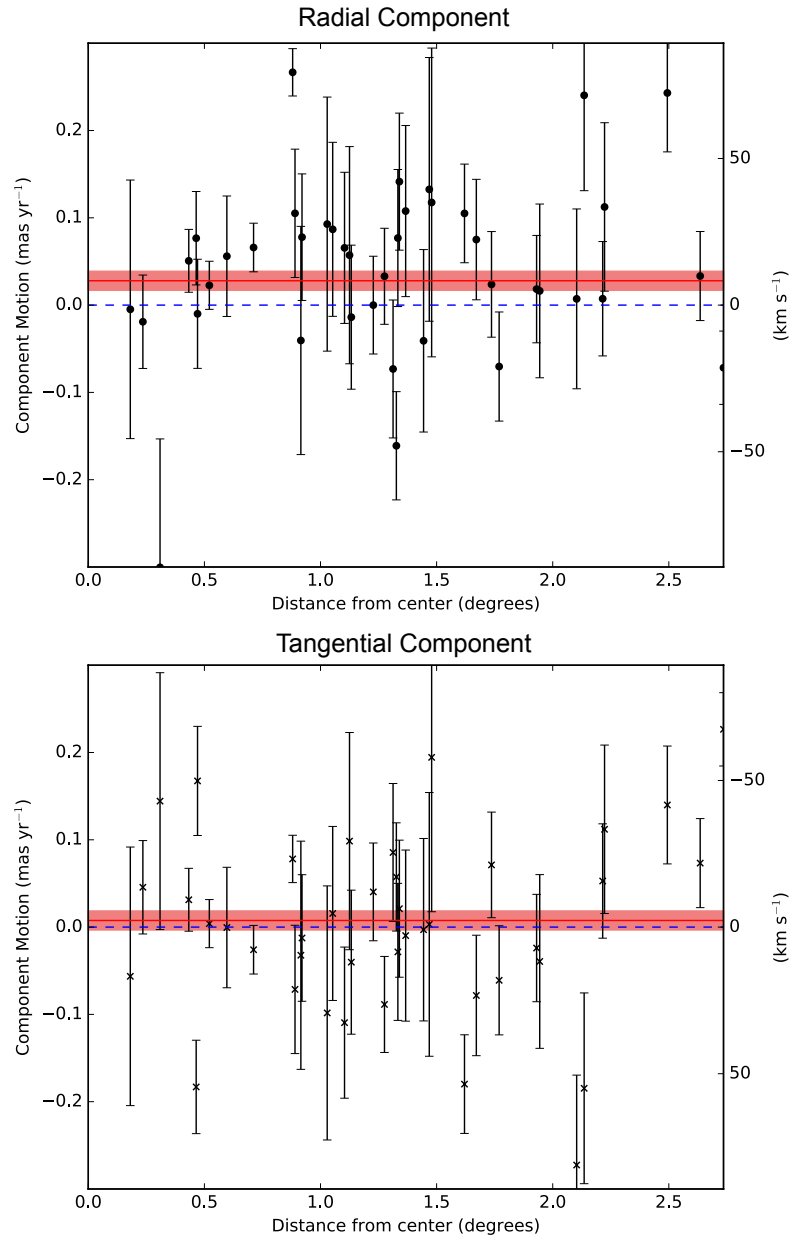


Fig. 2.9.— Amplitudes for the radial (top) and tangential (bottom) components of the residual motions for the H I center,  $V_{\text{rot}}$  free model, as a function of distance from the center. For calculating the error-weighted mean, we exclude any fields not consistent with zero to within twice the observational error. The resulting error-weighted mean is indicated by the red line and the error of the weighted mean is shaded above and below the line.

The combination of the amplitude of these residual vectors and their spatial coherence suggest the possibility of some of these fields being unbound from the SMC. To provide a physical sense for what might be unbound, we estimate the escape speed. We relate the escape speed  $v_e$  to the circular velocity  $v_c$  under the simple assumption of a Kepler potential, for which

$$\frac{v_e^2}{2} = \frac{GM}{R}, v_c^2 = \frac{GM}{R}, \quad (2.2)$$

so that  $v_e = \sqrt{2}v_c$ . For  $v_c$ , we use results from van der Marel & Franx (1993) to relate it to the LOS velocity dispersion  $\sigma_{\text{LOS}}$ . If we assume an isotropic velocity distribution and a density profile of  $r^{-3}$ , from Eq. (B6b) in van der Marel & Franx (1993) we find  $\sigma_{\text{LOS}} = \sqrt{\pi/16} v_c$ . Combining these two relations together, we get  $v_e = 3.19 \sigma_{\text{LOS}}$ . Using the measurement from Dobbie et al. (2014) for  $\sigma_{\text{LOS}} \approx 26 \text{ km s}^{-1}$ , we find a final  $v_e \approx 83 \text{ km s}^{-1}$ . We note that this is a lower limit, since realistic potentials are more extended than a Kepler potential, but it provides a useful intuition for the state of the SMC. Several of our fields have a total residual motion consistent with this estimate of the escape velocity. This provides kinematical evidence that the stars there could be unbound. This is consistent with the fact that other material from the SMC that is now at larger radii than the radii where we are probing, must have become unbound to form the Magellanic Stream and Magellanic Bridge.

We wanted to examine the impact on the COM PM from narrowing our choice of fields included. For stars in equilibrium around the COM, one expects to measure a radial PM residual of zero, calculated as in Figure 2.9. So we discard all fields for which the residual is not consistent with zero to within twice the observational error. This excludes five fields, 2 from our new sample, 1 from vdMS16, and 2 from NK13. After fitting our model to this restricted subsample, the resulting COM PMs do not

significantly vary from the original values for their respective centers. The choice of center has a bigger effect on our data than this difference in field selection.

### 2.4.2 Red vs Blue Stellar Motion

With multiple LOS studies in potential tension over the behavior of different stellar populations in the SMC, as discussed in Section 2.1, we wanted to explore our data's ability to constrain this problem.

We selected samples of red and blue stars, separated by a color of  $(F606W - F814W) = 0.45$  and with  $F606W < 21$  mag, as shown in Figure 2.10. This cleanly delineates the two populations, and we will refer to these as the red and blue populations. For a proper motion to be calculated, we also require that the field has a minimum of ten stars in each subsample.

For each population of stars, we repeated the process of iteratively transforming the source positions into a master frame, as described in Section 2.2.3. Due to the smaller number of fields with enough stars, we calculated a simple weighted average for the systemic motion of the fields and use that, along with the contributions from SMC geometry (viewing perspective) calculated from the model, to create residual motions as a function of color. For the red population, the resulting systemic motion is  $\mu_W = -0.72 \pm 0.06$  mas yr<sup>-1</sup> and  $\mu_N = -1.23 \pm 0.08$  mas yr<sup>-1</sup>, while the blue population was found to have an average motion of  $\mu_W = -0.81 \pm 0.06$  mas yr<sup>-1</sup> and  $\mu_N = -1.24 \pm 0.08$  mas yr<sup>-1</sup>. These estimates are statistically consistent but the differences may be real. The fields with a large enough number of red stars tend to lie towards the southwestern portion of the SMC, while the fields that have enough blue stars lie towards the eastern side of the SMC. More western fields will bias the average motion towards a greater western motion (a smaller  $\mu_W$ ) while more fields

near the Bridge will bias it in the opposite direction.

Indeed, when we examine fields that have both red and blue stars we see that for many of the fields there are no significant differences between the motions of the populations (see Figure 2.11). Only for the highest field numbers, corresponding to fields on the outer edges of the SMC, do we note a significant difference. Unfortunately, those fields are also among the sparsest, often falling on the threshold of the ten required stars. While the ability of WFC3/UVIS to detect enough stars to be able to distinguish between different stellar populations in the SMC is exciting, these results suggest it will require much better coverage of the entire SMC, rather than the pencil beam investigation undertaken here, to discern a difference between the populations, if one exists.

## 2.5 Orbit Implications

The past orbits of the LMC-SMC system about the Milky Way have been explored in many previous works. These have tended to concentrate on the more massive member of the pair, for instance, evaluating whether the LMC is on a first passage (Besla et al. 2007; NK13), exploring whether the presence of the LMC influences the dynamics of other MW satellites or even the MW-LMC barycenter or MW disk (Vera-Ciro et al. 2013; Gómez et al. 2015; Patel et al. 2017; Laporte et al. 2017, 2018), and exploring substructure that might have come in with the LMC (Sales et al. 2011; Yozin & Bekki 2015; Jethwa et al. 2016; Sales et al. 2017; Fritz et al. 2017a,b). However, the relationship of the Clouds to each other, specifically how long they have been a binary, and how closely they may have interacted in the past, is still relatively unexplored and unconstrained (e.g., Besla et al. 2012; Diaz & Bekki 2012). Our new data afford us a much better constraint on the past interactions between

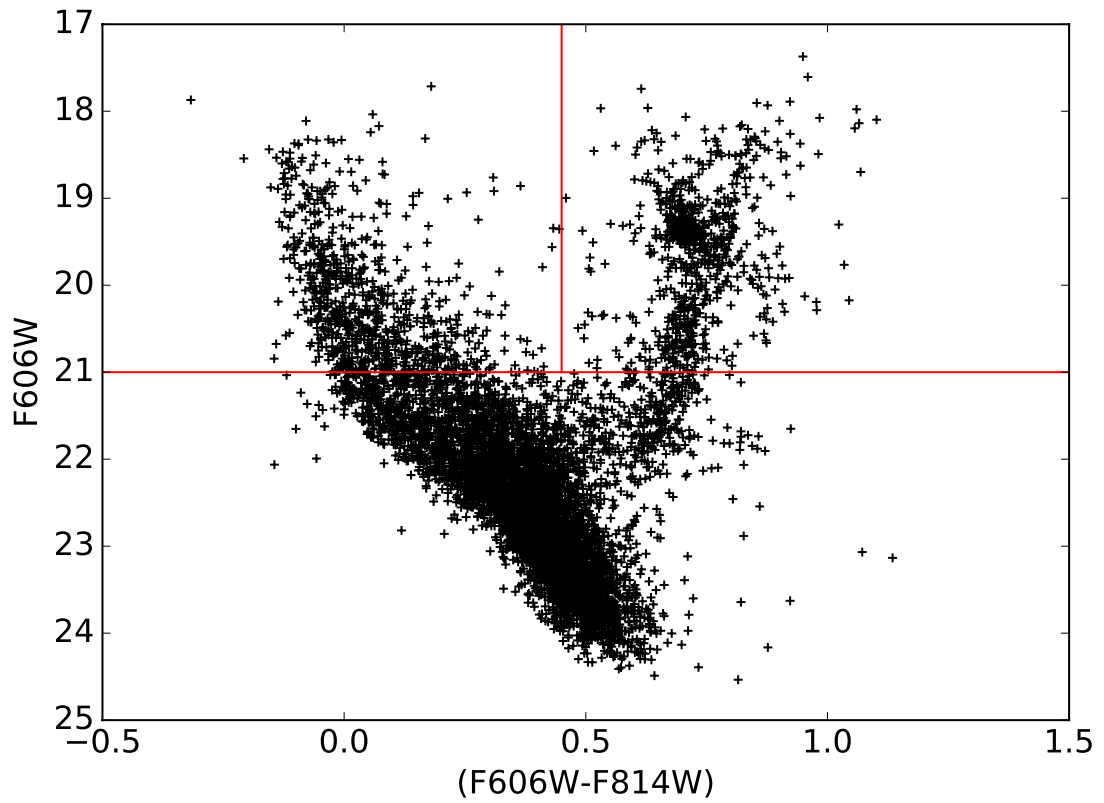


Fig. 2.10.— The composite CMD for all new SMC fields. The dividing lines for the red and blue subpopulations, examined in Figure 2.11, are marked at  $(F606W-F814W)=0.45$  and  $F606W < 21$  mag.

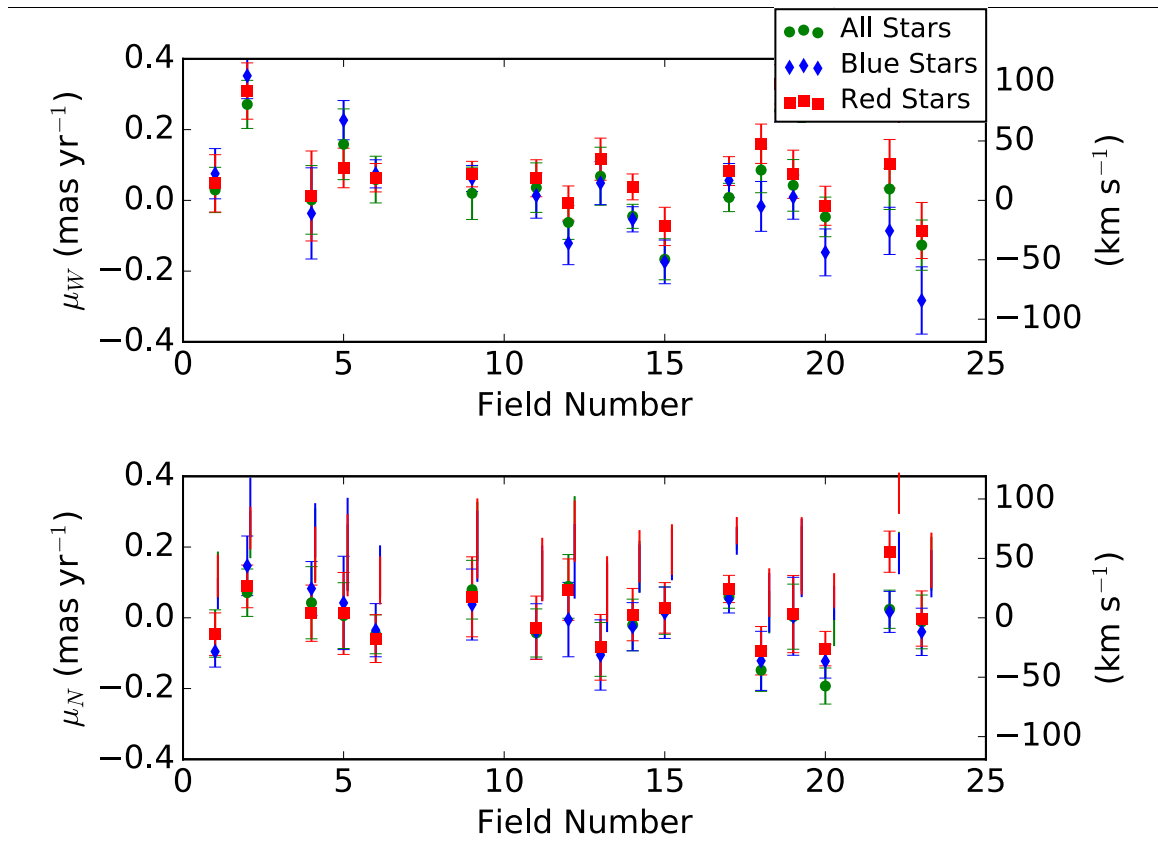


Fig. 2.11.— Residual proper motions in the E-W (top) and N-S (bottom) directions for all fields with enough red and blue stars for the transformations. There are essentially no statistically significant differences between the different populations.

the Clouds themselves. In particular, the impact parameter and timing of the last encounter between the Clouds is critical to our understanding of the formation of the Magellanic Bridge and the internal structure of both galaxies (e.g., Bekki & Chiba 2007, Yoshizawa & Noguchi 2003, Gardiner & Noguchi 1996, Besla et al. 2016, Diaz & Bekki 2012, Pardy et al. 2018, Guglielmo et al. 2014, Ružička et al. 2010), and this is where we focus our modeling efforts.

### 2.5.1 Methodology

Our orbital modeling procedure is basically identical to that in NK13, and we refer the interested reader to that work for the particulars. The MW is modeled as an axisymmetric three-component potential with a Navarro-Frenk-White (NFW) halo (Navarro et al. 1996, 1997), Miyamoto-Nagai disk (Miyamoto & Nagai 1975) and a Hernquist bulge (Hernquist 1990). The NFW halo is adiabatically contracted to account for the presence of the disk (Gnedin et al. 2004), and the NFW density profile is also truncated at the virial radius. We explore two such MW models that span the mass range of recent studies: a light model with a total virial mass of  $1 \times 10^{12} M_{\odot}$ , and a heavy model with a mass of  $2 \times 10^{12} M_{\odot}$  (e.g., Bland-Hawthorn & Gerhard 2016). As we saw in NK13, a high-mass MW tends to disrupt the LMC-SMC binary in the past, while it is easier for them to have been bound for longer in a low-mass MW model.

Our LMC model is slightly different than used in NK13, but still spans a low and high-mass range. It is less likely that the LMC and SMC have been a long-lived binary if the LMC mass is low, and much more likely if the LMC mass is high. Our low-mass LMC model of  $3.7 \times 10^{10} M_{\odot}$  comes from requiring the rotation curve to be flat at a value of  $91.7 \text{ km s}^{-1}$  (van der Marel & Kallivayalil 2014) out to 20 kpc. To

make sure that the adopted mass profile matches the dynamical mass of  $1.3 \times 10^{10} M_{\odot}$  at 9 kpc (van der Marel et al. 2009), the LMC is modeled as a Plummer potential with a softening length of 9 kpc. Our high-mass LMC of  $1.8 \times 10^{11} M_{\odot}$  is motivated by the minimum LMC mass that allows the LMC and SMC to have been a long-lived binary even in the presence of a massive MW (NK13) and cosmological expectations (Moster et al. 2013). Here, the LMC is also modeled as a Plummer potential with a softening parameter of 20 kpc. As in NK13 the SMC mass is assumed to have been tidally-truncated by the LMC at early times, and its mass is kept fixed at  $3 \times 10^9 M_{\odot}$  (Stanimirović et al. 2004).

We draw 10,000 random values for the LMC and SMC PMs (NK 13 and this work, respectively), distances (Freedman et al. 2001, Cioni et al. 2000), and line-of-sight velocities (van der Marel et al. 2002; Harris & Zaritsky 2006). The Galactocentric distances and velocities are calculated using the same conventions as in NK13. Since the LMC PM is the same as in that work, we also use the same Solar parameters for consistency (McMillan 2011). These values are broadly consistent with other studies such as that of Bovy et al. (2012). This Monte Carlo method allows us to properly take into account any covariances in the uncertainties of the measured parameters of the Clouds and the Sun. The resulting mean values for the present-day Galactocentric velocity and relative velocity are shown in Table 2.5. We then follow the orbits of the LMC and SMC backwards in time for the four combinations of LMC and MW mass models.

## 2.5.2 Impact parameter and timing of the last SMC-LMC encounter

We are interested to see if we can constrain the likelihood of a past collision between the Clouds. We therefore keep track of the minimum separation achieved between the Clouds in the past, and the time of that “encounter.” As expected, the extremes of the possible distributions in this encounter come from a low-mass LMC with a high-mass MW, and a high-mass LMC with a low-mass MW. We therefore only show the outcomes for these two mass combinations in Figure 2.12. We find that the choice of SMC center makes no discernible difference – the minimum separations and encounter times agree to within the errors – and so we show the results for the H I center only.

In Figure 2.12, we show the LMC-SMC separation at the last close encounter (in kpc), versus the time of the last encounter (Myr in the past), color-coded by the present-day relative velocity between the Clouds ( $\text{km s}^{-1}$ ). For both mass combinations, there is a strong trend with relative velocity, with the highest relative velocities resulting in the most recent and closest encounters. The fact that the highest relative velocities result in the most recent past encounters makes more obvious sense, but the reason that they also result in the closest encounters between the Clouds is because the highest relative velocities correspond to the largest angles between the LMC and SMC velocity vectors today.

The majority of cases (97%) result in a past encounter in which the centers of the Clouds come closer to each other than 20 kpc, which is the currently observed northern extent of the LMC disk (Mackey et al. 2016). This result is robust to choices in MW and LMC mass. Specifically, the minimum separation between the centers of mass of the two Clouds has a mean value of  $7.5 \pm 2.5$  kpc about  $147 \pm 33$  Myr ago in the case of the heavy LMC and light MW model, and  $9.7 \pm 4.5$  kpc about

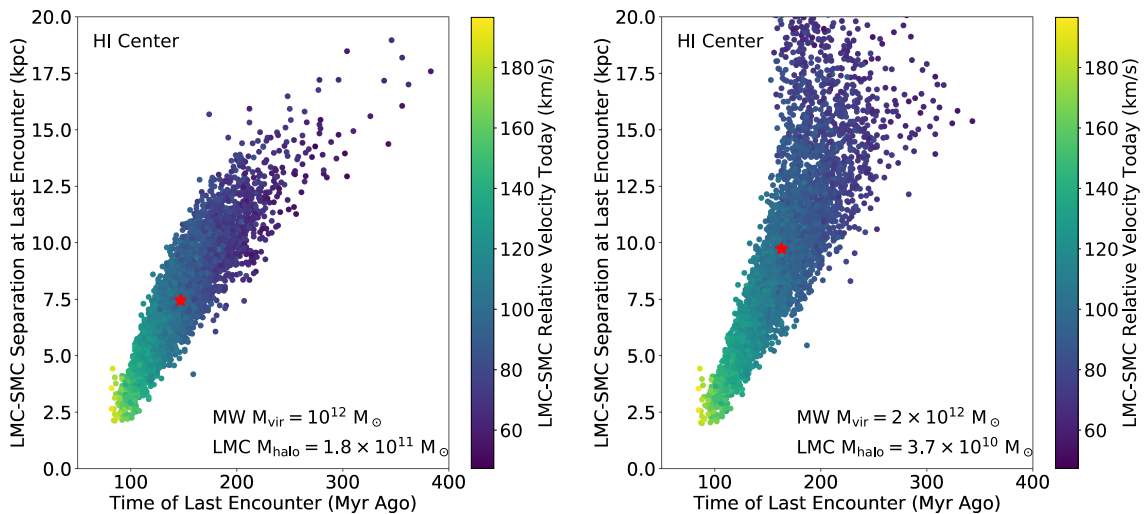


Fig. 2.12.— The LMC-SMC separation at their last encounter as a function of the time of the last encounter, color-coded by the present-day relative velocities between the LMC and SMC (in  $\text{km s}^{-1}$ ). The panel on the left shows results for integrations assuming a MW virial mass of  $10^{12} M_{\odot}$  and an LMC halo mass of  $1.8 \times 10^{11} M_{\odot}$ , on the lower (larger) end of MW (LMC) mass possibilities in the literature. The panel on the right is for a heavier MW virial mass of  $2 \times 10^{12} M_{\odot}$  and a lighter LMC halo mass of  $3.7 \times 10^{10} M_{\odot}$ , on the larger(lower) end of possible MW(LMC) masses. The red star indicates the mean value in each case. Impact parameters higher than 20 kpc are found to be highly unlikely. Impact parameters as small as 2.5 kpc and as recent as 100 Myr are possible, but a bulls-eye hit (0 kpc impact parameter) is unlikely.

$163 \pm 36$  Myr ago in the case of the light LMC and heavy MW model. In both of the considered mass cases, the smallest separation achieved is  $\sim 2$  kpc, indicating that the Clouds could have experienced a direct collision, but a bulls-eye hit (0 kpc impact parameter) is unlikely. Also, only 3% of cases have minimum separations larger than 20 kpc, for all mass combinations considered.

It seems extremely likely that the Clouds have hit each other (since the LMC's disk radius is 18.5 kpc Mackey et al. 2016). The fact that the SMC is in reality an extended body, and here we plot only the separation of the center of masses, strengthens this argument further. This result is consistent with the model of Besla et al. (2012), specifically their Model 2, in which the LMC and SMC pair have experienced a recent direct collision roughly 100 Myr ago which also produces the off-center stellar bar and one-armed spiral of the LMC (see also Pardy et al. 2016; Bekki & Chiba 2007).

In previous work the timing of the last encounter has been estimated at  $< 300$  Myr based on the age of stellar populations in the bridge (Harris & Zaritsky 2006). The previous PMs (Kallivayalil et al. 2006b) were consistent with a timing of  $\sim 150$  Myr ago (see Růžička et al. 2010), but now the error bars on this PM estimate are lower, supporting a very recent encounter. Interestingly, if you make the simple assumption that the radial expansion velocity is comparable to the tangential signal ( $\sim 80$  km  $s^{-1}$ ), in the 150 Myr since the SMC would have expanded roughly 12 kpc. With the deep line-of-sight extension in the eastern region of  $\sim 23$  kpc (Nidever et al. 2013) and assuming an intrinsic size for the SMC of  $\sim 10$  kpc (found in the western region by Mackey et al. 2018), this leaves an unaccounted for expansion of  $\sim 13$  kpc which roughly coincides with our preferred timing and expansion velocity. Note that this encounter is still before the pericentric approach of the LMC to the MW (which happened  $\sim 50$  Myr ago). Also previous works typically take the impact parameter

to be around 10 kpc or larger (Růžička et al. 2010; Diaz & Bekki 2012). Now we have both refined the impact parameter to be smaller as well as ruled out larger impact parameters, supporting a collision model.

## 2.6 Discussion & Conclusions

We have analyzed two epochs of PM data for 30 new fields in the SMC with *HST* WFC3/UVIS. We combine these data with previous *HST* PM results from NK13 and *Gaia* PM results from vdMS16 to create the largest PM data set yet for the SMC. Here we summarize our results, the new implications for the SMC’s history with the LMC, and future directions for the work.

### 2.6.1 Conclusions for PMs

With the  $\sim 3$  year baseline, our analysis gives results that have a range of errors comparable to the errors from NK13. In fields with a large number of stars in the final transformation, we find errors of order  $\sim 0.03$  mas yr $^{-1}$ , similar to those for the  $\sim 7$  year baseline measurements from NK13. Where our fields become sparser, our errors increase towards a maximum comparable to the errors from NK13,  $\sim 0.1$  mas yr $^{-1}$ , that also had relatively sparse star fields and a shorter baseline.

We have successful measurements for 28 of the 30 fields (as explained in Section 2.2), and we combine this data set with the PMs from NK13 and vdMS16 to improve our sampling of the SMC and more tightly constrain the estimate for the SMC COM PM. We fit this data set to a model for the SMC similar to the one laid out in van der Marel et al. (2002), leaving only the PM of the SMC and a possible rotational velocity as free parameters. We find that our dataset by itself does not allow us to independently determine the dynamical center of the SMC to better precision than

previous works. Instead, we adopt two different centers, the dynamical H I center and the geometric center determined in Ripepi et al. (2017). We find that the choice of center has an impact on the estimate of the COM motion, reflected in our systematic error. We find no compelling evidence for internal rotation, with a maximum rotation signal  $V_{\text{rot}} = 12 \pm 4 \text{ km s}^{-1}$  when the H I center is used. The resulting COM PMs roughly agree with all previously published values, though our random errors are several times smaller than the previous most precise measurement. This is primarily due to the increase in the size of the data set fit to the model. Soon after submission of this work, Niederhofer et al. (2018) presented VMC-based PMs for a  $3 \times 3$  degree region of the SMC. We do not attempt a detailed comparison here but their COM PM is marginally consistent with ours given the errors, however, they do not detect an outward residual motion towards the Bridge.

The small per-field errors allow us to probe the internal motions of the SMC, a galaxy whose internal structure is still quite unconstrained. We decompose the residual motion of each field (after subtraction of the COM motion) into a radial and a tangential component. We search for signs of rotation that would manifest as a signal in the tangential component as a function of distance from the SMC center. We see no clear trend in the tangential component. We instead find evidence for large residual motions towards the east and west of the galaxy. The eastern residual motions, on the order of  $\sim 80 \text{ km s}^{-1}$ , point in the direction of the Magellanic Bridge. We estimate the escape speed from the SMC (see Section 2.4.1) and examine the impact of limiting the fields used in the COM PM calculation. We find that the removal of potentially unbound fields has little impact on the COM PM values. The areas of large residual motions also help explain the small differences in previous COM PM measurements, as both NK13 and Cioni et al. (2016) largely sampled the central and western regions

of the SMC, which would not contain the significant residual motions seen in the eastern fields.

This underscores the necessity of sampling a broad area of the SMC in determining a COM motion while also raising new questions about how to best build a model to fit the SMC moving forward. Previous LOS attempts to study SMC structure (e.g., Dobbie et al. 2014; Evans & Howarth 2008) focused on the inner few degrees, where they did find a potential rotation signal. Our data set does not significantly probe the interior of the SMC, so we are unable to provide any further comparisons with these works. Finally, we also test whether different stellar populations in the SMC have measurable differences in their PMs. We employ the simple CMD cut shown in Figure 2.10 to select a ‘blue’ and a ‘red’ stellar population, and re-derive the PMs for each field using these subsamples of stars. We do not find any statistically-significant differences between the measured PMs for these two populations.

## 2.6.2 Conclusions for Implied Orbit

Using the measured PMs, we find new Galactocentric velocities for the SMC and examine the consequences for its recent interaction history with the LMC. Our improved coverage of the SMC significantly improves our overall accuracy of the relative velocity between the two Clouds.

Using this new relative velocity and two different mass cases for both the LMC and MW, we find a strong case for close interaction between the Clouds in the recent past (their centers of mass come within  $\sim 20$  kpc for 97% of all cases examined). The mean COM distance is consistent within the errors across the two mass combinations that we consider, one with a heavy LMC and light MW ( $7.5 \pm 2.5$  kpc  $147 \pm 33$  Myr ago), and a light LMC and a heavy MW ( $9.7 \pm 4.5$  kpc  $163 \pm 36$  Myr ago), strongly

supporting the idea of a direct collision between the Clouds. These impact parameters and encounter times depend little on our model for the internal PMs of the SMC. This lends support to the model of Besla et al. (2012), where the Clouds have recently had a very close interaction, and where the LMC is thus primarily responsible (as opposed to the MW) for the morphology of the SMC, the Magellanic Stream and Bridge. This direct collision also has consequences for the morphology of the LMC.

### 2.6.3 Future Work

We have presented an expanded picture of the PMs in the SMC, revealing its complicated dynamical nature. An immediate consequence of this is the necessity for a higher degree of spatial resolution. Improved resolution would help to disentangle where the ordered motion radially away from the SMC begins and where there may be more coherent stellar rotation, if it exists in the SMC. Studies have shown an increasingly elongated picture of the SMC (e.g., Ripepi et al. 2017), so the combination of a higher PM spatial resolution with LOS studies could help create a data set that would have the power required to clearly identify the dynamical center of the SMC. The upcoming *Gaia* Data Release 2 will provide the next opportunity.

We have better constrained the interaction history of the LMC and SMC. In future work, we will use this assumption to estimate the mass of the LMC enclosed within the SMC orbit. The mass of the LMC has been of considerable interest, first because it further constrains whether the Clouds are on their first or second passage about the MW, but it is also needed to ascertain the LMC's effect on the dynamics of the MW and its satellite population (e.g., Gómez et al. 2015; Peñarrubia et al. 2016), and to better constrain how much debris came in with the LMC itself (e.g., Sales et al. 2017).

The direct collision between the Clouds that we discover here should also inform studies of star formation in the Clouds. We are able to determine a rough timescale for this encounter, and therefore correlations can be made between the past orbits of the Clouds and their star and cluster formation history. Already there is evidence that the locations and age gradients in the SMC star cluster population (Dias et al. 2016) coincide well with the locations of our measured radial motions outwards in the outer regions, prima facie evidence that the ongoing interaction between the Clouds is inducing cluster formation. Future work combining these two datasets, the cluster population and SMC internal dynamics, provides a new opportunity to study the nature of star formation in an environment different than the posterchild Antennae galaxies.

Table 2.3: SMC Best-Fit Parameters.

(1)	Center		H I	H I	R17	R17
(2)	$V_{\text{rot}}$		Constrained	Free	Constrained	Free
(3)	$\mu_W$	mas yr <sup>-1</sup>	$-0.80 \pm 0.11$	$-0.83 \pm 0.02$	$-0.74 \pm 0.03$	$-0.73 \pm 0.02$
(4)	$\mu_N$	mas yr <sup>-1</sup>	$-1.21 \pm 0.04$	$-1.21 \pm 0.01$	$-1.25 \pm 0.13$	$-1.24 \pm 0.02$
(5)	$\mu_{\text{tot}}$	mas yr <sup>-1</sup>	$1.45 \pm 0.12$	$1.47 \pm 0.02$	$1.45 \pm 0.13$	$1.45 \pm 0.03$
(6)	$V_{\text{rot}}$	km s <sup>-1</sup>	—	$-11.6 \pm 4.0$	—	$-0.3 \pm 3.5$
(7)	$(\chi_{\text{min}}^2/N_{\text{dof}})^{1/2}$		2.32	2.29	2.32	2.37

Note. — Line 1 indicates the center used in the model as described in Section 2.3.1, and line 2 indicates whether  $V_{\text{rot}}$  was left free or constrained to  $0 \pm 40$  km s<sup>-1</sup>. Lines 3-6 are the best fit values for  $\mu_W$ ,  $\mu_N$ ,  $\mu_{\text{tot}}$ , and  $V_{\text{rot}}$ , respectively, for the four models. The units for each parameter are listed in the adjacent column. Line 7 is the statistic used to assess the quality of fit of the model to the data, described in Section 2.3.1. R17 refers to the estimate of the center of the SMC from Ripepi et al. (2017).

<sup>a</sup> Refers to Ripepi et al. (2017)

Table 2.4: SMC Center of Mass Proper Motions.

Work	Data	$\mu_W$ (mas yr <sup>-1</sup> )	$\mu_N$ (mas yr <sup>-1</sup> )
<b>This Paper</b>	<i>HST+Gaia</i>	$-0.83 \pm 0.02$	$-1.21 \pm 0.01$
vdMS16	<i>Gaia</i>	$-0.87 \pm 0.07$	$-1.23 \pm 0.05$
Cioni et al. (2016)	VMC	$-0.81 \pm 0.07$	$-1.16 \pm 0.07$
NK13	<i>HST</i>	$-0.77 \pm 0.06$	$-1.12 \pm 0.06$
Vieira et al. (2010)	SPM <sup>a</sup>	$-0.98 \pm 0.30$	$-1.10 \pm 0.29$

Note. — Column 1 indicates the source of the measurement and Column 2 the type of data used to determine the result.

<sup>a</sup> Yale/San Juan Southern Proper Motion program

Table 2.5: Galactocentric Velocities

Galaxy	PM	$v_X$ (km s <sup>-1</sup> )	$v_Y$ (km s <sup>-1</sup> )	$v_Z$ (km s <sup>-1</sup> )	$v_{tot}$ (km s <sup>-1</sup> )	$v_{rad}$ (km s <sup>-1</sup> )	$v_{tan}$ (km s <sup>-1</sup> )
SMC	This Work	18 ± 6	-179 ± 16	174 ± 13	250 ± 20	-10 ± 1	250 ± 20
LMC	Three-epoch NK13	-57 ± 13	-226 ± 15	221 ± 19	321 ± 24	64 ± 7	314 ± 24
SMC-LMC	...	75 ± 17	47 ± 22	-47 ± 23	103 ± 26	92 ± 29	43 ± 11

Note. — The three lines list the SMC velocity, the LMC velocity, and the relative velocity between the SMC and LMC, as measured in this work. Column 1 lists the galaxy name. Column 2 lists the assumed PM value, where the SMC value is this work’s value for the COM PM estimate assuming the H I center and fitting for  $V_{rot}$ , and the LMC value is taken from NK13. To correct for the solar reflex motion, we use the improved McMillan (2011) value of  $V_0 = 239 \pm 5$  km s<sup>-1</sup> and the improved Schönrich et al. (2010) solar peculiar velocity. Columns 3-5 list the Galactocentric velocity coordinates ( $v_X, v_Y, v_Z$ ). Columns 6-8 list the total length of the velocity vector, the radial component, and the transverse component, respectively. Uncertainties were calculated in a Monte Carlo fashion that propagates all relevant uncertainties in the position and velocity of both the Clouds and the Sun. Distance uncertainties are based on  $\Delta m - M = 0.1$ . Velocity uncertainties in the Galactocentric frame are highly correlated, because uncertainties in the LOS direction than in the transverse direction.

## Chapter 3

# The Proper Motion Field Along the Magellanic Bridge: a New Probe of the LMC-SMC Interaction

The following text originally appeared in *The Astrophysical Journal*, Volume 874, Issue 1, and has been lightly edited for this format.

### Summary

We present the first detailed kinematic analysis of the proper motions (PMs) of stars in the Magellanic Bridge, from both the *Gaia* Data Release 2 catalog and from *Hubble Space Telescope* Advanced Camera for Surveys data. For the *Gaia* data, we identify and select two populations of stars in the Bridge region, young main sequence (MS) and red giant stars. The spatial locations of the stars are compared against the known H I gas structure, finding a correlation between the MS stars and the H I gas. In the *HST* fields our signal comes mainly from an older MS and turn-off population, and the proper motion baselines range between  $\sim 4$  and 13 years. The PMs of these different populations are found to be consistent with each other, as well as across the

two telescopes. When the absolute motion of the Small Magellanic Cloud is subtracted out, the residual Bridge motions display a general pattern of pointing away from the Small Magellanic Cloud towards the Large Magellanic Cloud. We compare in detail the kinematics of the stellar samples against numerical simulations of the interactions between the Small and Large Magellanic Clouds, and find general agreement between the kinematics of the observed populations and a simulation in which the Clouds have undergone a recent direct collision.

### 3.1 Introduction

Stretched between the Small and Large Magellanic Clouds (SMC, LMC respectively) lies the Magellanic Bridge, originally identified as an overdensity of H I gas by Hindman et al. (1963). Given the proximity of the two dwarfs, tidal interactions between them were a clear potential explanation, and in time, models of the Magellanic system demonstrated this generally accepted paradigm (e.g., Besla et al. 2012; Diaz & Bekki 2012). Measurements of the relative motions of the SMC and LMC suggest that their most recent interaction likely occurred  $\sim 150$  Myr ago, with an impact parameter of  $< 10$  kpc (Zivick et al. 2018). This implies that the Magellanic Bridge was formed via both hydrodynamic and tidal interactions (Besla et al. 2012).

One additional prediction of the models is the presence of both in situ star formation as well as older, tidally stripped stars. Even before the formal predictions, a population of young stars associated with the Bridge was observed by Irwin et al. (1985), with a follow-up study by Demers & Battinelli (1998), that would be consistent with in situ star formation. Harris (2007) further examined this young population, hoping to use the star formation history to constrain the interactions between the Clouds. The existence of young stellar objects in the region (e.g., Sewilo et al. 2013) and the

strong correlation between young stars and the H I overdensities (e.g., Skowron et al. 2014) helped confirm the in situ formation scenario.

Only recently has there been evidence for the presence of older SMC stars in the Bridge. Using a combination of the WISE and 2MASS surveys, Bagheri et al. (2013) identified red giant branch (RGB) stars scattered around the Bridge region (later confirmed by Noël et al. (2013)). Spectroscopic follow up of targets in the region by Carrera et al. (2017) found the stars to be older than 1 Gyr and with metallicities consistent with having formed in the outer regions of the SMC. The stripping of the SMC was also observed by Belokurov et al. (2017) in *Gaia* DR1 data where they found two spatially distinct structures, separated by multiple degrees, made up of young main sequence stars and RR Lyrae stars.

These structures and their kinematic properties play an important role in understanding the interaction history between the Clouds. Different factors governing this interaction history have been explored in the literature, including varying the masses of the dwarfs, the impact parameters of the interaction, duration of the interaction time, and other factors (e.g., Besla et al. 2012; Diaz & Bekki 2012), each one providing a set of predictions. Understanding the 3D structure of the Bridge can help to constrain these formation scenarios (e.g., Belokurov et al. 2017), and detailed kinematic information will aid in further improving those constraints. Recent efforts have found a trend of stars moving from the SMC to the LMC in the plane of the sky (e.g., Schmidt et al. 2018) and outward motions on the eastern edge of the SMC distinct from the dwarf's motion (Oey et al. 2018), supporting the idea that material has been stripped from the SMC, but no detailed kinematic analysis of the Bridge has yet been published.

In this paper, we present the first detailed analysis of the proper-motion (PM) field

of stars in the Magellanic Bridge, and directly compare these PMs to predictions from simulations of the interaction history of the Clouds. We use the recently published *Gaia* Data Release 2 catalog (Gaia Collaboration et al. 2016c; Gaia Collaboration et al. 2018b) in combination with *HST* data to examine the kinematic structure in the Bridge. We examine both young and old stellar populations in the Bridge region. We treat each population separately and consider for the young stars the H I gas structure for potential correlations. For the comparisons with theory, we use the models presented in Besla et al. (2012).

The paper is organized as follows. In Section 3.2 we discuss the selection criteria applied to the *Gaia* data as well as the analysis and calculation of the PMs from the *HST* data. This data is transformed into a model-ready comparison frame, described at the beginning of Section 3.3. From there we examine the spatial and kinematic differences between the young and old populations and the young stellar population’s spatial correlation with the H I gas. We close Section 3.3 by making direct comparisons with simulations of the past interactions of the Clouds. Finally, in Section 3.4 we summarize our findings and their implications for our understanding of the Magellanic system.

## 3.2 Data Selection

### 3.2.1 *Gaia* DR2 Data

From the *Gaia* database, we select all stars within the vicinity of the Clouds (the exact area is shown in Figure 3.1) using `pygacs`<sup>1</sup>. We begin with a simple parallax cut of  $\omega < 0.2$  mas in order to remove foreground MW stars. Next we apply the

---

<sup>1</sup><https://github.com/Johannes-Sahlmann/pygacs>

following cut to the renormalized unit weight error (RUWE) as described in the *Gaia* technical note GAIA-C3-TN-LU-LL-124-01:

$$\frac{\sqrt{\chi^2/(N-5)}}{u_0(G, C)} < 1.40, \quad (3.1)$$

which uses the following *Gaia* properties:

$$\begin{aligned} N &\equiv \text{astrometric\_n\_good\_obs\_al}, \\ \chi^2 &\equiv \text{astrometric\_chi2\_al}, \\ u_0 &\equiv \text{Normalization factor } (G, C), \\ G &\equiv \text{phot\_g\_mean\_mag}, \\ C &\equiv \text{bp\_rp}. \end{aligned} \quad (3.2)$$

We additionally apply a cut for the color excess of the stars, as described in Gaia Collaboration et al. (2018a) by Equation C.2. As we are concerned with the better astrometrically behaved stars, primarily the bright stars, and to provide another check to avoid MW contamination, we select stars brighter than  $G < 17$ , leading to the final source densities in Figure 3.1.

From this initial catalog we select a smaller area for closer examination, stretching from the eastern edge of the SMC to the western edge of the LMC. These boundaries are marked in red in Figure 3.1. From this region, we apply two more criteria in the location of the stars in the color-magnitude diagram (CMD) and their PMs. For the CMD, first we de-redden our sample of *Gaia* stars, using Gaia Collaboration et al. (2018b) and Schlegel et al. (1998). Using the de-reddened CMD, we select main sequence (MS) and red giant (RG) stars as indicated in Figure 3.2. We provide for reference three PARSEC isochrones (Marigo et al. 2017), the two in blue at 10

and 30 Myr and the one in red at 800 Myr. We note that we are not attempting a rigorous fit to the stellar populations, but instead we use these to highlight the likely populations belonging to the Clouds. The two young isochrones do appear to trace distinct MS populations, especially above  $G < 15$ . An examination of the spatial and kinematic properties of the two populations revealed no apparent difference, so for the comparison to both the older population and numerical modeling, all MS stars will be categorized together. For the PM selection (see Figure 3.3), we select all stars in and around the two dense regions, with each region belonging to one of the Clouds, with the systemic motions marked in light green. With this cut in PM, we allow for stars originating from the LMC to be included in the sample. Given the large overdensity in Figure 3.3, it is likely that many of the stars, especially those spatially overlapping with the LMC, are of LMC-origins. However, due to the uncertainty in assigning a definite membership to any given star, we keep this broader PM selection to provide as much relevant information regarding the Bridge as possible. Our final sample only includes stars that pass both of these cuts.

A subsample of roughly 3,000 MS stars and 20,000 RG stars pass our astrometric and CMD-based cuts. Examining the physical location of the stars in this sample, we see that the selected MS stars trace the expected Bridge structure while the RG stars primarily trace the broader SMC and LMC structure, although some RG stars are scattered throughout the Bridge area (Figure 3.4). For easier viewing, the RG population has been randomly subsampled to the same number as MS stars. Our selected area does include part of the region identified as possessing LMC substructure in the RG population in *Gaia* DR2 data by Belokurov & Erkal (2019). This substructure, roughly located in the bottom left of our Figure 3.4, can be slightly seen, but we ascribe most of the difference to our brighter magnitude cut of  $G < 17$  removing

much of the signal in addition to the subsampling done for display purposes. From here, we begin to examine the kinematic properties of the stars as they relate to the larger Magellanic system.

### 3.2.2 *HST* Data

In addition to the *Gaia* PMs, we measured PMs of stars in the Magellanic Bridge using *HST* data. We searched the *HST* archive for existing deep imaging located along the Magellanic Bridge and found three fields. The characteristics of these fields are summarized in Table TBD The first-epoch data for the three fields were obtained for *HST* programs to study the cosmic shear or Lyman-break galaxies at high redshift. The second-epoch data were obtained through our *HST* program GO-13834 (PI: van der Marel) to measure PMs. We used the same observational setup (i.e. telescope pointing, orientation, detector, and filters) as the first-epoch observations. For the astrometric analysis we used the F775W filter data, and to construct CMDs of our target fields that may help in identifying stars along the Magellanic bridge against Galactic foreground contamination, we obtained F606W exposures during our second-epoch observations.

We measured the PMs of stars in our target fields using the same technique as used in Sohn et al. (2015, 2016). Readers interested in the details of the PM mea-

Table 3.1: *HST* Target Fields and Observations

	R.A.	Decl.	Epoch 1			Epoch 2 (Prog. ID 13834)	
Target Fields	(J2000)	(J2000)	Prog. ID	Epoch	Exp. Time (s) <sup>a</sup>	Epoch	Exp. Time (s) <sup>a</sup>
<i>HST</i> -BG1	02:04:11.2	−76:16:11.5	12286	2011.49	2132	2015.43	9126
<i>HST</i> -BG2	02:30:41.6	−73:53:43.3	9488	2003.20	2400	2015.21	8757
<i>HST</i> -BG3	04:21:05.0	−74:02:26.9	9488	2002.72	1800	2015.68	9246

<sup>a</sup>Total exposure time of the F775W observations used for astrometric analysis.

surement process are referred to those papers. In short, we created high-resolution stacked images by combining our second-epoch data, identified stars and background galaxies from these stacks, constructed templates for stars and galaxies, determined template-based positions of stars and galaxies on images in each epoch, and measured displacements in positions of stars with respect to the background galaxies between the two epochs. We also measured photometry for each star in our target fields in the F606W and F775W bands. To do this, we used *AstroDrizzle* (Gonzaga & et al. 2012) to combine images for each field per filter and measured the flux within aperture radius of 0.1 mas (i.e., 4 ACS/WFC pixels) from the center of each stars. Aperture corrections were carried out to infinity following the method by Sirianni et al. (2005). The photometry was then calibrated to the ACS/WFC VEGAMAG system using the time-dependent zero points provided by the STScI webpage.

Figure 3.5 illustrates the selection of Magellanic Bridge stars in our *HST* fields. The top panels show the CMDs, while the lower panels show the PM diagrams of all stars detected in the images. Selection of Magellanic Bridge stars in the target fields is straightforward since the PM diagrams exhibit conspicuous clumps as expected for groups of stars co-moving in the same direction. We first identified these clumps and selected candidate members of the Magellanic Bridge based on their distance from the average  $(\mu_W, \mu_N)$  of the clumps. For this we define a local reference frame for  $\mu_W$  and  $\mu_N$  with  $\mu_W \equiv -(d\alpha/dt) \cos(\delta)$  and  $\mu_N \equiv d\delta/dt$ . We then inspected the CMDs to verify that the majority of stars in the clump are consistent with an LMC- or SMC-like stellar population. The overlaid isochrones in the top panels of Figure 3.5 were adopted from the Dartmouth Stellar Evolution Database (DSED, Dotter et al. 2008), and represent such a population. Our goal here is not to carry out a detailed stellar population study for each field but to use the CMDs to select

highly probable members of the Magellanic Bridge. With this in mind, we allowed a fairly wide range in color relative to the isochrones when selecting members, and only filtered out stars noticeably segregated in the CMD. Most of the non-members are far redder than the selected Magellanic Bridge candidates, and are most likely giant stars in the MW halo that happen to lie in the same region occupied by the Bridge stars in the PM diagram. We would add that all of the isochrone ages displayed represent populations formed before the most recent interaction between the SMC and LMC. The average PMs of selected stars in each field were then calculated by taking the error-weighted mean, and the uncertainties of the averages were computed by propagating the individual PM uncertainties. We have also added the uncertainties originating from setting up the stationary reference frame using galaxy positions in quadrature, which typically dominates the final PM uncertainties. Results are shown in Table 3.2. We note that our results are insensitive to the CMD selection of Bridge stars. For example, we repeated our selection using a much more conservative criteria (i.e., only allowing stars consistent with the isochrones in Figure 3.5 within their color errors), and the resulting average PMs are all consistent with those in Table 3.2 within their  $1\sigma$  uncertainty. We have also verified that there are no correlations between the locations in the CMDs and the PM diagrams for the selected Bridge stars.

In addition to the three fields measured using the background galaxies, five additional fields were observed with the intent to use background quasars to measure the PMs (e.g., as in Kallivayalil et al. 2013). The first epoch was observed in late 2014 as part of the original program and a new second epoch was observed in late 2017 as part of our *HST* program GO-14775 (PI: van der Marel). However, the sample of spectroscopically-confirmed QSOs available at the time were very bright compared to the average Bridge star, and even though we designed our *HST* observations with

short and long exposures in order to try to mitigate this, due to the tension between avoiding saturating the bright quasar while still observing a sufficiently large number of stars in the fields, we were unable to successfully measure high-quality PMs for these five fields. The resultant errors were roughly on the order of  $1 \text{ mas yr}^{-1}$ , and are not competitive with the dataset compiled above.

### 3.3 Data Analysis & Model Comparisons

#### 3.3.1 Data Analysis

For our analysis, we need the motions of the stars relative to the Clouds, not just their absolute motions. However, as our sample stretches across tens of degrees on the night sky, simply subtracting the systemic motion of the SMC (chosen as the zero-point for the system) is incorrect as the projection of the systemic motion onto the plane of the sky will shift dramatically. To address this we correct for the viewing perspective at each star, as outlined in van der Marel et al. (2002), in addition to subtracting the systemic SMC motion ( $\mu_W = -0.82 \text{ mas yr}^{-1}$  and  $\mu_N = -1.21 \text{ mas yr}^{-1}$ , Zivick et al. 2018; consistent with the PM found by Gaia Collaboration et al. 2018c). With all of the individual motions shifted into this standard frame, we then

Table 3.2: Proper Motion Average and Dispersion for the Magellanic Bridge Stars in the *HST* Fields

Field	$\mu_W$ mas yr $^{-1}$	$\mu_N$ mas yr $^{-1}$	$N_{\star}^a$
<i>HST</i> -BG1	$-1.638 \pm 0.052$	$-1.421 \pm 0.052$	259
<i>HST</i> -BG2	$-1.503 \pm 0.020$	$-0.799 \pm 0.020$	177
<i>HST</i> -BG3	$-1.960 \pm 0.013$	$-0.326 \pm 0.013$	912

---

Note. — a. Number of Magellanic Bridge stars included in the PM calculations.

transform the positions and PM vectors into a Cartesian frame, as defined in Gaia Collaboration et al. (2018c), to allow for consistent calculations of motion along the Bridge. We define the  $x$ -axis as the line connecting the kinematic centers of the SMC  $((\alpha, \delta) \text{ (J2000)} = (16.25^\circ, -72.42^\circ))$  and LMC  $(78.76^\circ, -69.19^\circ)$  with positive in the direction of the SMC. The arrangement of our sources in this reference frame can be seen in Figure 3.4. We use this reference frame in all later analyses and comparisons to models and refer to proper motions calculated in this way as "relative proper motions" in the figures. This same process of viewing-perspective correction and transformation is applied to the PMs of the three *HST* fields as well in addition to the systemic motion of the LMC at its kinematic center.

In Figure 3.6 we plot the resulting median residual PM vectors relative to the SMC center of mass (COM) PM, separated in  $0.5^\circ \times 0.5^\circ$  degree bins across our selected region, with the two stellar populations indicated by our color convention. To help ensure that the displayed vectors are representative of the behavior at that location, only bins where there are five or more stars present are displayed. We see that the different stellar populations do not display significant differences in the vectors across the Bridge. However, we do see that when the absolute motion of the Small Magellanic Cloud is subtracted out, the residual Bridge motions display a general pattern of pointing away from the SMC towards the LMC. We display the measured motions for the *HST* fields as well, which show a general agreement in the direction of motion, albeit different in the magnitude of the motion.

For the analysis, we keep all units in observed quantities, as converting to physical units, such as  $\text{km s}^{-1}$ , would require assumptions about the 3D structure of the Bridge. We found from our analysis that the *Gaia* parallaxes, while efficient at removing foreground stars, are not good enough to afford improved insights into the distances

along the Bridge (median parallax errors of  $\sim 0.05$  mas for stars brighter than  $G < 17$ , where expected parallax at 50 kpc is  $\sim 0.02$  mas). The resulting relative motions for the different stellar populations are shown in Figures 3.7 and 3.8, and are discussed below.

Given the large number of stars in our samples, for display-purposes we group the data every 0.2 degrees. Within each group, we calculate the error-weighted average PM and the standard error of the weighted average. This error calculation only captures the random error of the measurements, not the spatially correlated systematic errors in the *Gaia* DR2 catalog, which Lindegren et al. (2018) finds to be between  $\sim 0.07$  mas yr<sup>-1</sup> for sources averaged over less than a degree and  $\sim 0.03$  mas yr<sup>-1</sup> for sources averaged over  $\sim 10$  degrees or more. These average PMs are marked in Figures 3.7 and 3.8 by the color points with the raw data plotted as the gray points in the background. We note that for each bin the errors are displayed but that for many of the bins the resulting standard error is smaller than the points. The ‘raw’ data display roughly similar spreads in PM. Potential differences could readily be attributed to the difference in the spatial distribution of the two populations, with the MS stars relatively tightly clustered together while the RG stars are spread out over nearly ten degrees.

We additionally display a range of possible LMC-bound motions, drawn from the rotating disk model of the LMC from van der Marel & Kallivayalil (2014), as a light green region. The HST motions are shown as red squares in each Figure with their calculated errors, which illustrate the motion of older MS and turn-off stars. Reassuringly, we see that for both the MS stars and RG stars the *HST* motions agree quite well with the *Gaia* data. We note that the errors displayed are scaled the same for both *HST* and *Gaia* so the comparable precision of the *HST* fields is real, despite

the far fewer number of stars that have been averaged in each field. This illustrates that HST remains unique for small-field astrometric studies at faint magnitudes and large distances.

### 3.3.2 H I and Stellar Comparisons

As discussed briefly in Section 3.2.1, while two distinct MS branches are discernible in Figure 3.2, the kinematic and spatial properties of the two branches are not significantly different. As such we choose to consider all MS stars together. For these young stars, we test for potential correlations with the H I gas distribution in the Bridge. For this comparison, we use the H I data from Putman et al. (2003), and in Figure 3.9 plot the gas intensity in addition to the locations of the MS stars. The correlation between the H I and the stars is immediately clear from the Figure, a trend that has been demonstrated in previous studies (Skowron et al. 2014, e.g.,). We can see a large overlap of young stars with the dense arm of H I gas stretching out towards the LMC. We also note that slightly further out, at  $\sim 8$  degrees, we observe a slight overdensity of young stars that falls between two peaks in the H I gas. Given the tight spatial correlation between the gas and the stars, we can infer that the behavior of these stars should indeed be similarly correlated with the kinematics of the underlying gas.

Given the preferred age of tens of Myr for the MS stars and this tight correlation, we can interpret the two different populations as pre- and post-interaction with the LMC, as the RG stars are on the order of 1 Gyr old and the collision timeframe has been constrained to be roughly 100 Myr ago (Zivick et al. 2018). With this framework in mind, we look at the differences in behavior between the MS and RG stars, focusing on the weighted average PMs of each to compare the populations (shown against each other in Figure 3.10).

In the  $x$ -direction, there appears to be a slight offset between the old and young populations with the MS stars having systematically larger negative PMs than the RG stars. Using the difference of the averages divided by the errors summed in quadrature as a statistic of significance, we find almost every bin before 7 degrees to be significant at the  $3\sigma$  level or greater. Even when accounting for the potential systematic error introduced by the spatial correlations (assumed to be  $\sim 0.04 \text{ mas yr}^{-1}$  given the intermediate spatial scales listed earlier), many of the individual bins still remain significant at the  $3\sigma$  level. Past 7 degrees the stellar sparsity makes statistical comparisons difficult, so we refrain from over-analyzing the trends. Interestingly in the  $y$ -direction we observe no such significance. Indeed across most of the Bridge, even in the sparse regions, the MS and RG populations appear to generally agree with each other. However, this is not an entirely unexpected result given the comparisons of the two Models, discussed further below. We do note the apparent structure in  $\mu_x$  for the RG stars with a cluster of points above  $0.0 \text{ mas yr}^{-1}$ , stretching from  $\approx 6$  degrees to 10 degrees. However, further examination of these stars does not reveal any significant spatial correlations or correlations in  $\mu_y$ . One potential explanation would be that this is a detection of the RG tidal features of the SMC and LMC found in Belokurov et al. (2017).

We also compare the location of the LMC-disk PMs to the data. In both the  $x$ - and  $y$ -directions we see the RG data matching well with the predicted PMs of the disk, though we note that this only holds true for near the LMC. Within  $\sim 10$  degrees of the SMC, one observes a clear shift in the behavior of the stars. For the MS stars, the agreement is not as clear. The PMs in the  $x$ -direction appear to have a rough agreement, but there is a noticeable offset in the  $y$ -direction. We posit that the MS stars measured here originated from H I gas not initially belonging to the LMC

as an explanation for this disparity, but given the sparsity of the data, refrain from attempting further analysis.

### 3.3.3 Model Comparisons

To understand the implications for the Magellanic system, we compare our data against simulations of the interactions between the Clouds from Besla et al. (2012). Two models are explored, one in which the SMC and LMC interact tidally but remain relatively well-separated from each other ( $\sim 20$  kpc separation), referred to as Model 1, and one in which the SMC and LMC collide ( $\sim 2$  kpc separation), referred to as Model 2. In Model 1, the Bridge forms out of gas and stars tidally stripped from the SMC by the LMC. However, in Model 2 the SMC gas undergoes ram pressure stripping after encountering the LMC gas as it passes through the LMC's disk. This hydrodynamic interaction enhances the density of the stripped gas and forces the corresponding stars that form in-situ to trace the SMC's motion back towards the LMC. From the presence of in situ star formation known already in the Bridge (e.g., Harris 2007), we have reason to prefer the latter scenario, but our data allow us to further constrain the interaction history. For more details on the computational aspects of the simulations, please refer to Besla et al. (2012).

The results from the simulations, similarly transformed and binned as our data, are displayed against the average PMs of the data in Figure 3.10 (Model 1 in purple, Model 2 in lime-green). We convert the physical units of the simulation (kpc, km  $s^{-1}$ ) to observed quantities (degrees, mas  $yr^{-1}$ ) to reduce the number of assumptions required for manipulating the data. For this conversion, we adjust the center of mass (COM) position of the modeled SMC to match the observed COM location of the SMC. Note that the Bridge in Model 2 does not extend as far as in Model 1

(the area marked by the dashed black lines in Figure 3.4 denote the area covered by Model 2, whereas Model 1 covers the entire area of the figure), limiting our ability to fully compare to our data. Nonetheless, the models do clearly predict distinct and different PM signals. Additionally, when we test limiting the spatial selection of our data for comparison to Model 2, we do not find any noticeable shifts in the average PMs for either the MS or RG populations. As a result, we choose to present kinematic information for all stars in the Bridge area. The two models diverge in the  $x$ -direction providing a clear test for comparison. The predicted motions in the  $y$ -direction are not as starkly different near the beginning of the Bridge, but we note that the continuation of Model 1 beyond  $\sim 6$  degrees from the SMC does provide some additional discriminatory power.

Before comparing the observed data to the simulated data, we note that the exact magnitudes of the motions are not a point of emphasis. Given the number of parameters involved in setting up the simulation, and with total LMC & SMC masses being crucial unknowns in this, we do not expect that our data will perfectly replicate the predictions of the models. Instead we focus on comparisons of the trends in the data and the models to help provide a physical intuition for interpreting the data. That being said, perhaps surprisingly, we do find that the magnitudes of the PMs of the predicted and observed data along the Bridge do live in the same ballpark.

In comparing the data to Model 1 in Figure 3.10, we see a distinct disagreement between data and model in the  $x$ -direction. From the closest point in to the SMC, the values begin to diverge. In the  $y$ -direction, the difference is not as dramatic close to the SMC, but as the simulation data approaches the LMC, the predicted motion continues to increase in a positive direction while our observed data trends in the opposite direction, ending with a difference of almost  $1 \text{ mas yr}^{-1}$ . For Model 2, the

predicted motions along the  $x$ -direction agree well with the observed data, although we are limited in the extent of our comparison beyond  $\sim 6^\circ$  from the SMC center. However, this limitation itself provides a potential test as the shorter Bridge forms as a result of the direct collision and the resulting gas interactions between the SMC and LMC. Interestingly, we observe a distinct decline in the number of MS stars beginning around a similar distance into the Bridge as in Model 2. In the  $y$ -direction, we see a similar difference in the magnitudes of the motions as with Model 1, although not at as significant a level of disagreement, and the trend directions of both models and data roughly agree within  $6^\circ$  of the SMC.

In both models, the SMC is initially modeled as a rotating disk in a prograde orbit about the LMC, which enables the formation of the Magellanic Stream via tidal stripping. In Model 1, the lack of a direct collision means that the SMC disk retains ordered rotation. As a result, the tidally stripped material that forms the bridge contains residual signatures of the disk rotation, resulting in the positive motion along both the  $x$  and  $y$  direction in Figure 9. In contrast, in Model 2, the SMC disk is destroyed in the collision (Besla 2011; Besla et al. in prep). As such, both stripped stars and gas track the motion of the SMC back towards the LMC, without any rotation. Given the known structure of the H I gas, and now the observed motions of stars moving away from the SMC, we find strong evidence for the scenario of a recent direct collision.

### 3.4 Discussion & Conclusions

We present the first detailed analysis of the PM kinematics of the stellar component of the Magellanic Bridge using a combination of *Gaia* and *HST* data. In the *Gaia* data we examine two different stellar populations, the MS and RG stars. In both cases,

we use *Gaia* parallaxes, photometry, and kinematics to help discriminate between foreground stars and SMC/LMC stars. The *Gaia*-selected data span the entire length of the Bridge between the two Clouds. We point to the observable split between two main sequence populations to illustrate our ability to select a "clean" sample of Magellanic stars.

Milky Way contamination is less of a concern with the *HST* data. There we measure PMs in three Bridge fields, two relatively close to the SMC and one relatively close to the LMC. The PMs are measured with respect to background galaxies and over baselines of  $\sim 4 - 13$  years. We pick up a much fainter, and relatively old population of MS and turn-off stars with *HST* compared to *Gaia* as would be expected. One of the *HST* field locations overlaps with the *Gaia* data, while the other two probe independent directions along the Bridge. The overlapping field gives us an opportunity for a direct comparison between *Gaia* PMs and *HST*-measured PMs, albeit targeting different stellar populations, and these two independently-measured PM sets are found to be consistent with each other.

The different stellar populations probed by our datasets, in turn, give us an opportunity to investigate population-based structure and kinematics. The young MS stars display a strong spatial correlation with the underlying H I gas, unlike the RG stars that trace a broader dispersed structure around both the SMC and LMC. However, for the kinematics, both the RG and the MS stars exhibit similar behavior in increasing magnitude of their motion towards the LMC. The other component of their motion in the plane of the sky remains roughly consistent with the systemic motion of the SMC, only decreasing near the LMC.

We compare the PM kinematics along the Bridge to predictions from two numerical simulations of the interaction-history of the Clouds from Besla et al. (2012). The

two different numerical simulations examined both consider the Bridge to be caused by tidal disturbance of the SMC by the LMC on a recent ( $\sim 100$  Myr) past encounter, but in Model 1, the Clouds remain relatively well-separated, with perhaps a grazing past encounter with an impact parameter of  $\sim 20$  kpc, while in Model 2, the SMC goes directly through the LMC, with an impact parameter for the encounter of  $\sim 2$  kpc (for reference, the LMC's disk radius is 18.5 kpc Mackey et al. (2016)). As such, Model 2 also allows for a hydrodynamic interaction between the SMC and LMC gas disks and ultimately destroys any signature of rotation in the SMC main body (Besla 2011). These two models predict different kinematic signatures in the  $x$ -direction, defined as the axis that lies along the line that connects the centers of the LMC and SMC (see Figure 3.4), and when compared against the observational data, we find strong agreement with the direct collision model (Model 2). Combined with previous studies on the interaction parameters of the Clouds (e.g., Besla et al. 2012; Zivick et al. 2018), the growing body of evidence heavily favors such a direct collision (e.g., Oey et al. 2018), with an impact parameter of a few kpc.

Future work in this area will consist of continuing to draw in other types of data sets (e.g., star formation histories, metallicities) to build a more holistic view of the history of the Clouds. This includes deeper examinations of the gas content of the Clouds where recent work has helped constrain the histories both using H I data (McClure-Griffiths et al. 2018) and molecular gas (Fukui et al. 2018). Future data releases from *Gaia* will also continue to improve in data quality, but specifically, improvements in the parallaxes will allow us to include distances along the Bridge both as a constraint in the interaction history and more broadly to better separate out Magellanic debris (Bridge(s), Stream(s)) from Milky Way pollutants. Better distances for the Magellanic RGs will also aid a more rigorous investigation of population-based

kinematic differences in the Bridge.

Additionally, analysis of the PM kinematics of the stellar populations of the SMC main body from *Gaia* along the lines of the analysis present here, will allow us to better constrain its geometry. At present, there is little evidence for internal rotation in the SMC, and strong evidence that the main body is being tidally disrupted, based largely on *HST* data (Zivick et al. 2018). The addition of radial velocities will also add one more piece to the puzzle of the Magellanic Clouds, which are looking more and more like a local analog of the Antennae galaxies. As shown by Figure 3.9, perhaps the most striking aspect of the data set presented here is the strong spatial correlation between H I gas in the Bridge and very young stars. Clearly the Clouds are an ideal laboratory to study star formation in a low metallicity regime.

On the numerical side, upcoming work will explore the impact of the LMC–SMC collision on the structure of the SMC main body (Besla et al. in prep). Future studies including a more realistic treatment of star formation are needed to better understand the consequences of the recent violent interaction history to the star formation histories of the Clouds.

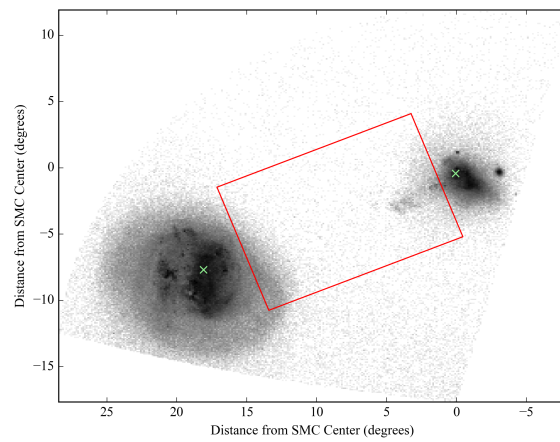


Fig. 3.1.— *Gaia* source density count around the Magellanic System with cuts made as described in 3.2.1 for astrometric quality. The green crosses mark the locations of the assumed centers of the LMC and SMC, and the red box indicates the area examined further for Bridge dynamics. (0,0) is defined as the kinematic center of the SMC.

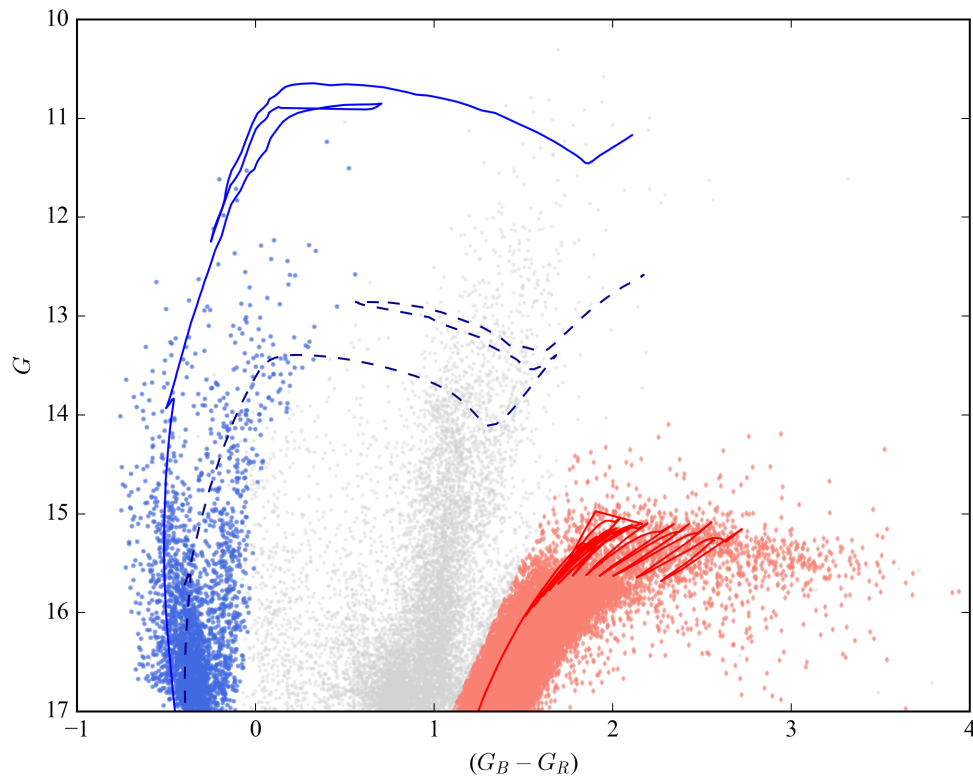


Fig. 3.2.— Color-Magnitude Diagram of the selected Bridge region. All stars in the region are marked in gray. The blue colored points indicate the stars selected by our mask as main sequence stars, and the orange-red colored points indicate the red giant mask. From left to right the PARSEC isochrones are 10 Myr (solid blue line), 30 Myr (dashed dark blue line), and 800 Myr (solid red line), all more metal-rich than  $[M/H] > -0.65$ .

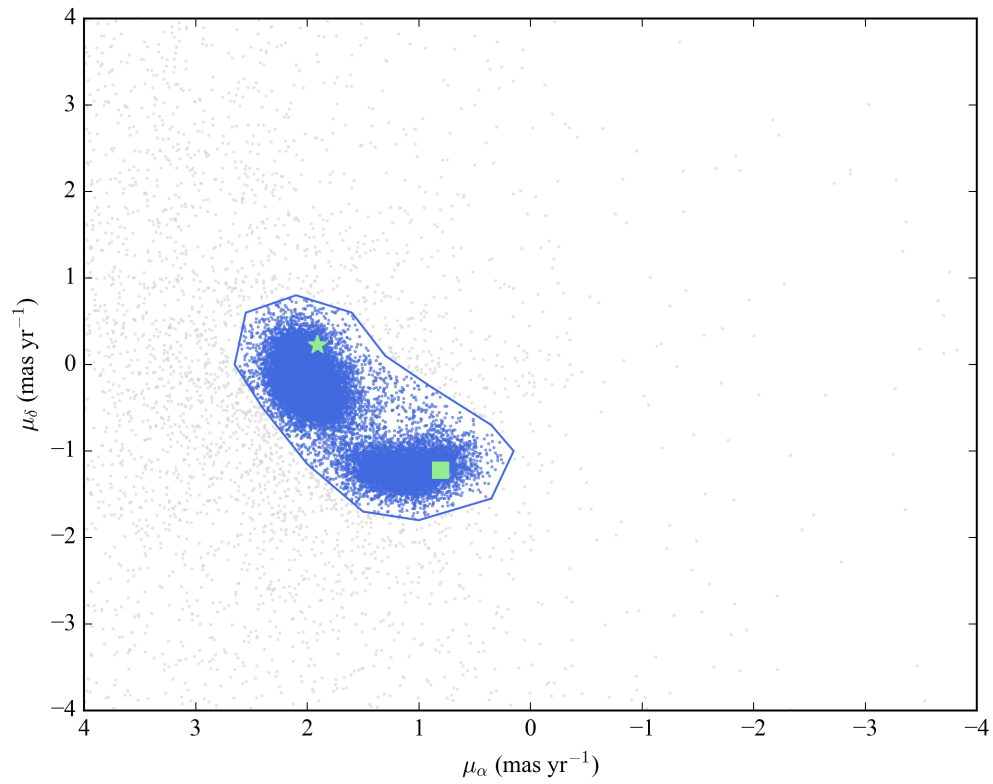


Fig. 3.3.— Proper motion diagram for the selected Bridge stars. All stars present in the region are marked in gray. The blue lines indicate the PM region identified as belonging to the Magellanic system. The light green square indicates the PM of the SMC and the light green star indicates the PM of the LMC.

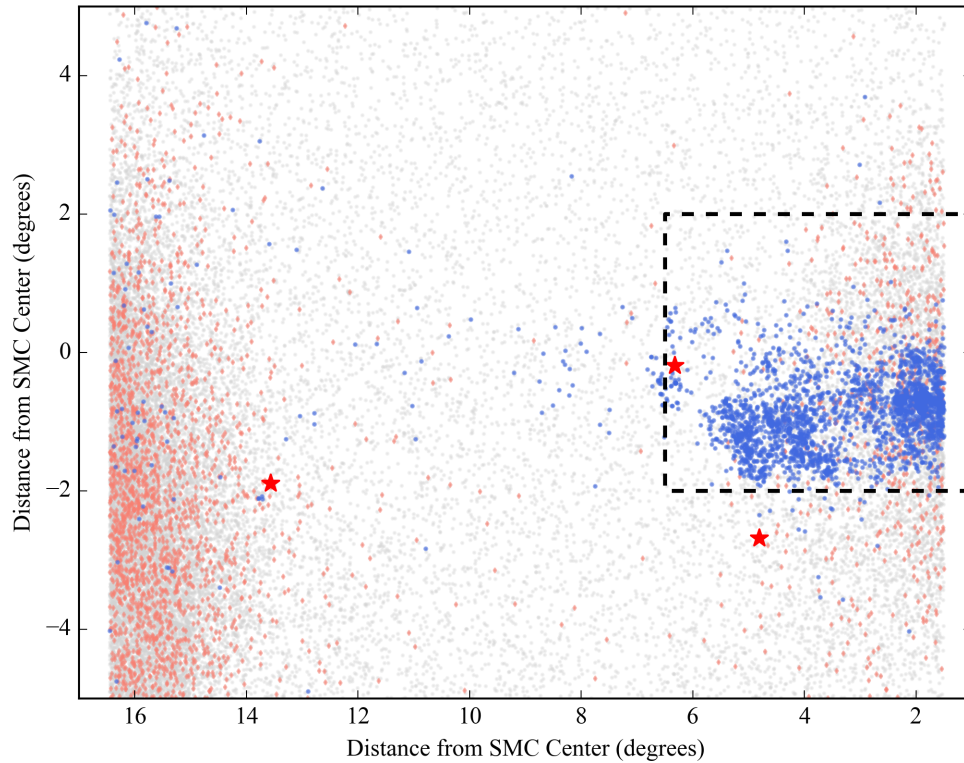


Fig. 3.4.— Bridge region with the main sequence (MS) population marked in blue and the red giant population (RG) marked in orange-red. The frame has been rotated such that the  $x$ -axis now lies along the line between the assumed centers for the LMC and SMC, where  $(0,0)$  is the center of the SMC. The area comparable to Model 2 (discussed in 3.3.3) has been outlined in black for easier comparison, and the locations of the *HST* fields are marked with brown stars. The RG population has been randomly subsampled down to the level of the MS stars to allow for easier comparison of the spatial correlations.

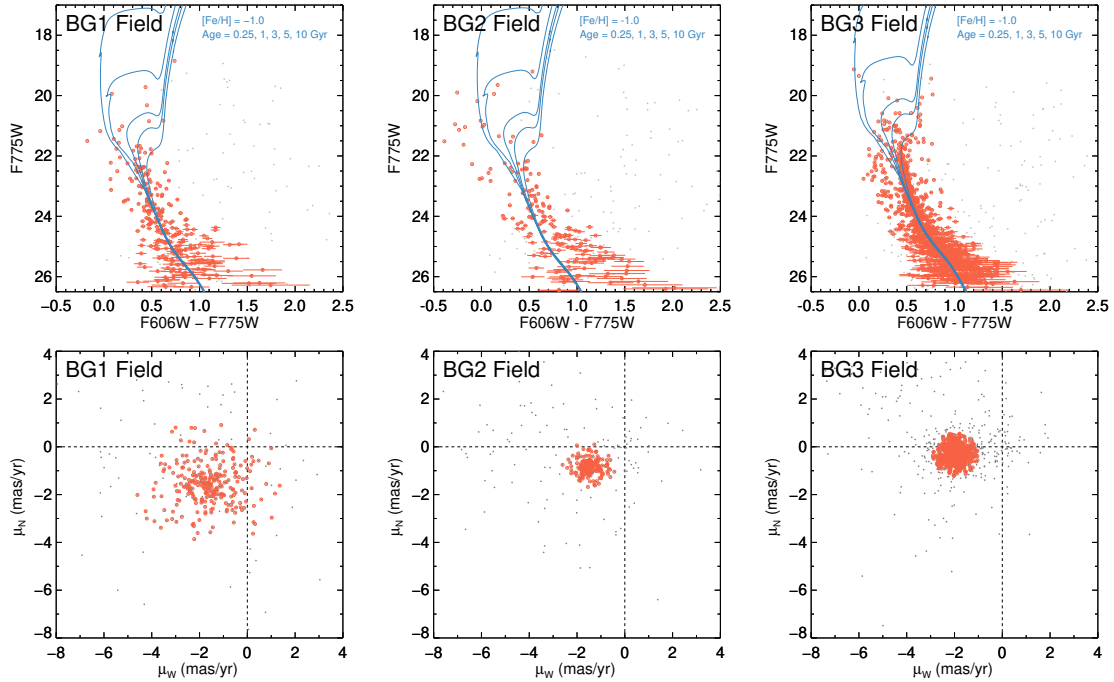


Fig. 3.5.— Color-magnitude (top) and proper motion diagrams (bottom) for the three *HST* fields. Stars selected as belonging to the Magellanic Bridge are plotted in red while non-members are plotted in gray. In the top panels, we overplot isochrones with metallicities  $[\text{Fe}/\text{H}] = -1.0$  and ages 0.25, 1, 3, 5, and 10 Gyr to represent stellar populations expected in these regions. Distances of 62, 62, and 50 kpc were adopted respectively for BG1, BG2, and BG3. We applied reddening to the isochrones based on the  $E(B - V)$  values estimated from interpolating the reddening maps of Schlegel et al. (1998), and the total absorption values were adopted from Table 6 of Schlafly & Finkbeiner (2011).

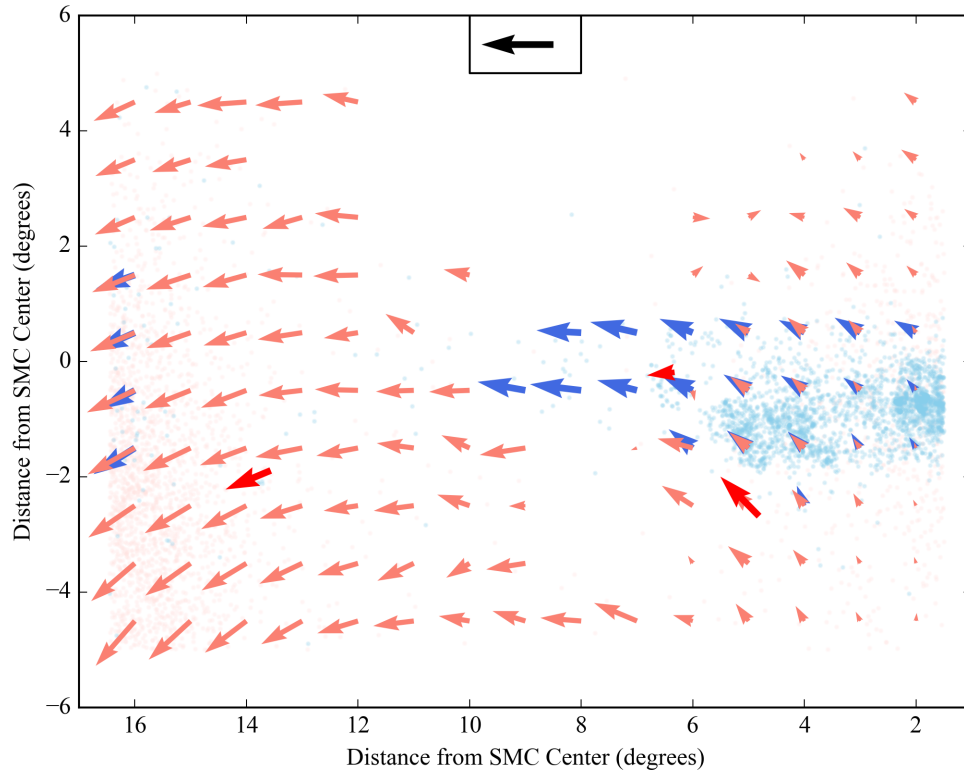


Fig. 3.6.— Vector field of the residual PMs of the stellar populations in the Bridge relative to the SMC COM PM. The RG stars are displayed in orange-red, and the MS stars in blue. The *HST* fields are marked in brown. The locations of each population are displayed in the background for reference. The median vectors are created from  $0.5^\circ \times 0.5^\circ$  bins and are only calculated if five or more stars are present. A reference vector of  $1 \text{ mas yr}^{-1}$  is provided at the top of the figure in black. The largest *Gaia* vector has a length of  $1.01 \text{ mas yr}^{-1}$ .

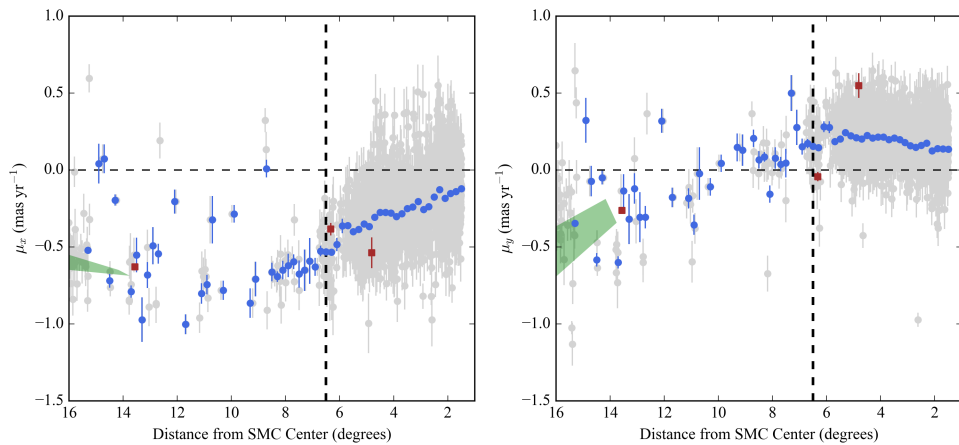


Fig. 3.7.— (Left) Relative proper motions of the stars in the Bridge along the  $x$ -axis as a function of angular distance from the center of the SMC. All MS stars selected as part of the Bridge are displayed in gray. To understand the typical motion as a function of distance across the Bridge, the data are binned every 0.2 degrees, and the resulting error-weighted average PM in each bin is displayed in blue along with the standard error for weighted averages. The systematic errors of the *Gaia* DR2 catalog are not displayed. The motions of the *HST* fields are marked in brown and the LMC-disk PMs by the light green region on the lefthand side of the plot. The vertical dashed line indicates the limit of comparison to Model 2, and the horizontal dashed line at  $0 \text{ mas yr}^{-1}$  is a guide for the eye. (Right) Same as for the left plot but for the motion along the  $y$ -axis.

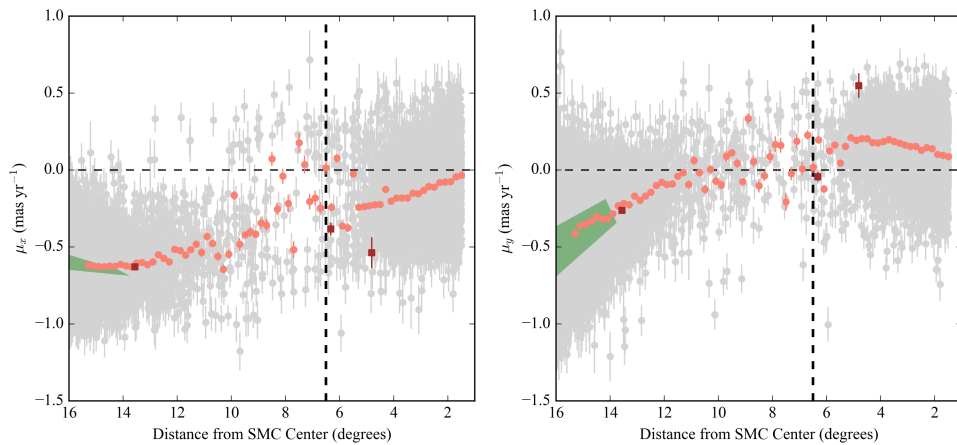


Fig. 3.8.— (Left) Relative proper motions of the older stars in the Bridge along the  $x$ -axis as a function of angular distance from the center of the SMC. All RG stars selected as part of the Bridge are displayed in gray. To understand the typical motion as a function of distance across the Bridge, the data are binned every 0.2 degrees, and the resulting error-weighted average PM in each bin is displayed in orange-red along with the standard error for weighted averages. The systematic errors of the *Gaia* DR2 catalog are not displayed. The motions of the *HST* fields are marked in brown and the LMC-disk PMs by the light green region on the lefthand side of the plot. The vertical dashed line indicates the limit of comparison to the models, and the horizontal dashed line is at  $0 \text{ mas yr}^{-1}$  as a guide for the eye. (Right) Same as for the left plot but for the motion along the  $y$ -axis.

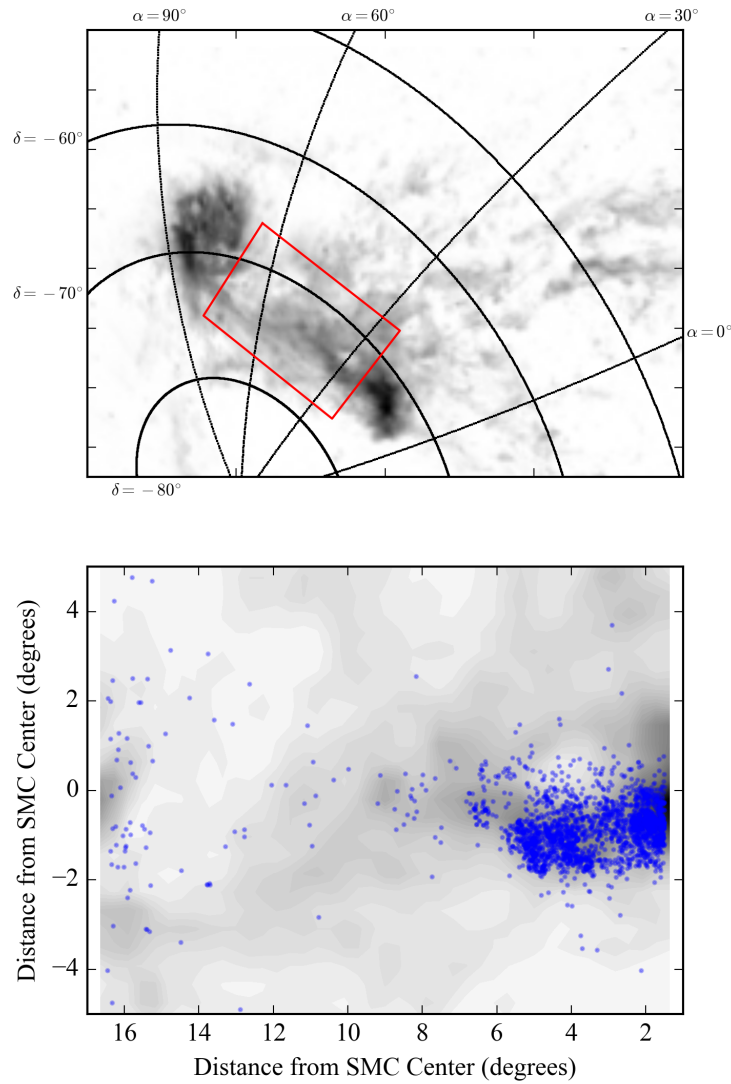


Fig. 3.9.— (Top) H I gas intensity map from Putman et al. (2003) with lines of constant RA and Dec provided for reference. The LMC is the large structure in the middle left of the panel and the SMC is located below and to the right of the LMC with the Bridge stretching between them. (Bottom) The H I map transformed into our working frame with the location of the selected MS stars overlotted in blue.

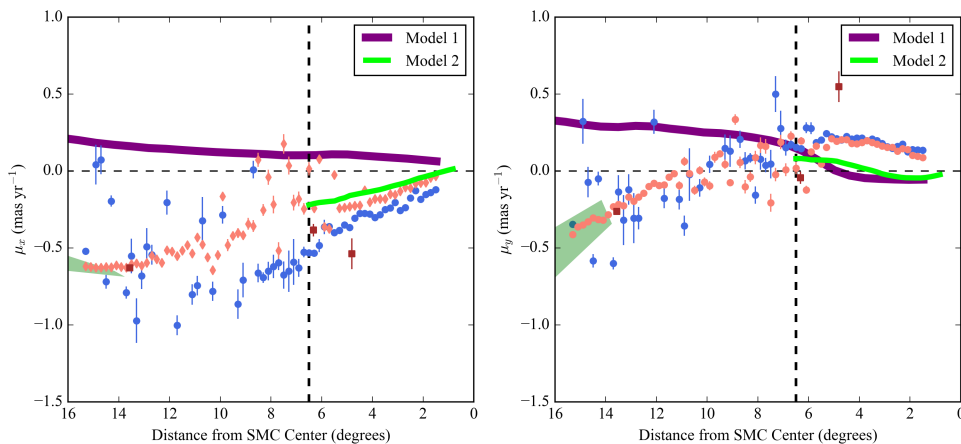


Fig. 3.10.— (Left) Error-weighted average relative PMs along the Bridge in the  $x$ -axis direction, calculated as described in Section 3.3.1 for the RG (orange-red) and MS (blue) stars. The motions of the *HST* fields are marked by the brown squares and the LMC-disk PMs by the light green region on the lefthand side of the plot. The predicted motions from the two models are plotted here as well (purple for Model 1, lime-green for Model 2). The average error for the models is on the order of  $\sim 0.1$  mas yr $^{-1}$ . Model 2 allows for a direct collision between the SMC and LMC while Model 1 assumes they do not. At the start of the Bridge ( $\sim 2$  degrees from the SMC) Models 1 and 2 begin diverging, with Model 2 motions having a similar trend as both the observed RG and MS star motions. (Right) Same as the left plot but for motion along the  $y$ -axis. Near the start of the Bridge, Models 1 and 2 do not provide significant discriminating power. However, as Model 1 continues for the length of the Bridge, we observe a clear divergence from the data for both the RG and MS stars on approach to the LMC-side of the Bridge.

## Chapter 4

# Deciphering the Kinematic Structure of the Small Magellanic Cloud through its Red Giant Population

The following text is in preparation for an upcoming manuscript and has been lightly edited for this format.

### Summary

We present a new kinematic model for the Small Magellanic Cloud (SMC), using data from the *Gaia* Data Release 2 catalog. We identify a sample of astrometrically well-behaved red giant (RG) stars belonging to the SMC and cross-match with publicly available radial velocity catalogs for SMC RGs. We create a mock spatial model of the SMC using the observed RG spatial structure and a distance distribution derived from the RR Lyrae population. We examine the kinematic effects of changing the assumed dynamical center, the systemic proper motion (PM), the addition of a rotating disk, and for the first time in SMC observational modeling, the effects of tidal expansion due to the LMC. We then compare this mock 3D kinematic cata-

log to the observed PMs and radial velocities of the SMC RG population. We find a combination of rotation and tidal expansion is required to explain the kinematic signatures. Our best-fit model presents a clear divergence from previously inferred rotational geometries, including the SMC HI gas model and the red giant (RG) radial velocities (RVs) model. This extends to both the inferred kinematic center, which is closer to the center measured from RR Lyrae, and the systemic PM of the RG population, which appears significantly more westward than the PM measured using a mix of old and young tracers. Taken together this suggests the need to treat the SMC as a series of different populations with distinct kinematics.

## 4.1 Introduction

More than a decade ago, our paradigm for the Magellanic Clouds shifted with the measurement of proper motions for the Large and Small Magellanic Clouds (LMC and SMC, respectively). Proper motion (PM) measurements of the Clouds made using the *Hubble Space Telescope* (*HST*) (Kallivayalil et al. 2006a,b) in conjunction with orbital integrations of their interactions with the Milky Way (MW) revealed a strong preference for the first infall scenario (Besla et al. 2007), supported by follow-up analysis shortly thereafter (Piatek et al. 2008). Since then, both the systemic properties and internal dynamics of the LMC have been well-studied (e.g., Olsen et al. 2011; Kallivayalil et al. 2013; van der Marel & Kallivayalil 2014; Platais et al. 2015). However, its smaller companion, the SMC, has proven significantly more challenging to fully characterize, in large part due to its complicated interaction history with the LMC.

In particular, the question of rotation in the SMC has remained frustratingly inconclusive. Stanimirović et al. (2004) produced one of the first detections of a

gradient in the radial velocities (RVs) of the HI in the SMC, finding that the gradient was well fit by a rotating disk, up to a velocity of  $60 \text{ km s}^{-1}$ , inclined out of the plane of the sky. An examination of RVs of the red giant (RG) population of the SMC by Harris & Zaritsky (2006) did not reproduce this, instead finding inconclusive evidence for rotation in the SMC. Interestingly, a RV study of the OBA stars in the SMC (Evans & Howarth 2008) did find evidence for rotation in the stars ( $\sim 26 \text{ km s}^{-1} \text{ deg}^{-1}$ ), albeit with a different inclination angle and line-of-nodes position angle (LON PA) than those found for the HI, creating a complicated picture of rotation in the SMC.

Two more recent studies have reinforced this disagreement between the type of tracer and the resulting inferred rotation. Dobbie et al. (2014) (hereafter D14) conducted a spatially broader study of the RG stars than Harris & Zaritsky (2006). With the larger sample, they found a measurable gradient in the RVs, inferring an observed rotation curve between  $20\text{-}40 \text{ km s}^{-1}$ , potentially larger than their measurement of the internal dispersion of the SMC ( $\sim 26 \text{ km s}^{-1}$ ), and an inclination and LON PA consistent with that of Evans & Howarth (2008). While it may seem unusual, the detection of a rotational signal in the SMC at larger radii but not smaller radii is consistent with results of SMC simulations (Besla et al. 2012).

For HI, Di Teodoro et al. (2019) (hereafter DT19) provided the highest resolution measurements of the gas in the SMC to date. Using the new measurements, they found a plane of rotation consistent with that originally inferred by Stanimirović et al. (2004), with improved errors and constraints on the uncertainty in the model fit. Intriguingly, a slight preference for this rotational geometry was also found in a more recent analysis of OB stars by Lamb et al. (2016), at odds with other stellar measurements. However, for all of these works, a key uncertainty lies in only measur-

ing motion in one direction, leaving open the possibility for PM measurements (that complete the 3D velocity vector) to potentially begin to resolve these tensions.

The first PM insights about the internal kinematics of the SMC began with Kallivayalil et al. (2006b), where they measured PMs for five different fields in the inner regions of the SMC with *HST*, enabling a measurement of the center-of-mass motion, but not strong constraints on the internal velocity field. Kallivayalil et al. (2013) improved the precision for these five fields, but the spatial distribution of the fields prevented further analysis into the question of rotation. van der Marel & Sahlmann (2016) used PMs from the Tycho-*Gaia* Astrometric Solution Catalog (Lindgren et al. 2016), a combination of *Gaia* Data Release 1 (Gaia Collaboration et al. 2016a,b) and the *Hipparcos* Tycho-2 Catalog (Høg et al. 2000), to add another eight PM data points to constrain the velocity field of the SMC. Their resulting analysis found inconclusive evidence for rotation, limited in part by the relatively small number of data points.

Zivick et al. (2018) attempted to expand this data set, using *HST* to measure PMs for another 28 fields, sampling a broader region around the SMC, but kept their analysis for rotation restricted to the plane of the sky as well. While the measurement of a rotation signal proved inconclusive, the analysis did reveal coherent motions in the southeastern portion of the SMC moving radially outwards, in the direction of the Magellanic Bridge and LMC, potentially indicative of tidal expansion. Finally, the release of *Gaia* Data Release 2 (DR2) (Gaia Collaboration et al. 2018b) vastly expanded the catalog of PMs for the SMC, opening up for the first time the ability for the PM data to constrain the inclination and LON PA of the rotation model in the SMC. The initial analysis of the SMC (Gaia Collaboration et al. 2018c) found a weak rotation signal throughout the SMC with a LON PA different from that measured from the RG stars in D14 and the HI in DT19. De Leo et al. (2020) presented the latest

attempt to understand the SMC internal kinematics by combining an expanded RV RG catalog with *Gaia* PMs. They found evidence for significant tidal fragmentation in the distribution of the stars but no sign of a coherent rotation curve.

Given the unusual nature of the SMC and its interaction history with the LMC, constraining the presence of rotation within the SMC may provide us a window into its previous form. The presence of coherent rotation in the outskirts of the SMC would be a marked contrast to the primarily dispersion-supported interior, suggesting that we are witnessing the transition of the SMC from a dwarf irregular galaxy to a dwarf spheroidal galaxy (Besla et al. 2012). Improving the constraints on the magnitude and direction of rotation could additionally aid in informing the set of initial conditions used in simulating the interactions between the LMC and SMC, in turn improving our understanding of their joint history with the MW as well.

In simulations we have perfect knowledge of the 6D phase space information of the motions and locations of particles, but creating a comparable observational data set is challenging. *Gaia* DR2, however, now provides us an opportunity to synthesize all the observational efforts aimed at understanding SMC structure and to begin to piece together a more holistic picture of the SMC. Here, we use a forward modeling approach, creating a mock SMC data set that we transform into observational kinematic space, with a view to match the *Gaiadata*. In addition to the tens of thousands of PMs in the *Gaia* DR2 Catalog, we cross-match with past RV studies, which are admittedly more sparse than the *Gaia* PMs, but bring us closer to producing a truly 3D observational data set for the stars. We compare this unique data set to our mock SMC to disentangle the complicated internal kinematics of the SMC.

In Section 4.2, we describe our selection of *Gaia* DR2 data, both for astrometric quality and SMC membership, as well as cross-matching with existing RV catalogs.

Section 4.3 first details the creation of our spatial model of the SMC and the kinematic model applied to create a catalog of mock data. We then discuss our methodology for a quantitative comparison to the data. In Section 4.4 we analyze previous literature results by generating a mock dataset using their inferred kinematic properties and comparing to the data. We also present our best-fit kinematic model from the explored parameter space. Finally, in Section 4.5 we summarize our efforts in modeling the SMC and forecast ahead to future work for further improving our understanding of the SMC internal kinematics.

## 4.2 Data Selection

### 4.2.1 Gaia DR2 Selection

For our analysis, we select all stars from the *Gaia* DR2 catalog within roughly 5 degrees from the optical center of the SMC using `pygacs`<sup>1</sup>. We then apply a series of initial cuts to jointly select both astrometrically well-behaved stars and stars likely to belong to the SMC. To remove MW foreground stars, we require all stars in our sample to have a parallax  $< 0.2$  mas and a proper motion within  $3 \text{ mas yr}^{-1}$  of the SMC systemic motion ( $\mu_W = -0.82 \pm 0.1 \text{ mas yr}^{-1}$  and  $\mu_N = -1.21 \pm 0.03 \text{ mas yr}^{-1}$  from Zivick et al. (2018)).

Next we apply the following cut to the renormalized unit weight error (RUWE) as described in the *Gaia* technical note GAIA-C3-TN-LU-LL-124-01:

$$\frac{\sqrt{\chi^2/(N-5)}}{u_0(G, C)} < 1.40, \quad (4.1)$$

---

<sup>1</sup><https://github.com/Johannes-Sahlmann/pygacs>

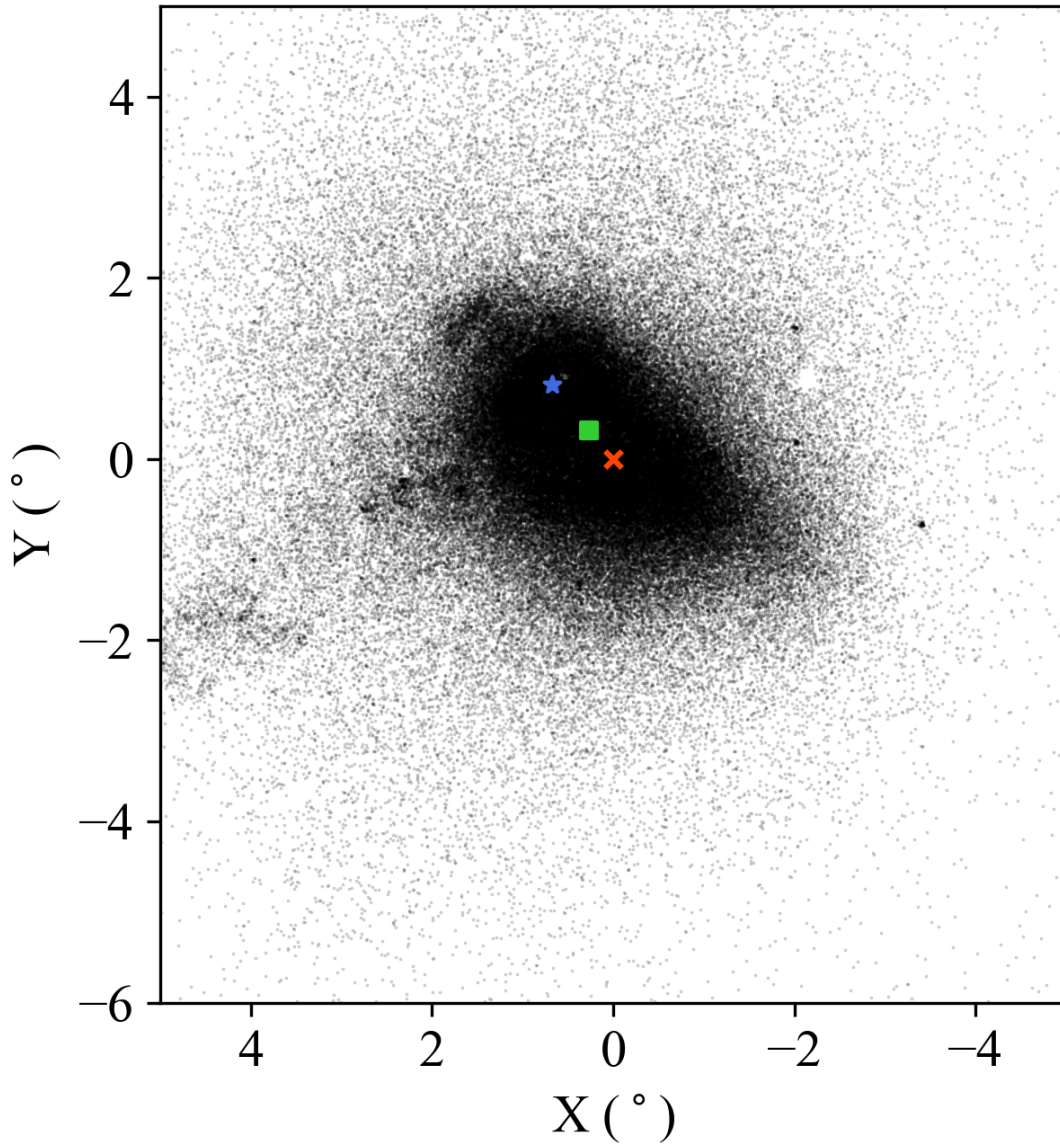


Fig. 4.1.— *Gaia* DR2 sources after initial astrometric cuts have been applied to the data, displayed in a Cartesian coordinate system as outlined in Gaia Collaboration et al. (2018c). The zero point is set to the best-fit center for the RG population (the red “x”), described in Section 4.2. The inferred kinematic center from H I gas is marked by the blue star, and the geometric center derived from the RR Lyrae population is marked by the green square. The SMC Wing can be seen on the eastern (left) side of the SMC, heading towards the Magellanic Bridge and the LMC. We also note the empty patch on the right side of the figure as the location of 47 Tuc, which has been removed from our sample by our astrometric criteria.

which uses the following *Gaia* properties:

$$\begin{aligned}
 N &\equiv \text{astrometric\_n\_good\_obs\_al}, \\
 \chi^2 &\equiv \text{astrometric\_chi2\_al}, \\
 u_0 &\equiv \text{Normalization factor } (G, C), \\
 G &\equiv \text{phot\_g\_mean\_mag}, \\
 C &\equiv \text{bp\_rp}.
 \end{aligned}
 \tag{4.2}$$

. We additionally apply a cut for the color excess of the stars, as described in Gaia Collaboration et al. (2018a) Equation C.2. As we are concerned primarily with the bright, astrometrically well-behaved stars, and to provide another check to avoid MW contamination, we select stars brighter than  $G < 18$ , leading to the final source densities in Figure 4.1. We note the conspicuous absence of 47 Tuc on the right side of Figure 4.1 as an example of the power of *Gaia* DR2 to remove potential contamination from spatially coincident sources.

With this initial astrometric selection we move to further isolate the SMC stars. Examining the color-magnitude diagram (CMD) in Figure 4.2, we identify two clear SMC stellar tracks in our sample: the main sequence (MS, marked in blue) and the red giants (RG, red). The SMC red clump is also observable near the bottom of the CMD, but due to worsening astrometric performance at  $G > 18$ , we do not examine it further in this work. We also present all sources with a cross-matched RV (see Section 4.2.2 for more details) in green.

We do note the presence of a likely third stellar sequence, a group of red supergiants (RSG) located just blueward of the RG branch, that contains a number of the RV-measurements. However, rudimentary isochrone fits to the RSG sequence find a good agreement to an age  $\sim 150$  Myr. As this age is consistent with the most recent

time of peak interaction between the LMC and SMC (Martinez-Delgado et al. 2019; Joshi & Panchal 2019), which may introduce complex kinematic signatures into the data, we choose to leave a more thorough study of this intermediate age population to a future effort.

We next consider the spatial structure of these populations in the top panel of Figure 4.7. The MS and RG populations show a marked difference in their structure. The MS stars occupy an irregular distribution, roughly tracing the main optical body of the SMC with minimal presence in the SMC halo, and with numerous smaller clumps embedded within the larger structure. The RG population, however, appears to be approximately azimuthally isotropic, with only a radial dependence for its spatial density. This difference extends into the PM space as well (bottom panel of Figure 4.7), where the center of the RG PM distribution, fit with a Gaussian, is markedly offset from the bulk of the MS PMs. The distribution of the PMs also appears different, with the RGs having a smoother distribution while the MS have clear asymmetries towards the left side of the figure. Given the smoother distribution of the RGs in both spatial and kinematic dimensions and the wealth of literature on the structure of older stars in the SMC (e.g., Subramanian & Subramanian 2012; Jacyszyn-Dobrzniecka et al. 2017), we hereafter consider only the RGs as the focus of our analysis.

### 4.2.2 Radial Velocity Cross-Matching

To attempt to provide full 3D velocity information for our selected stars, we looked to cross-match our catalog with existing RV catalogs. For this we use two publicly available catalogs: the prior work by D14 and RVs from the Apache Point Observatory Galactic Evolution Experiment 2 (APOGEE-2) (Majewski et al. 2017; Wilson et al.

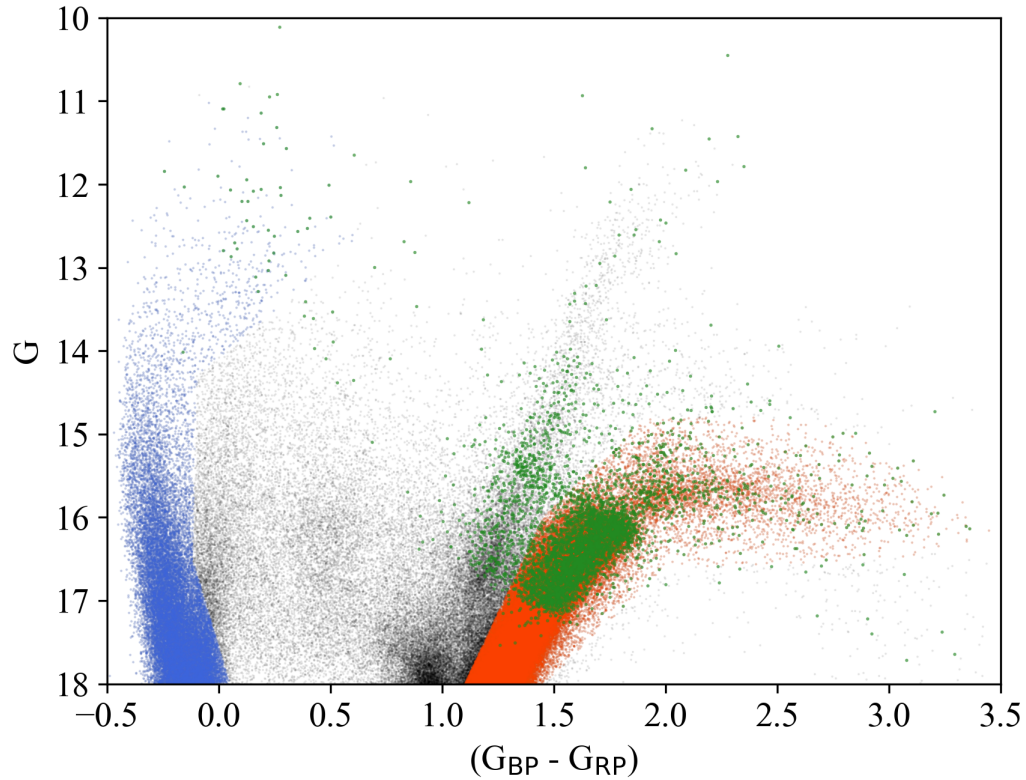


Fig. 4.2.— Color-Magnitude Diagram of all sources present in Figure 4.1. Two separate stellar sequences have been marked: the main sequence (MS) stars in blue on the left side and the red giants (RG) on the right side. The top of the red clump can be observed near  $(1.0, 18.0)$ , but due to worsening astrometric performance near  $G \sim 18$ , we have chosen not to examine it further. All sources that have been matched to an existing RV measurement (described in Section 4.2.2) are marked in green, which can be seen to mostly sample the RGs but do extend to the sequence blueward of the RGs, likely a red supergiant population in the SMC.

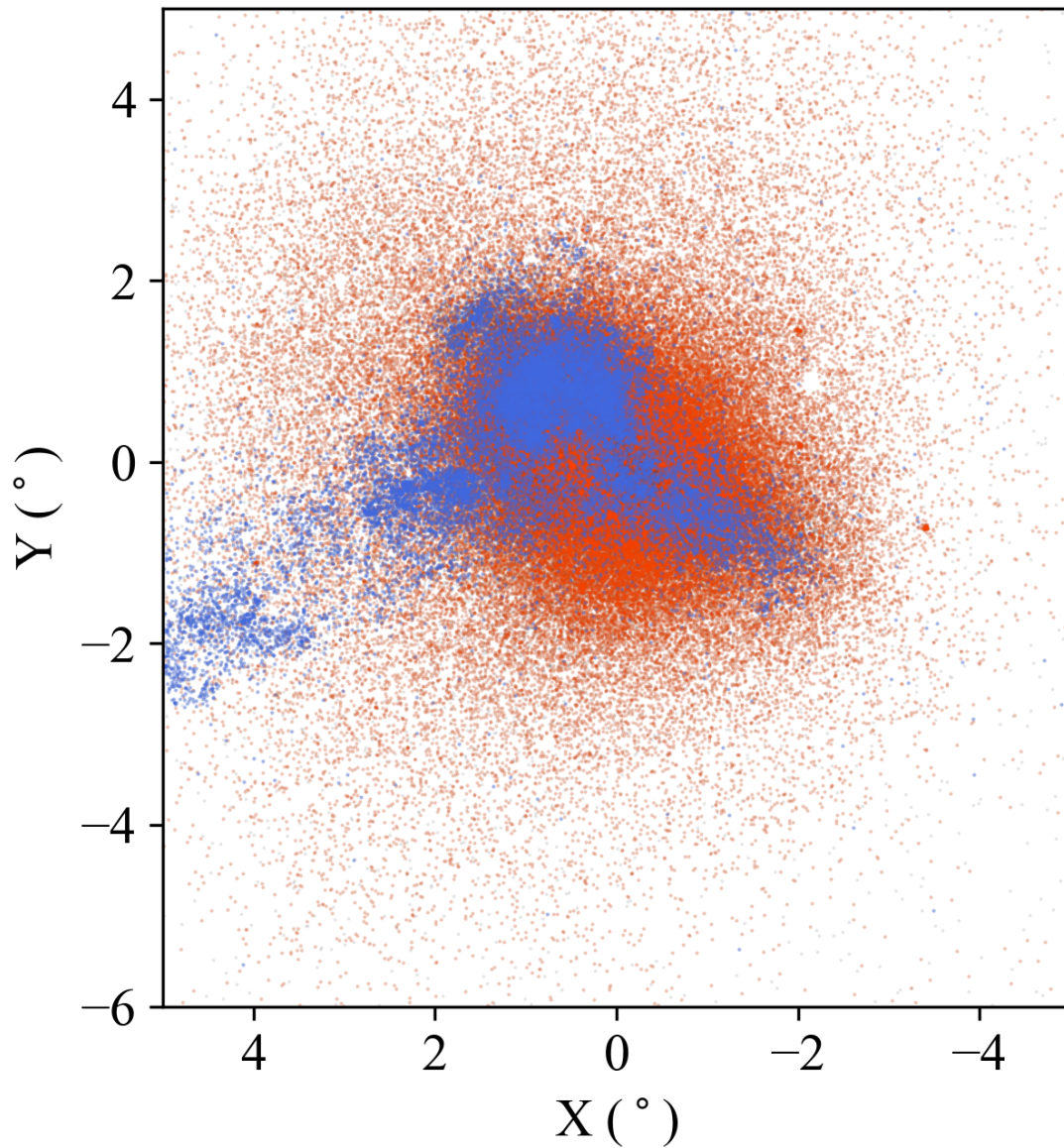


Fig. 4.3.— All SMC main sequence (MS, blue) and red giant (RG, red) stars from Figure 4.2 in the same field of view and Cartesian coordinate system as Figure 4.1. The MS stars have a clear spatial structure to them, tracing the optical main body of the SMC and stretching into the Wing, while the RGs have a significantly more well-behaved structure, appearing to be roughly azimuthally isotropic with a radial dependence for the density.

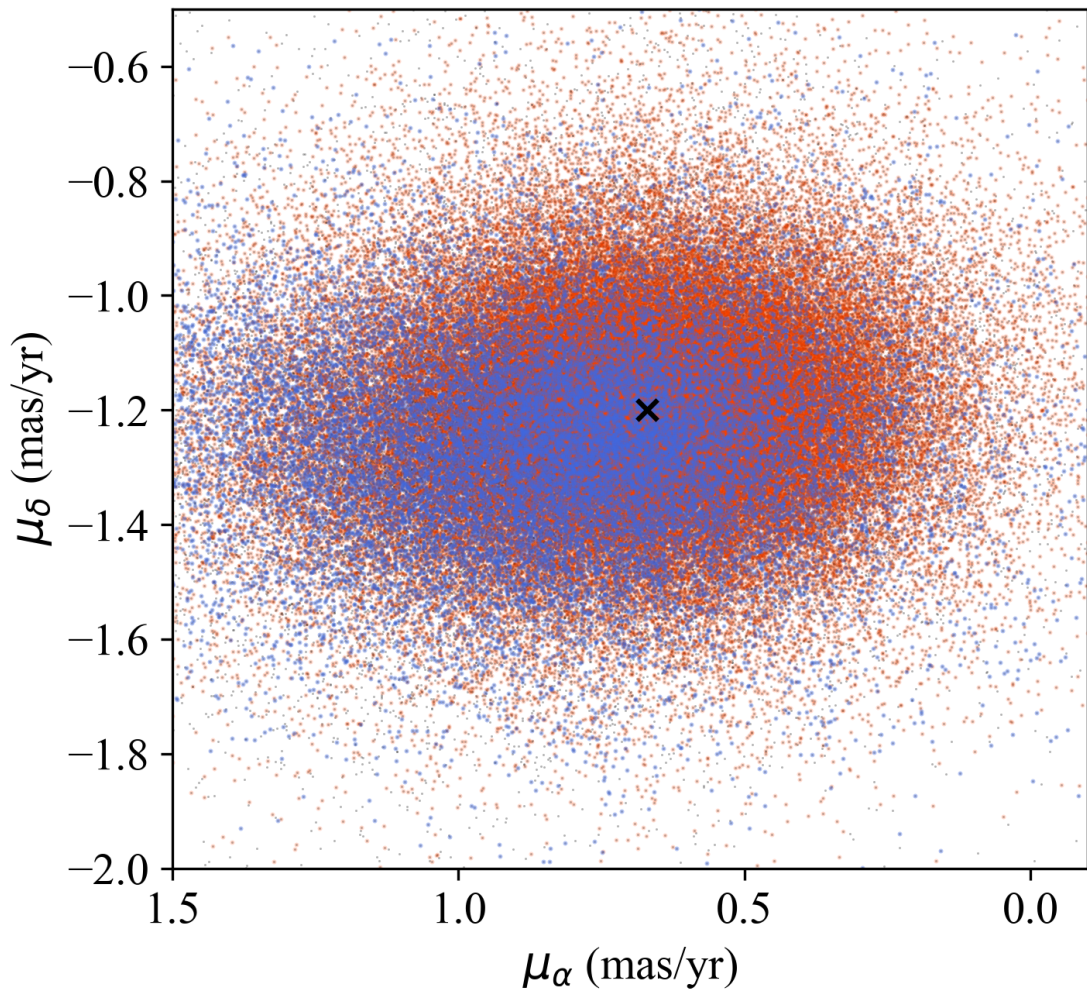


Fig. 4.4.— Distribution of the PMs of the RG and MS samples. The PM center of the RGs, measured with a simple Gaussian fit, is marked by the black “X”. The RG PM is clearly offset from where one would place the MS center, though the asymmetric extension of the MS PMs towards the left side of the figure would make it difficult to accurately assess the systemic MS PM.

2019), part of the Sloan Digital Sky Survey IV (Blanton et al. 2017) Data Release 16 (Ahumada et al. 2019). Between the two catalogs, excluding any sources that may have been double counted, we find over 4,000 sources common to our DR2 RG selection. The locations of these common sources can be seen in Figure 4.5.

For our analysis, we choose to consider both the DR2-only catalog of roughly 100,000 sources for examining the proper motion structure of the SMC and the DR2-RV list that allows us to fully probe the kinematic space. As we do not know individual distances to stars, we choose to leave our PM measurements in  $\text{mas yr}^{-1}$ , but we note for a physical interpretation of the PMs that at a distance of 60 kpc, a PM of  $0.1 \text{ mas yr}^{-1}$  corresponds to  $\sim 30 \text{ km s}^{-1}$ .

## 4.3 Data Analysis

### 4.3.1 Observational Data

Before any analysis can begin of the internal kinematics of the SMC RGs, we must first deal with correcting for viewing perspective effects, which cause the 3D motion of the SMC to project differently as we change our line of sight. However, this correction requires assumptions regarding the location (in distance and on the sky) and magnitude of the 3D motion. As *Gaia* affords us the opportunity to only examine a single stellar population instead of multiple populations combined, we choose to use the data to derive the systemic properties to be used for correcting the individual stellar motions.

For this, we fit two 2D Gaussians to the spatial and PM distributions of the RGs, finding a center of  $((\alpha, \delta) \text{ (J2000)} = (13.04^\circ, -73.10^\circ))$  and a systemic RG PM of  $((\mu_\alpha, \mu_\delta) = (0.67 \text{ mas yr}^{-1}, -1.20 \text{ mas yr}^{-1}))$ . These centers are marked in Figures

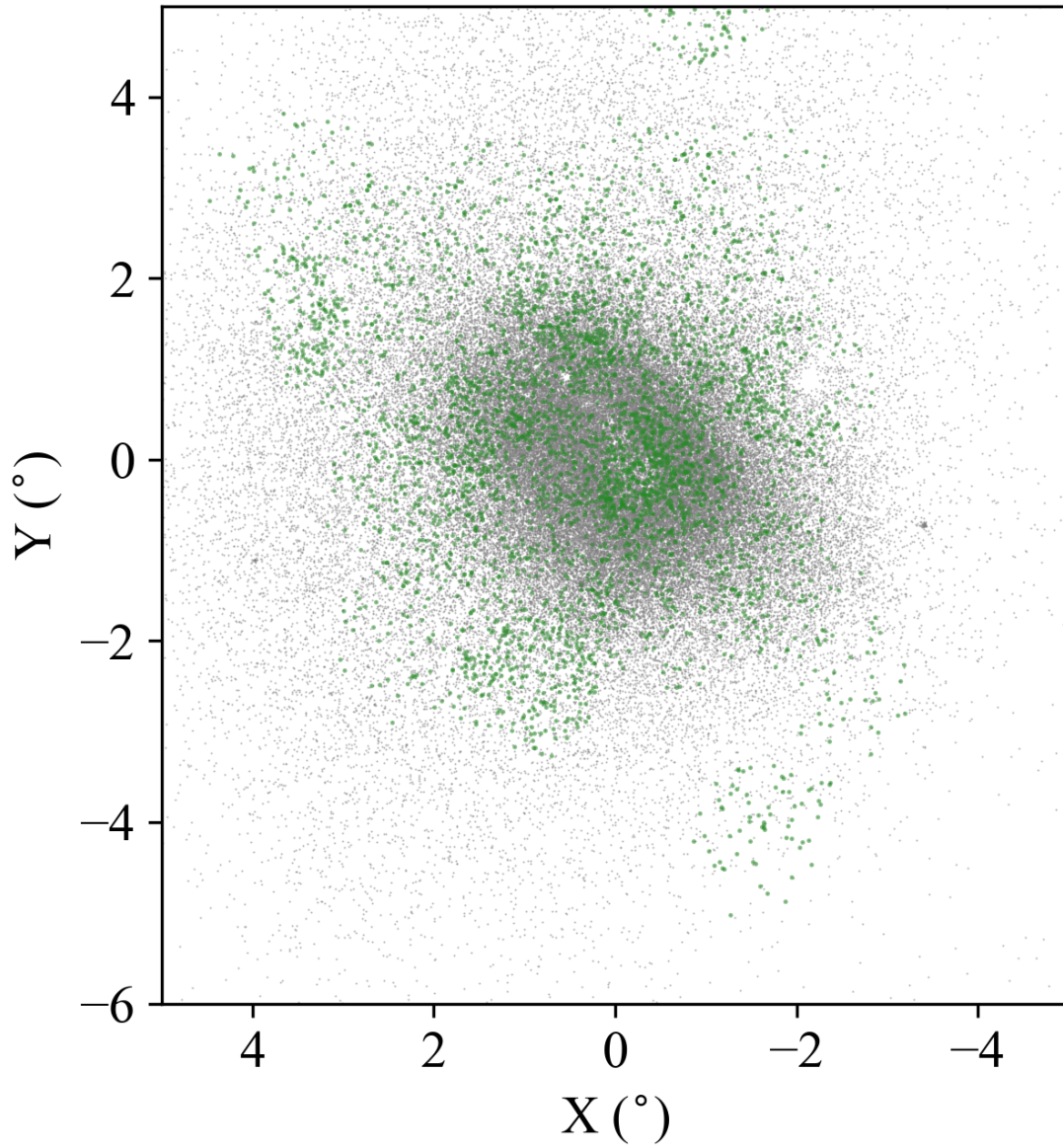


Fig. 4.5.— Spatial locations of all RG stars (same Cartesian frame as in Figure 4.1) selected for analysis. The stars possessing a measured RV are marked in green. The resulting distribution of RV stars does favor the interior of the SMC but coverage is available for much of the RG distribution.

4.1 and 4.3 and the systemic PM is marked in Figure 4.4. The center generally agrees well with previous analyses of the RG structure in the SMC (Jacyszyn-Dobrzniecka et al. 2017, e.g.), and the PM value is in line with other *Gaia*-based measurements of the RG systemic motion (De Leo et al. 2020, e.g.). For a distance, we use the estimates from Jacyszyn-Dobrzniecka et al. (2017) for a distance modulus of  $(m-M) = 18.91$ .

With these three values in hand, we subtract the systemic PM and perspective correction from each individual PM. For analysis, we convert the PMs into a Cartesian frame as outlined in Gaia Collaboration et al. (2018c). For display, the 100,000 stars are binned every 0.2 degrees and the average PM is calculated. The resulting averaged relative SMC RG PMs are displayed in Figure 4.6.

As other prior analyses have noted, there is a clear outward motion, particularly on the eastern side of the SMC towards the direction of the Magellanic Bridge. However, *apparent rotation can be seen in the center of the SMC* with the averaged residual vectors displaying a distinct counter-clockwise pattern in the inner 2 degrees of the SMC.

The idea of tidal expansion has often been invoked in trying to understand the residual PMs in the outer part of the SMC. To place this idea into context, we calculate the relative velocity between the LMC and SMC. We use the new systemic motion for the RG population and take care to perform this subtraction in 3D Galactocentric coordinate space before transforming the relative velocity back into observable quantities (where we find the relative velocity in our Cartesian frame to be  $(\mu_z, \mu_y, v_z) = (0.43 \text{ mas yr}^{-1}, -0.21 \text{ mas yr}^{-1}, -32.8 \text{ km s}^{-1})$ ). The PM components of this relative velocity, which we will refer to as  $\mu_{\text{LMC-SMC}}$ , are displayed as the dark red vector at (0,0) in Figure 4.6.

Immediately we see that the direction of  $\mu_{\text{LMC-SMC}}$  agrees well with the general direction of the residual PMs in addition to the minor axis of the SMC. Combined with the hint of coherent rotation in the interior of the SMC, we propose that the internal velocity field of the SMC can be roughly modeled by two mechanisms: a cylindrical rotation and a linearly increasing tidal component. To fully understand this parameter space, we move to attempting to build a 3D model of the SMC, as described in the following Section.

### 4.3.2 Mock Data Creation

To create the mock SMC data set, we make the assumption that the RG population can be approximately modeled using a simple Gaussian distribution for each spatial dimension. For the dimensions in the plane of the sky, we use the values from the earlier 2D Gaussian fit to the RG *Gaia* data. We find a standard deviation of approximately 1.3 kpc for the longer axis and 1.0 kpc for the shorter axis with a rotation of  $\sim 55$  degrees. For the line-of-sight (LOS) depth, we refer to Jacyszyn-Dobrzniecka et al. (2017) for their measurements of the RR Lyrae distances and axial ratios in the SMC. Additionally, as has been shown, the range of LOS distances varies in the SMC as a function of spatial position. To account for this, we adopt a simple prescription in assigning the Gaussian mean for the distance distribution, which is able to reproduce the observed tilt in the SMC (with the southeastern corner being the closest to the observer and the northwestern corner being the furthest).

We then apply a random subsampling to the central region of our model to reflect the loss in astrometrically well-behaved stars observed in the RG *Gaia* data. At this point we note that in the *Gaia* data there appears to be two different stellar components: a dense core, relatively well-fit by a 2D Gaussian, and an offset halo of

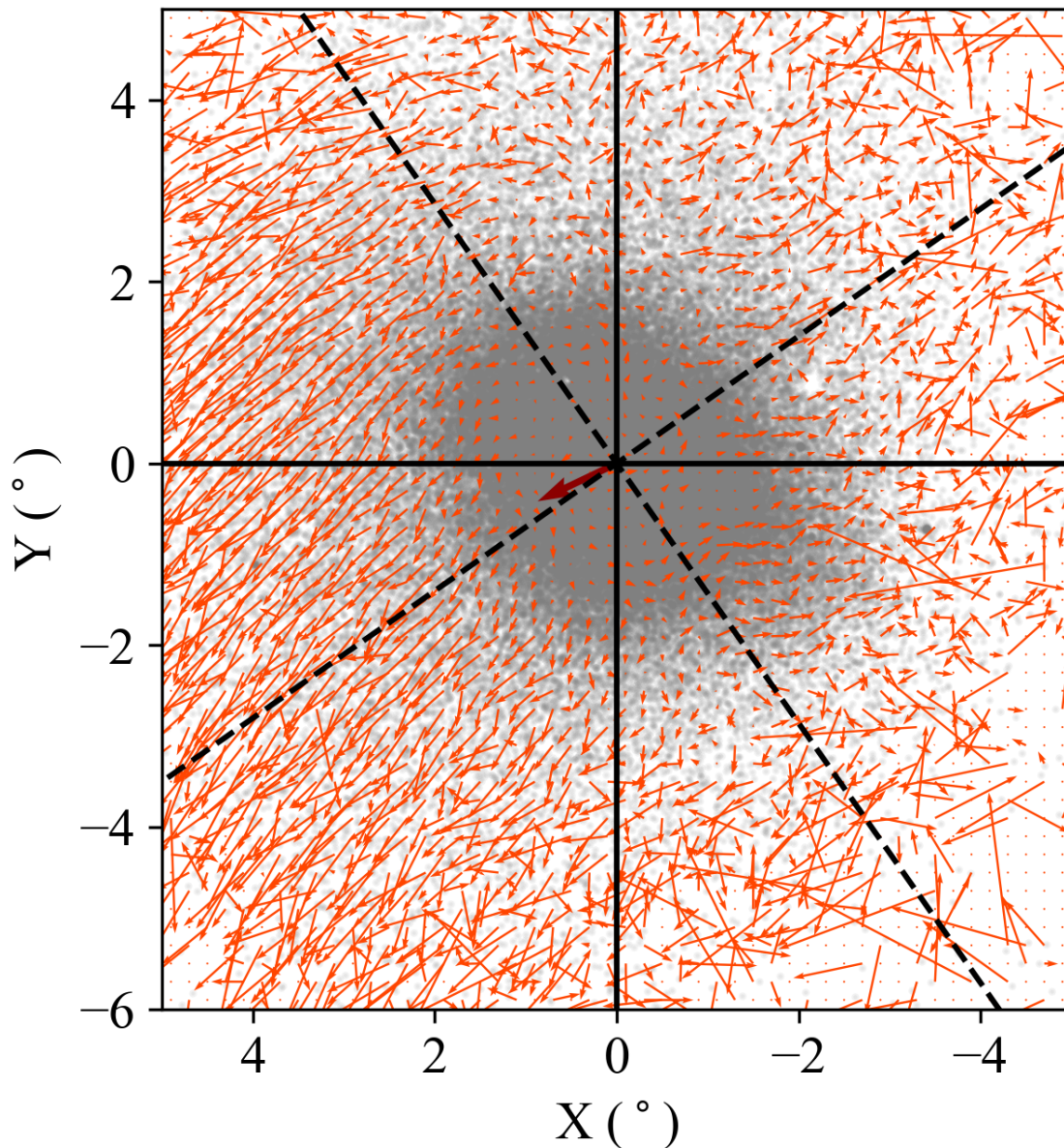


Fig. 4.6.— The average residual PM vectors of the SMC RGs as a function of location in the SMC. The gray points mark all RG stars used in the averaging. The solid black lines indicate the original Cartesian coordinate system, and the dashed black line marks the rotated frame where the  $x$ -axis lies along the major axis of the SMC RG distribution. The dark red vector marks the relative velocity, as projected on the sky, between the LMC systemic motion and the SMC systemic motion,  $\mu_{\text{LMC-SMC}}$ . Clear outward motion can be seen on the eastern side of the SMC, consistent with the direction of  $\mu_{\text{LMC-SMC}}$ , while coherent rotation appears to be located in the center of the SMC.

stars (offset as it appears to extend significantly further to the northeast). As this may represent a separate component of the SMC with unique kinematic properties, we choose to only model the dense core of the SMC, resulting in the model seen in Figure 4.7. We also observe that our modeling does not quite capture the apparent boxy-ness of the observed data. However, as we are focused on developing a simple physical intuition for SMC kinematics, we believe the model to be appropriate for our purposes.

With a 3D spatial model complete, we turn to assigning velocities to each of our mock stars. For this, we adopt the formalism outlined in van der Marel et al. (2002)(hereafter vdM02) to describe observations of a rotating solid body whose center of mass (COM) has some non-zero 3D motion. For more description, we refer the reader to that work. Here we will provide an outline of the key concepts used in creating the kinematic model, including the mechanisms described earlier. The kinematics for each star in our model can be described with the following:

$$\begin{pmatrix} v_1 \\ v_2 \\ v_3 \end{pmatrix} = \begin{pmatrix} v_1 \\ v_2 \\ v_3 \end{pmatrix}_{\text{CM}} + \begin{pmatrix} v_1 \\ v_2 \\ v_3 \end{pmatrix}_{\text{int}} + \begin{pmatrix} v_1 \\ v_2 \\ v_3 \end{pmatrix}_{\text{pn}} + \begin{pmatrix} v_1 \\ v_2 \\ v_3 \end{pmatrix}_{\text{tidal}}, \quad (4.3)$$

where the different velocity components are:  $v_{\text{CM}}$ , the center-of-mass motion of the SMC;  $v_{\text{pn}}$ , the precession and nutation of the velocity plane of the SMC;  $v_{\text{int}}$ , the internal rotation and dispersion of the SMC; and  $v_{\text{tidal}}$ , the tidal expansion due to the interactions with the LMC.

For the initial  $(x, y, z)$  frame, we orient it such that  $(0, 0, 0)$  is located at the dynamical center of the SMC, with positive the  $z$ -axis pointing in the direction of the observer, the positive  $x$ -axis towards the west, and the positive  $y$ -axis pointing north.

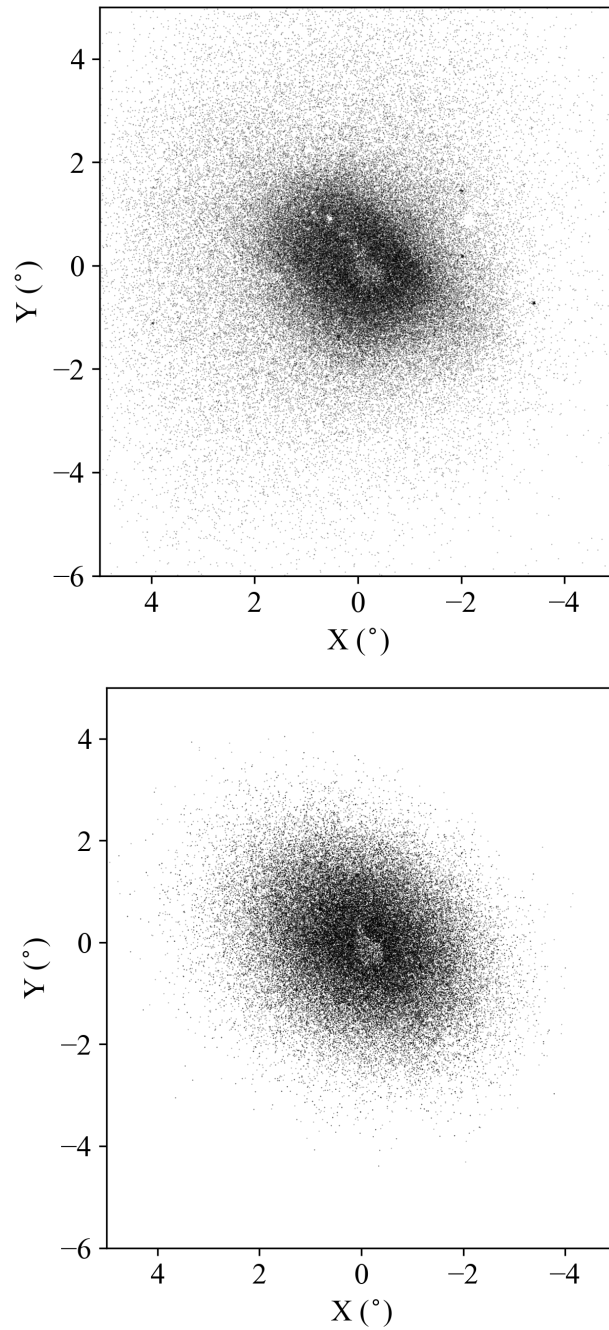


Fig. 4.7.— **(Top)** All RG stars in our selected sample plotted using our Cartesian frame. The small, tightly clumped dark areas in the plot are believed to be globular clusters or other stellar associations belonging to the SMC. **(Bottom)** All model stars, scaled to qualitatively match the observational data, plotted in our Cartesian frame. The central underdensity present in the data has been artificially created in the model in an effort to reflect observations.

We first assign  $(x, y, z)$  coordinates for each star in our SMC model then use these coordinates to calculate angular coordinates in the frame of the observer (distance,  $\rho, \phi$ ), following Eq. 2 from vdM02. These coordinates inform the decomposition of the different velocity Cartesian components into the  $(v_1, v_2, v_3)$  frame (hereafter the  $v_i$  frame).

To calculate  $v_{\text{CM}}$ , the model is created with an initial kinematic center  $(\alpha_0, \delta_0, D_0)$  and associated motion  $(\mu_\alpha, \mu_\delta, v_{\text{sys}})$ . Using these quantities, the transverse velocity ( $v_t$ ) and direction of the transverse velocity ( $\Theta_t$ , measured east over north) are calculated. Combined with the star’s angular coordinates, we use Eq. 13 from vdM02 to calculate the velocities for each star given its angular position on the sky.

For  $v_{\text{int}}$ , we assume a linearly increasing rotation curve, with a maximum velocity of  $V_0$  at a scale radius of  $R_0$ , after which the rotation flattens out, as described in Equation 4.4.

$$V(R') = \begin{cases} \frac{R'}{R_0} V_0 & R' < R_0 \\ V_0 & R' \geq R_0 \end{cases} \quad (4.4)$$

For simplicity, we assume cylindrical rotation, where  $R'$  is only dependent on the  $x'$  and  $y'$  coordinates of the star in the rotating frame, denoted by  $'$ . For the plane of rotation, we define an inclination  $i$  and a LON PA  $\theta$  to describe the orientation of the plane with respect to the internal spatial frame of the galaxy. We then convert the internal Cartesian vectors to the  $v_i$  frame using Eq. 21 from vdM02. Once in the  $v_i$  frame, we add a velocity “kick” to each component, randomly drawn from a normal distribution using  $26 \text{ km s}^{-1}$  (from D14) as a standard deviation.

As a brief aside related to the internal motions, we note that we are aiming to only model the observable motions of the SMC. As such, we are not considering

asymmetric drift when reporting our final rotation curves. For the SMC, the known dispersion in the RG population of  $> 20 \text{ km s}^{-1}$  would require significant corrections in order to model the rotation curve predicted by the underlying gravitational potential. However, the observational impact of asymmetric drift on older stellar populations, the flattening of the rotation curve beyond a certain scale radius due to random kicks and perturbations experienced by individual stars, mirrors the model we apply for rotation. As such, our modeled rotation can be understood as the curve measured for non-drift-corrected motion, just as one would measure in the raw *Gaia* data as well.

For  $v_{\text{pn}}$ , knowledge of the time dependency of  $d\theta/dt$  and  $di/dt$  is required. For the SMC, there are no known constraints for  $d\theta/dt$ , so we choose to not include it in the modeling. Attempts have been made at constraining  $di/dt$  in the SMC (e.g., Di Teodoro et al. 2019; Dobbie et al. 2014), but the parameter space is still fairly unconstrained. Additionally, for an object the size of the SMC, contributions from even a fairly large  $di/dt$  would only account for up to a few  $\text{km s}^{-1}$  in the radial velocity component, significantly smaller than our uncertainties from other factors. As such we choose to not include  $v_{\text{pn}}$  in our final calculation.

For  $v_{\text{tidal}}$ , given the complex gravitational interactions between the SMC and LMC, we do not attempt a rigorous numerical analysis. Instead, we use the expectation that tidal expansion should occur along the direction of relative motion between the two bodies to create a prescription for the individual stars, as seen in numerical simulations of dispersion-supported systems on plunging orbits into larger hosts (e.g., Peñarrubia et al. 2009). Contrary to more conventional expectations of tidal behavior, no contraction in the satellite’s stellar population appears. Instead stars are evacuated out of the satellite across all locations, rather than only through the Lagrange points as observed in tidally disrupted globular clusters in the MW. As described earlier

in Section 4.3.1, we calculate the relative velocity,  $v_r$  between the LMC and SMC to determine the direction of the tidal component, which for simplifying purposes we will assume to be fixed for every star. For the magnitude of the motion for an individual star, we use the distance from the SMC center along the axis of relative motion,  $d_i$ , in conjunction with a scaling ratio between of 10 and 30 km s<sup>-1</sup> kpc<sup>-1</sup>,  $v_t$  (the possible range based on the relative motions in the Magellanic Bridge in Zivick et al. 2019), giving the final tidal contribution for each star, displayed below in Equation 4.5.

$$\vec{v}_{tidal} = d_i \cdot v_t \cdot \frac{\vec{v}_r}{\|\vec{v}_r\|} \quad (4.5)$$

With all of the components combined together in the  $v_i$  frame, we then convert these physical velocities (km s<sup>-1</sup>) into observed motions (mas yr<sup>-1</sup> for  $\mu_\alpha$  and  $\mu_\delta$ ) using Eq. 9 from vdM02. We add a random kick, selected from a Gaussian distribution with standard deviation of 0.15 mas yr<sup>-1</sup>, calculated using the RG PM errors in Section 4.2, to the measured  $\mu_\alpha$  and  $\mu_\delta$ , to reflect the uncertainties in the *Gaia* DR2 catalog. This results in a final catalog for our model of stars, with each one possessing (RA, Dec,  $\mu_\alpha$ ,  $\mu_\delta$ ,  $v_{LoS}$ ) comparable to the data.

For the RV catalog, as the selection was not spatially random in D14, we choose to adopt the same spatial sampling. In the plane of the sky, for each RV star, we select the closest neighbor from our model to create our RV subcatalog, consisting in total of  $\sim 4,200$  stars.

### 4.3.3 Comparison Quantification

To quantify our data, we require that our model be able to reproduce both the magnitude of the residual motions and the location of the residual motions. To that end, we construct a set of spatial vs kinematic comparisons for all possible

permutations of observable quantities (e.g.,  $\mu_x$  vs  $x$ ,  $\mu_y$  vs  $x$ ), leaving us with six different comparisons to consider (as in observable space we are not able to access PMs/RVs as a function of LOS distance).

For a choice of the  $x/y$  frame, we adopt the SMC's shape as a natural frame, assigning the  $x$ -axis to align with the major axis and the  $y$ -axis to align with the minor axis of the SMC RG distribution (as seen by the dashed black lines in Figure 4.6). After rotating the positions and PMs of the RGs into this new frame, we bin the PMs along the spatial axis, using the Freedman-Draconis Rule to set the bin width (Freedman & Diaconis 1981) to avoid over-fitting the data. We set the bin widths using the observational data but limit the comparison between model and data to only bins containing model data.

The residual PMs in each bin are then averaged with a standard deviation calculated. For each proposed kinematic model, a  $\chi^2$  is calculated for each of the four spatial-kinematic permutations, factoring in both the standard deviation of the data and the mock model. Bins with fewer than 5 stars are excluded from this calculation to avoid unintentionally biasing the comparisons towards sparsely sampled outer regions of the SMC model. To compare model to model, the four separate  $\chi^2$  values are summed to produce a single statistic that is then minimized.

We attempted this process for the RV sample, but we found between the smaller sample size (4,200 RV stars vs 100,000+ PM-only stars) and uneven spatial sampling that the calculated  $\chi^2$  values for the RV sample were insufficient to properly constrain the model-to-data comparisons. We did use the expected RVs as a qualitative check with the PM-only best-fits, but for final determination of the best-fit model, the PM-only  $\chi^2$  was used.

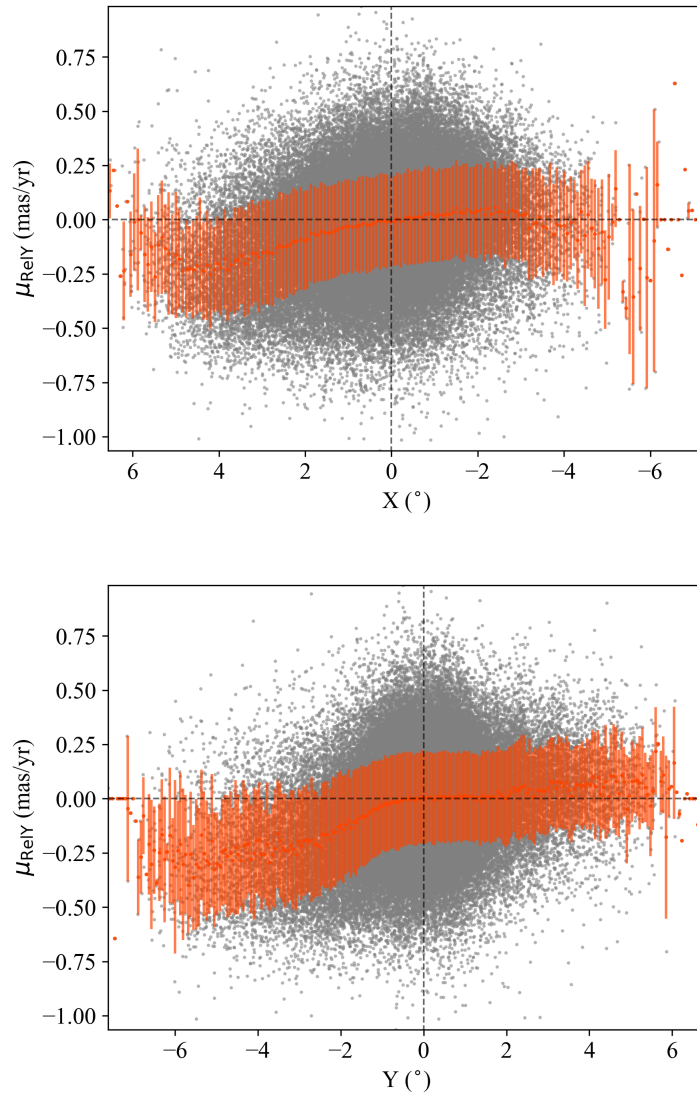


Fig. 4.8.— Residual PMs plotted against spatial position in the SMC geometric major/minor axis frame. The gray points are all of the RG stars in the same. The stars are binned accordingly to the spatial sampling, which is about 0.08 degrees in  $X$  and 0.06 degrees in  $Y$ . A simple average is taken for each bin, marked by the orange-red point, and the standard deviation of the bin is shown as the error bar. **(Left)** Residual PM in  $Y$  (which points roughly along the axis of relative LMC-SMC motion) as a function of position in  $X$  (which spans the major axis of the SMC, with the positive  $X$  direction north of the Magellanic Bridge). **(Right)** Residual PM in  $X$  as a function of position in  $Y$ .

## 4.4 Model-to-Data Comparison Results

### 4.4.1 Best-fit Results

In exploring the parameter space, given the imperfect 3D SMC model and the new forward-modeling approach to understanding the internal kinematics, we choose to focus our analysis on five key parameters of the model: inclination angle  $i$ , the position angle of the Line of Nodes (LON)  $\Theta$ , the rotation velocity  $V_0$ , the scale radius  $R_0$ , and the tidal expansion scale factor  $V_{tidal}$ . For our initial analysis in attempting to build our physical intuition for the SMC kinematics, we simply test the parameter space in discrete steps for each of the parameters.

For the remainder of the parameters, we choose to keep the distance  $D_0$ , the proper motion  $(\mu_W, \mu_N)$ , center  $(\alpha_0, \delta_0)$ , and the systemic velocity  $V_{sys}$  fixed to the values used in the original RG analysis. For the distance and systemic velocity, both have already been better established for the RG population in prior studies (Jacyszyn-Dobrzyniecka et al. 2017; Dobbie et al. 2014, e.g.). For the center and systemic PM, as we have already measured them based on the data, we choose not to test them to avoid introducing unexpected biases in our  $\chi^2$  calculation. Finally, as described earlier, given the large degree of uncertainty and relatively small effect of the precession/nutation,  $di/dt$ , we do not include it.

The parameter space step frequency for each parameter is as follows:

- $i$ : every 10 degrees from 0 to 90 degrees (rotation in plane of sky vs edge-on rotation)
- $\Theta$ : every 10 degrees from 0 to 360 degrees
- $V_0$ : every 5 km s<sup>-1</sup> from 0 to 30 km s<sup>-1</sup>, which probes the lower to upper range of previous inferred values for the SMC stellar component

- $R_0$ : every 0.5 kpc from 0.5 kpc to 2.5 kpc
- $V_{tidal}$ : every 5 km s<sup>-1</sup> kpc<sup>-1</sup> from 0 km s<sup>-1</sup> kpc<sup>-1</sup> to 25 km s<sup>-1</sup> kpc<sup>-1</sup>

After creating a mock set of data for each permutation of the above parameter space steps, the summed  $\chi^2$  values were compared. Across the best-fitting models, we find a need for both a non-zero rotation ( $V_0$  between 15-25 km s<sup>-1</sup> with  $R_0$  of around 1 kpc), at a relatively high inclination ( $i$  between 60-80 degrees) with a LON oriented from northeast to southwest ( $\Theta$  around 210-270 degrees), and a non-zero tidal expansion component ( $V_{tidal}$  near 15 km s<sup>-1</sup> kpc<sup>-1</sup>). The specific best fit values and comparisons to literature values can be found in Table 4.1. Estimates on the uncertainty in the model fitting can be found in Table 4.2, where the errors have been estimated using the distribution widths of the 50 best-fitting models. Figure 4.9 shows the residual vector plot of the model with the smallest  $\chi^2$  value, which displays similar key characteristics to the *Gaia* data: large and roughly linear motion in the eastern portion of the SMC and a weak signal of rotation within the inner 1 degree of the spatial distribution.

We can see this in the spatial-kinematic comparisons in Figure 4.11, where our model is able to capture the behavior across much of the SMC, including unusual asymmetric behavior in the  $Y$  vs  $V_Y$  space. We do note some deviations from the observations, in particular in the southwestern region of the SMC (negative  $X$  in the spatial-kinematic plots) where we are unable to fully capture that behavior. This can be seen in the residual vectors plots as well, where the stars to the southwest of the SMC display a larger western motion than would be expected from our simple tidal+rotation model (the *Gaia* RG residual PMs and the model residual PMs can be seen contrasted in Figure 4.12). However, the eastern portion of the SMC appears to be well-described by our model, including capturing the rotation signal layered on

top of the large tidal motions as they subtly change the direction of the stars, offset from relative LMC-SMC vector, as a function of azimuth.

As a final check on our best-fit model, we compare our predicted RVs to the cross-matched RV catalog. In Figure 4.10, we display all *Gaia* stars with a residual RV calculated for them in the top panel and the bin-averaged residual RVs from the best-fit model. In the RV data, we do not see any obvious patterns that would make for an easy constraint on the modeled RVs. We also observe that for our best-fit model, the strongest residual RV signals will appear far to the northeast and southwest of the SMC, both areas which are noticeably undersampled in the RV data. This mismatch of predicted high leverage area and observed data, combined with the lack of distance information for individual RVs that are shown to have a strong dependence on LOS depth, and it becomes difficult to assign a clear significance to the data-model comparison. In future spectroscopic surveys, continuing to expand the coverage in the outer regions of the SMC will be crucial.

#### 4.4.2 Existing Proposed Scenarios

While our tidal+rotation model is well equipped to described the observed PM distributions in the *Gaia* data, we also create mock sets of data using the inferred models from D14 and DT19 to help identify the underlying differences.

In the case of D14, we can see that the prescribed rotation would be far too large a signal in the PMs to be possible. However, we note that their inferred LON (122 degrees) in the rotation is in line with the direction of the relative LMC-SMC velocity, which has a non-zero component in the LOS velocity. For DT19, we find a similar axis of rotation, which isn't necessarily expected for gas vs old stellar kinematics. However, it appears to be reversed, where the gas on the eastern side of the SMC is

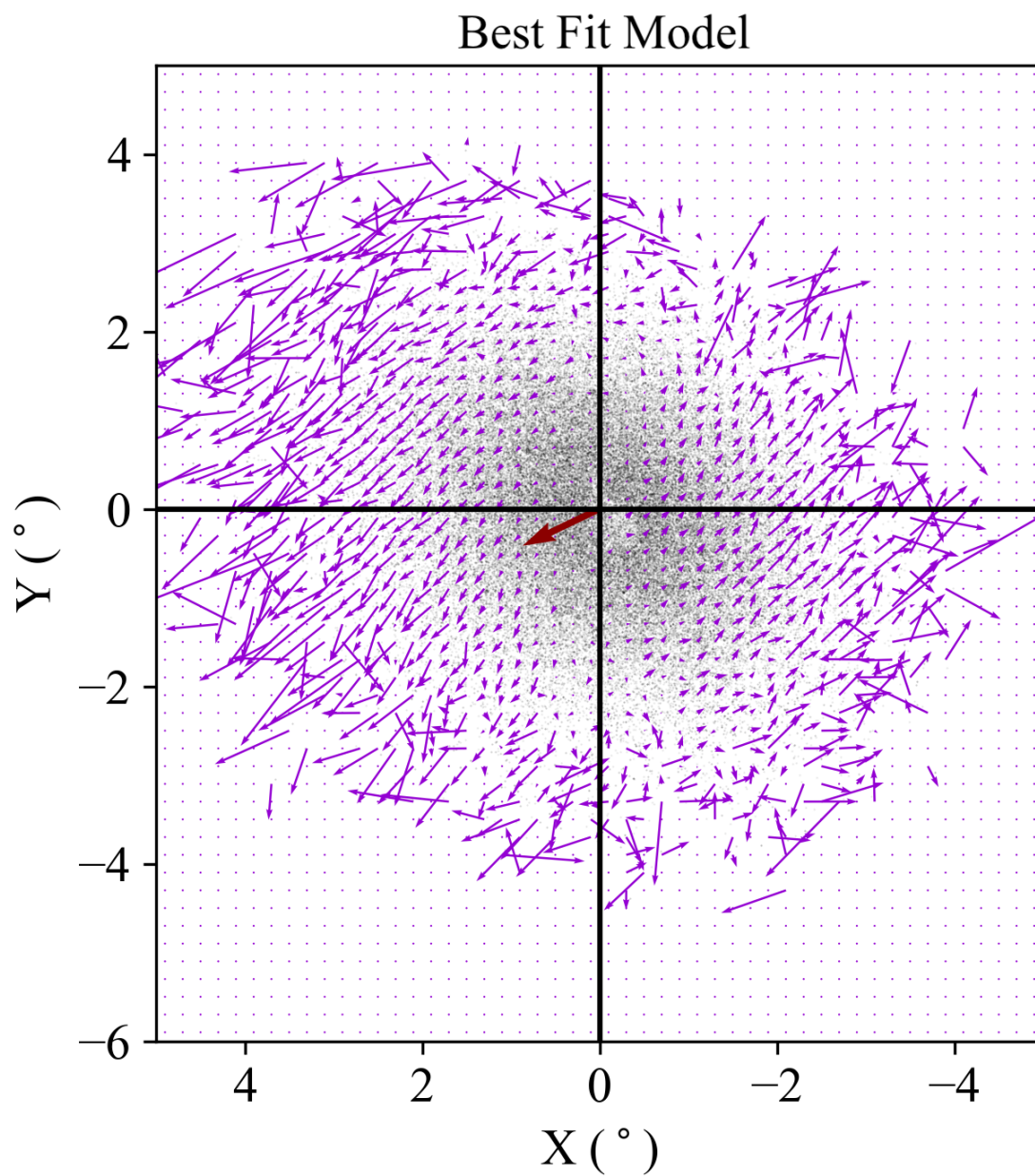


Fig. 4.9.— Residual PM vectors for the best-fit model to the data (specifics can be found in Table 4.1), displayed in the same format as Figure 4.6. Unlike the data, the residual vectors are limited to the area encompassed by a single 2D Gaussian function that had been fit to the original RG distribution.

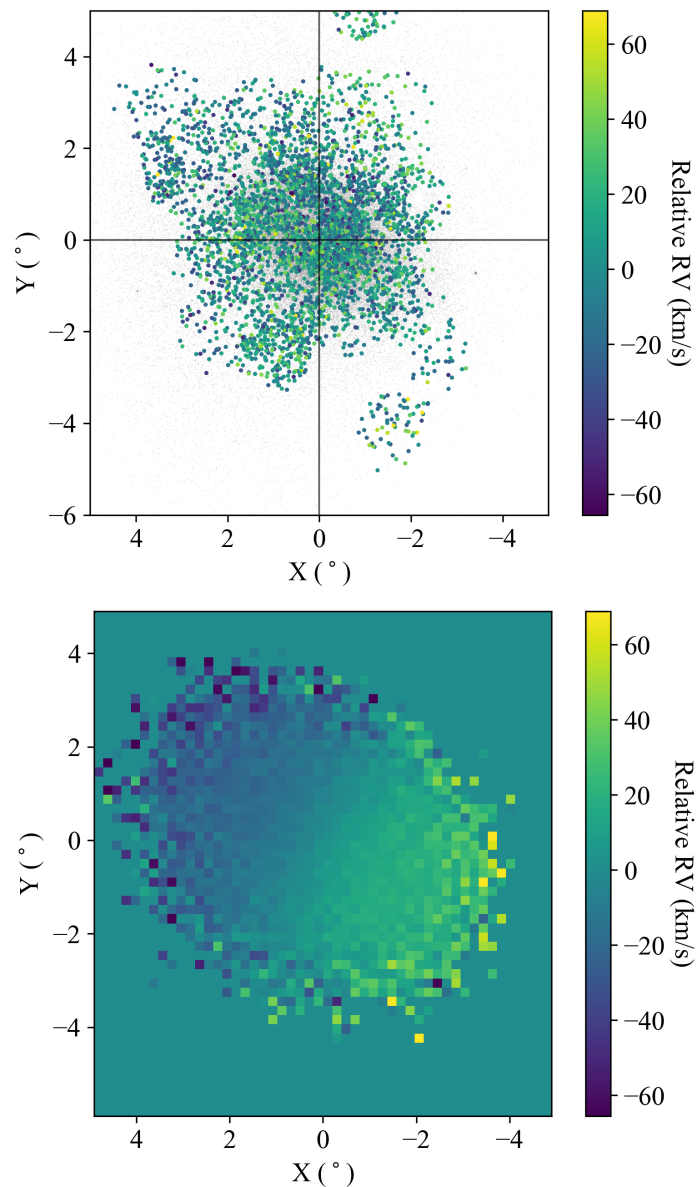


Fig. 4.10.— **(Left)** Spatial positions of the *Gaia* sample with cross-matched RVs, color coded by the residual RV (after removing the SMC systemic RV and correcting for viewing perspective). The non-RV stars for each respectively stellar population are marked by the grey points in the background. **(Right)** Bin-averaged residual RVs from the best-fit model. .

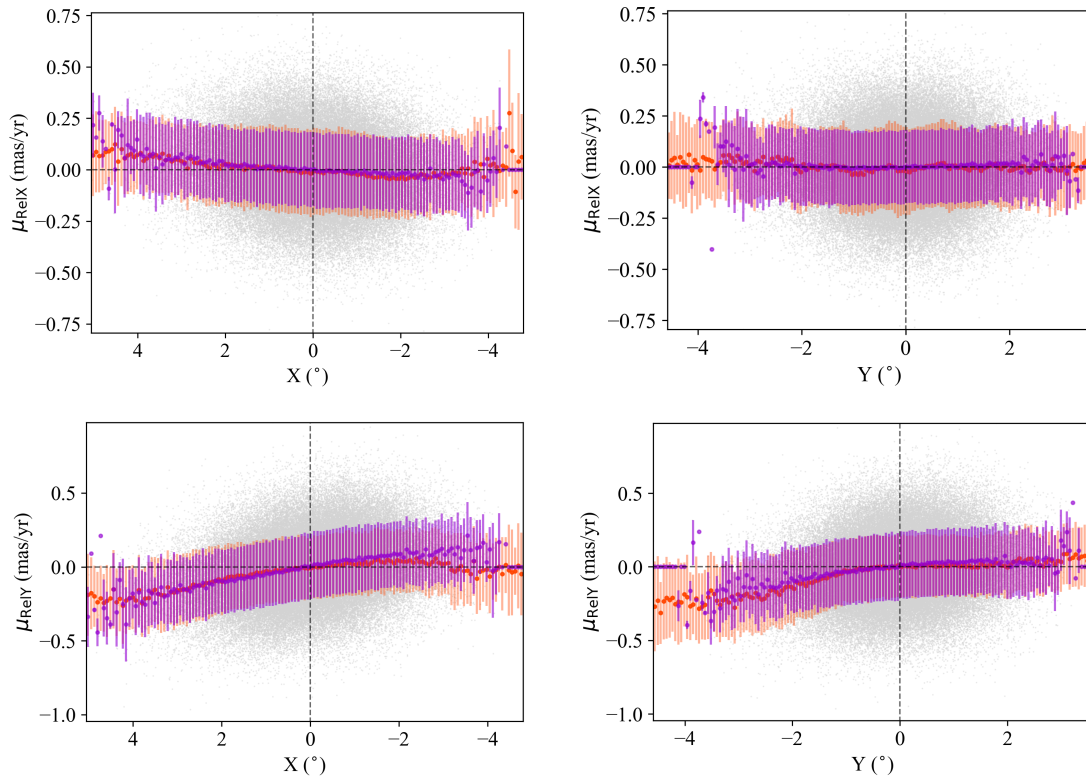


Fig. 4.11.— Residual PMs as a function of spatial position for all permutations of  $PM_X/PM_Y$  and  $X/Y$ . The light grey points are the mock RG stars from the kinematic models. The orange-red points are the measured *Gaia* RG residual PM averages, and the purple points are the averaged residual PMs for the mock RG stars. The model presented here is the best-fit model to the data (specific parameters are listed in Table 4.1).

moving away from us while the stars appear to be moving towards us, relative to the SMC bulk motion. The difference is apparent in more recent stellar RV studies as well (e.g., De Leo et al. 2020), potentially offering new leverage on constraining the most recent interaction between the LMC and SMC.

## 4.5 Conclusions and Discussion

With the release of *Gaia* DR2, the amount of kinematic information available for Magellanic system exponentially expanded. Beyond PM information, expanded spectroscopic surveys of the Magellanic Clouds have added new RV and metallicity information, bringing us closer to a more complete understanding. New combinations of these different parameter spaces will offer the opportunity to constrain the Clouds' interactions and underlying physical properties. To help set the foundation for these more complex models and analyses of the SMC, we have presented a novel approach to disentangling the PMs of the SMC RG population.

Consistent across our models, we find that rotation alone is insufficient to explain the observed PM behavior in the SMC and that invoking tidal expansion of the stars, similar to kinematics observed in stellar streams formed from bodies perturbed by the MW, offers a possible explanation. However, to model this effect, we are required to work with the velocities in true 3D space as the 3D structure of the SMC will drastically affect the implied PM distribution due to the tidal expansion. To achieve this, we combine existing frameworks for transforming 3D velocities for resolved stellar systems into observable quantities and the wealth of distance information from SMC RR Lyrae studies, updating the vdM02 model to include our new tidal component. The result is a model capable of providing a physically intuitive explanation to the otherwise unusual-appearing PM structure of the SMC, one which needs both a

Table 4.1: Rotation Model Parameters.

(1)	Model		Di Teodoro et al. (2019)	Dobbie et al. (2014)	Best-Fit
(2)	Distance $D_0$	kpc	63	60.3	60.6 <sup>a</sup>
(3)	Proper motion $\mu_W$	mas yr <sup>-1</sup>	-0.77	-0.78	-0.67 <sup>b</sup>
(4)	Proper motion $\mu_N$	mas yr <sup>-1</sup>	-1.12	-1.11	-1.20 <sup>b</sup>
(5)	RA $\alpha_0$ (J2000)	deg	15.24	16.25	13.04 <sup>b</sup>
(6)	Dec $\delta_0$ (J2000)	deg	-72.27	-72.42	-73.10 <sup>b</sup>
(7)	Systemic Velocity $V_{\text{sys}}$	km s <sup>-1</sup>	148	148	148 <sup>c</sup>
(8)	Inclination angle $i$	deg	51	60	70
(9)	Position Angle of LON $\Theta^d$	deg	66	122	230
(10)	Rotation Velocity $V_0$	km s <sup>-1</sup>	47	20	20
(11)	Scale Radius $R_0$	kpc	2.8	8.7	1.0
(12)	Precession/Nutation $di/dt$	deg Gyr <sup>-1</sup>	281	140	0.0
(13)	Tidal Scale $V_{\text{tidal}}$	km s <sup>-1</sup> kpc <sup>-1</sup>	0.0	0.0	15

Note. — For Di Teodoro et al. (2019) and Dobbie et al. (2014), all listed values are sourced from the original works.

a. From Jacyszyn-Dobrzeniecka et al. (2017).

b. Measured from the *Gaia* RG data.

c. From Dobbie et al. (2014).

d. Measured east over north.

Table 4.2: Best-Fit Model Values &amp; Uncertainties.

(1)	Model		Best-Fit & Uncertainty
(2)	Distance $D_0$	kpc	60.6 <sup>a</sup>
(3)	Proper motion $\mu_W$	mas yr <sup>-1</sup>	-0.67 <sup>b</sup>
(4)	Proper motion $\mu_N$	mas yr <sup>-1</sup>	-1.20 <sup>b</sup>
(5)	RA $\alpha_0$ (J2000)	deg	13.04 <sup>b</sup>
(6)	Dec $\delta_0$ (J2000)	deg	-73.10 <sup>b</sup>
(7)	Systemic Velocity $V_{\text{sys}}$	km s <sup>-1</sup>	148 <sup>c</sup>
(8)	Inclination angle $i$	deg	70 ± 10
(9)	Position Angle of LON $\Theta^d$	deg	240 ± 30
(10)	Rotation Velocity $V_0$	km s <sup>-1</sup>	19 ± 5
(11)	Scale Radius $R_0$	kpc	1.0
(12)	Precession/Nutation $di/dt$	deg Gyr <sup>-1</sup>	0.0
(13)	Tidal Scale $V_{\text{tidal}}$	km s <sup>-1</sup> kpc <sup>-1</sup>	15 ± 1

Note. — a. From Jacyszyn-Dobrzeniecka et al. (2017).

b. Measured from the *Gaia* RG data.

c. From Dobbie et al. (2014).

d. Measured east over north.

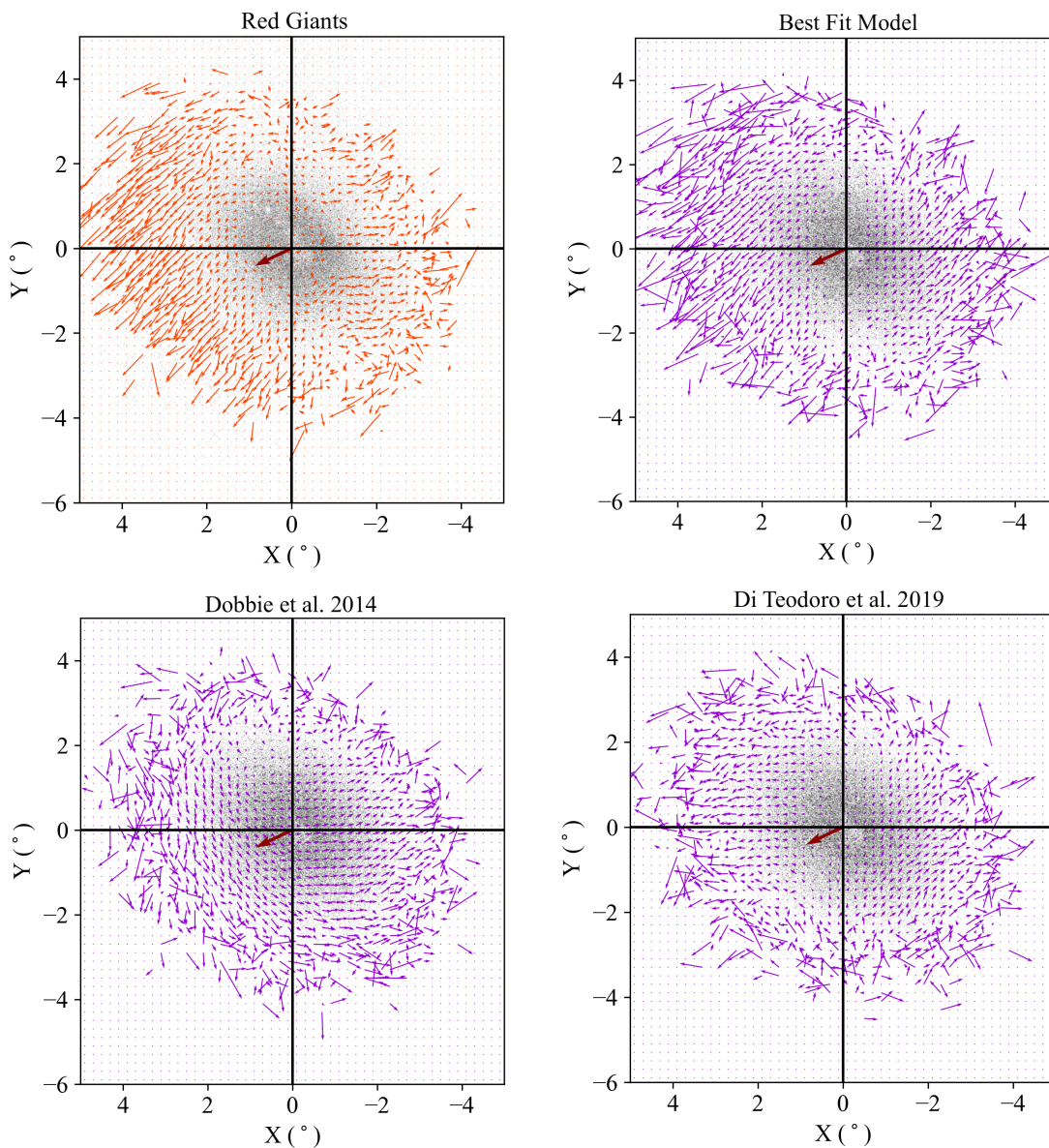


Fig. 4.12.— Residual PM vector plots for the *Gaia* RG stars (orange-red, top left), the best-fit model (top right), the model inferred by D14 (bottom left), and the model inferred by DT19 (bottom right). The frame and vectors are displayed in the same manner as Figure 4.6. The *Gaia*-measured residual PMs have been limited to only the bins that have measured PMs in the mock SMC data. One can readily observe the departures from the *Gaia* data in both the D14 and DT19 models that fail to capture the behavior on the eastern edge of the SMC, while the tidal+rotation best-fit model is able to capture both that structure while also managing to describe the finer interior motions.

coherent rotation and tidal expansion to fully capture the PM behavior.

Using the data-derived systemic properties, our model finds a formal best-fit for a kinematic model with a rotation curve of  $20 \text{ km s}^{-1}$ , a scale radius of 1 kpc, a LON angle of 230 degrees, an inclination angle of 70 degrees, and a tidal scale factor of  $15 \text{ km s}^{-1} \text{ kpc}^{-1}$ . At this magnitude, the rotation is still below the measured RG velocity dispersion ( $\sim 26 \text{ km s}^{-1}$ ), leaving this stellar component as a primarily dispersion-supported system. We do note that our model is still relatively simple and more sophisticated approaches to exploring the full parameter space will be required in the future. As the tidal expansion and rotation plane, especially one inclined into the plane of the sky, offer potential degeneracies without full 3D motions, we look towards future RV surveys, potentially in upcoming *Gaia* data releases or other ground-based efforts, to better constrain our modeling, which may impact the inferred rotation and tidal expansion magnitudes.

The combination of the existence of coherent stellar rotation and a clear offset in the systemic RG properties (center, bulk PM) from previously measured studies with a mixed stellar sample suggests a reassessment of how we understand the SMC. To this, we propose a new interpretation similar to the Bullet Cluster, where in the last interaction with the LMC, the SMC gas was slowed and pulled towards the LMC, while the RG stars passed through collision-free, kinematically separating from the newly forming stars. Moving forward, we underscore the necessity of identifying distinct SMC subpopulations and treating their kinematics separately. In turn, by unlocking the kinematics from each other, we may create a finer leverage on constraining the LMC-SMC interaction than simply treating all of the stars as a single body. Future work will be necessary to disentangle the kinematics of these other stellar populations, folding in new kinematic components capable of addressing

younger stars forming from turbulent gas.

This work has made use of data from the European Space Agency (ESA) mission *Gaia* (<https://www.cosmos.esa.int/gaia>), processed by the *Gaia* Data Processing and Analysis Consortium (DPAC, <https://www.cosmos.esa.int/web/gaia/dpac/consortium>). Funding for the DPAC has been provided by national institutions, in particular the institutions participating in the *Gaia* Multilateral Agreement.

Funding for the Sloan Digital Sky Survey IV has been provided by the Alfred P. Sloan Foundation, the U.S. Department of Energy Office of Science, and the Participating Institutions. SDSS acknowledges support and resources from the Center for High-Performance Computing at the University of Utah. The SDSS web site is [www.sdss.org](http://www.sdss.org).

SDSS is managed by the Astrophysical Research Consortium for the Participating Institutions of the SDSS Collaboration including the Brazilian Participation Group, the Carnegie Institution for Science, Carnegie Mellon University, the Chilean Participation Group, the French Participation Group, Harvard-Smithsonian Center for Astrophysics, Instituto de Astrofísica de Canarias, The Johns Hopkins University, Kavli Institute for the Physics and Mathematics of the Universe (IPMU) / University of Tokyo, the Korean Participation Group, Lawrence Berkeley National Laboratory, Leibniz Institut für Astrophysik Potsdam (AIP), Max-Planck-Institut für Astronomie (MPIA Heidelberg), Max-Planck-Institut für Astrophysik (MPA Garching), Max-Planck-Institut für Extraterrestrische Physik (MPE), National Astronomical Observatories of China, New Mexico State University, New York University, University of Notre Dame, Observatório Nacional / MCTI, The Ohio State University, Pennsylvania State University, Shanghai Astronomical Observatory, United Kingdom Participation Group, Universidad Nacional Autónoma de México, University of Ari-

zona, University of Colorado Boulder, University of Oxford, University of Portsmouth, University of Utah, University of Virginia, University of Washington, University of Wisconsin, Vanderbilt University, and Yale University.

## Chapter 5

# Exploring the Kinematics of the “Young” Stars of the Small Magellanic Cloud

The following text is in preparation for an upcoming manuscript and has been lightly edited for this format.

### **Summary**

We present a new analysis of the kinematics, internal and systemic, of the red supergiants (RSGs) in the Small Magellanic Cloud. We identify an astrometrically well-behaved sequence of RSGs, consistent with ages on the order of  $\sim 150$  Myr, and cross-match with existing publicly available radial velocity (RV) catalogs to create a subset of stars with near-3D velocities. To constrain the internal kinematics of the SMC RSGs, we apply our previously established framework, which had been used to analyze the SMC RG population. We find an apparent bimodality in the RSG population kinematics, with one population well-described by RG systemic properties and the other with a clear offset. Near the inferred RG center, we find evidence for

coherent rotation in the proper motions (PMs) of the RSG population, while stars over a degree from the RG center display no apparent signs of rotation. This offset extends to the RV sample as well, with the southeastern RSGs having a noticeably larger residual RV than the stars near the RG center. We suggest this may offer a clear way to assess the fraction of the SMC that stayed gravitationally bound during its interactions with the LMC, which in turn may help to better constrain our understanding of the LMC-SMC history.

## 5.1 Introduction

Located near the Milky Way (MW) are the Large and Small Magellanic Clouds (LMC and SMC, respectively), a pair of irregular dwarf galaxies. At a distance of 50 and 60 kpc, they represent the closest example of an interacting pair of galaxies, offering an unparalleled opportunity to study in high resolution this complex process occurring across the universe. Originally thought to have orbited the MW multiple times, the first precision proper motion (PM) measurement of the LMC and SMC motions revealed that they were likely on their first infall into the MW (Kallivayalil et al. 2006b; Besla et al. 2007). This new result upended our previous understanding of the system and quickly became the new foundational paradigm of the system.

Since then, significant effort has been placed in understanding not just the systemic properties of the two galaxies but the internal kinematics as well. The LMC, which had been known to display signs of coherent rotation from early radial velocity (RV) studies (van der Marel et al. 2002), proved tractable in understanding the PM distribution as well. Using *HST*, van der Marel & Kallivayalil (2014) was able to demonstrate the clear existence of rotation in the LMC and used the prior RV measurements to constrain its magnitude of rotation and the corresponding geometry.

However, the SMC has not as readily revealed its kinematic details. A number of different RV-based studies attempted to constrain the internal motions, using a variety of different tracer populations. Stanimirović et al. (2004), using H I gas, found evidence for coherent rotation in the gas and measured a dynamical center located near the northeast part of the SMC. Dobbie et al. (2014) examined a large population of red giant (RG) stars in the SMC and detected a possible rotation signal, albeit at nearly an orthogonal angle to the rotation geometry from the H I. Using PMs to constrain the rotation has not proven effective either. A combination of *HST* observations and SMC stars identified in the Tycho-*Gaia* Astrometric Solution (Lindgren et al. 2016; van der Marel & Sahlmann 2016) was inconclusive in attempting to measure rotation, though potential signs of outward tidal motion were detected in the southeast portion of the SMC (Zivick et al. 2018).

With the advent of the *Gaia* Data Release 2 (Gaia Collaboration et al. 2018b), suddenly there were tens of thousands of stars in the SMC with well-measured PMs. Still, initial efforts did not reveal any significant rotation (Gaia Collaboration et al. 2018c). However, new kinematic modeling techniques have revealed possible signs of rotation in the old RG population of the SMC. Zivick et al. (in prep.) (hereafter Z20) demonstrates that if one attempts to account for the impact on the internal kinematics due to tidal expansion in the SMC, a coherent rotation signal can be seen extending for multiple degrees from the center of the SMC. Crucially, this relies on an appropriate assumption of the systemic properties of the SMC RG population, which appears to be significantly offset in both position and PM from previously derived properties using either gas or a mix of stellar tracers.

With a framework in place capable of identifying coherent internal kinematics, the next stellar component of the SMC to examine is the intermediate age stars. Ripepi

et al. (2017) examined the Classical Cepheid population of the SMC, finding that there appeared to be a bimodality in the ages of the Cepheids, with an older group near 220 Myr in age and a younger group closer to 120 Myr. Additionally they identify an elongation along the line of sight in the Cepheids, stretching from  $\sim 55$  kpc in the northeast section of the SMC to greater than 72 kpc in the southwest section of the SMC. The timing of the stars correlates well with the inferred time of last interaction between the LMC and SMC, somewhere around 150 Myr ago (Zivick et al. 2018). As such, this intermediate population of stars may contain unique kinematic signatures that can place strong constraints on the interaction process.

In this chapter, we present our efforts to understand the kinematic nature of the RSG population in the SMC. In Section 5.2 we describe our selection of the *Gaia* DR2 data, using both astrometric quality cuts and SMC membership requirements, and the process we apply in cross-matching with publicly available RV catalogs. In Section 5.3 we present our efforts in understanding the systemic properties of the RSGs and the corresponding internal kinematic analysis under select systemic property assumptions. Additionally, we present the results of the RV catalog and compare/contrast with the prior RG results from Z20. Finally, we place our results in the broader context of understanding the SMC, identify new possible constraints on SMC-LMC properties, and outline future paths forward to improve our analysis.

## 5.2 Data Selection

### 5.2.1 Gaia DR2 Selection

For our analysis, we select all stars from the *Gaia* DR2 catalog within roughly 5 degrees from the optical center of the SMC using `pygacs`<sup>1</sup>. We then apply a series of initial cuts to jointly select both astrometrically well-behaved stars and stars likely to belong to the SMC. To remove MW foreground stars, we require all stars in our sample to have a parallax  $< 0.2$  mas and a proper motion within  $3 \text{ mas yr}^{-1}$  of the SMC systemic motion ( $\mu_W = -0.82 \pm 0.1 \text{ mas yr}^{-1}$  and  $\mu_N = -1.21 \pm 0.03 \text{ mas yr}^{-1}$  from Zivick et al. (2018)).

Next we apply the following cut to the renormalized unit weight error (RUWE) as described in the *Gaia* technical note GAIA-C3-TN-LU-LL-124-01:

$$\frac{\sqrt{\chi^2/(N-5)}}{u_0(G, C)} < 1.40, \quad (5.1)$$

which uses the following *Gaia* properties:

$$\begin{aligned} N &\equiv \text{astrometric\_n\_good\_obs\_al}, \\ \chi^2 &\equiv \text{astrometric\_chi2\_al}, \\ u_0 &\equiv \text{Normalization factor } (G, C), \\ G &\equiv \text{phot\_g\_mean\_mag}, \\ C &\equiv \text{bp\_rp}. \end{aligned} \quad (5.2)$$

. We additionally apply a cut for the color excess of the stars, as described in Gaia Collaboration et al. (2018a) Equation C.2. As we are concerned with astrometrically

---

<sup>1</sup><https://github.com/Johannes-Sahlmann/pygacs>

well-behaved stars, primarily the bright stars, and to provide another check to avoid MW contamination, we select stars brighter than  $G < 18$ , leading to the final source densities in the top left panel of Figure 5.1. We note the conspicuous absence of 47 Tuc in the panel as an example of the power of *Gaia* DR2 to remove potential contamination from spatially coincident sources.

With this initial astrometric selection, we move to further isolate the SMC stars. Examining the color-magnitude diagram (CMD) in Figure 5.2, we identify three clear SMC stellar tracks in our sample: the main sequence (MS, marked in blue), the red giants (RG, red), and the sample of interest in this effort, the red supergiants (RSG, green) whose CMD structure correlates well with ages near 150 Myr, similar to the Cepheid population in Ripepi et al. (2017). We do note that the SMC red clump is observable near the bottom of the CMD, but due to worsening astrometric performance at  $G > 18$ , and a desire to focus on more intermediate-age populations, we do not examine it further in this work. In addition, all sources that have been successfully cross-matched with publicly available RV catalogs are marked by dark blue points (this process and catalogs are discussed further in Section 5.2.2). Here we note that while a majority of the RV-matched sources are primarily the RG population (of the 100,000+ RGs,  $\sim 4,200$  have RVs), a sizeable fraction belongs to the RSG sequence ( $\sim 9,000$  RSGs with just over 600 RVs).

Finally as a reference and to understand how the selections translate between the different parameter spaces, we display the spatial positions of the three different CMD sequences in Figure 5.1. The derived H I center (Di Teodoro et al. 2019) is displayed as a blue square in the panel displaying all stars passing the initial astrometric quality checks and appears as a black square in the remaining three panels. Similarly, the derived RG center from Zivick et al. (in prep.) is marked by the red “x” at the (0,0)

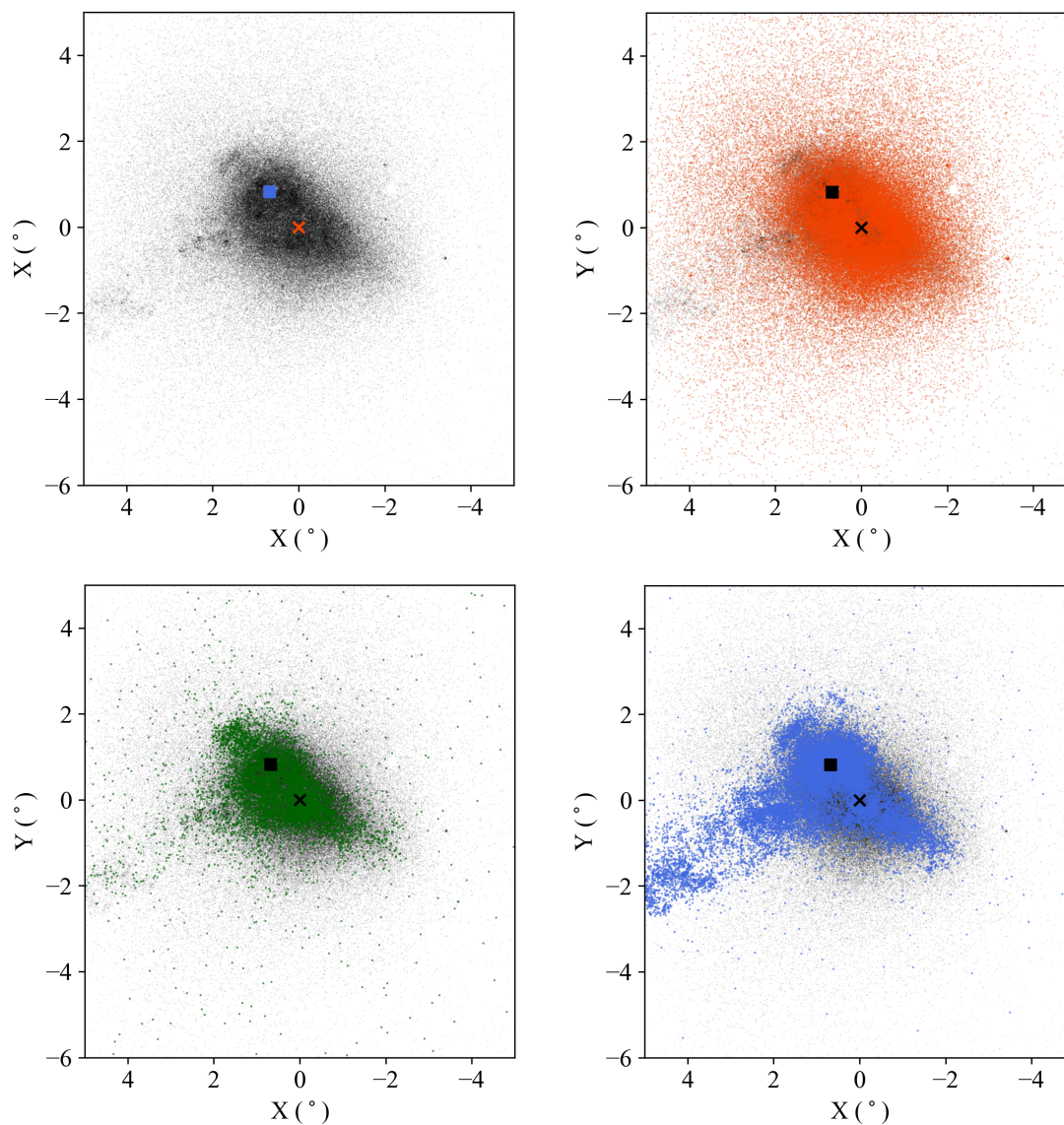


Fig. 5.1.— *Gaia* DR2 sources after initial astrometric cuts have been applied to the data, displayed in a Cartesian coordinate system as outlined in Gaia Collaboration et al. (2018c). For each plot, the zero point is set to the best-fit center for the RG population found in Z20 (the “x”, red in top left), and the inferred kinematic center from H I gas is marked by the square (blue in top left). **(top left)** All stars in the *Gaia* sample are displayed. The SMC Wing can be seen on the eastern (left) side of the SMC, heading towards the Magellanic Bridge and the LMC. We also note the empty patch on the right side of the figure as the location of 47 Tuc, which has been removed from our sample by our astrometric criteria. **(top right)** The red giant population as identified in Figure 5.2. **(bottom left)** The red supergiant population. **(bottom right)** The main sequence population.

location in the top left panel and as a black “x” in the remaining three plots. We can see as we transition from older to younger populations that the preferred center shifts. Interestingly, the RSG population appears to be plausibly-fit by both centers, reflecting its intermediate age situated between the RGs and MS and its formation around the last LMC-SMC interaction. With the basic characteristics of our target population, the RSGs, established, we can move to begin a more thorough analysis of their properties.

### 5.2.2 Radial Velocity Cross-Matching

To attempt to provide full 3D velocity information for our selected stars, we look to cross-match our catalog with existing RV catalogs. For this we use two publicly available catalogs: the prior work by D14 and RVs from the Apache Point Observatory Galactic Evolution Experiment 2 (APOGEE-2) (Majewski et al. 2017; Wilson et al. 2019), part of the Sloan Digital Sky Survey IV (Blanton et al. 2017) Data Release 16 (Ahumada et al. 2019). Between the two catalogs, excluding any sources that may have been double counted, we find just over 600 sources common to our DR2 RSG selection, which primarily trace the central distribution of the RSG stars seen in the lower left panel of Figure 5.1.

As the overall fraction of RSG stars with PMs+RVs is larger than the fraction for the RGs, we do weigh the RV information more heavily than in prior analyses. While we do not know the exact distance to each of the stars, making it difficult to translate the PMs into physical velocities, we note that for the purposes of comparing the PMs to the RVs at the average SMC distance of 60 kpc, a PM of  $0.1 \text{ mas yr}^{-1}$  corresponds to  $\sim 30 \text{ km s}^{-1}$ .

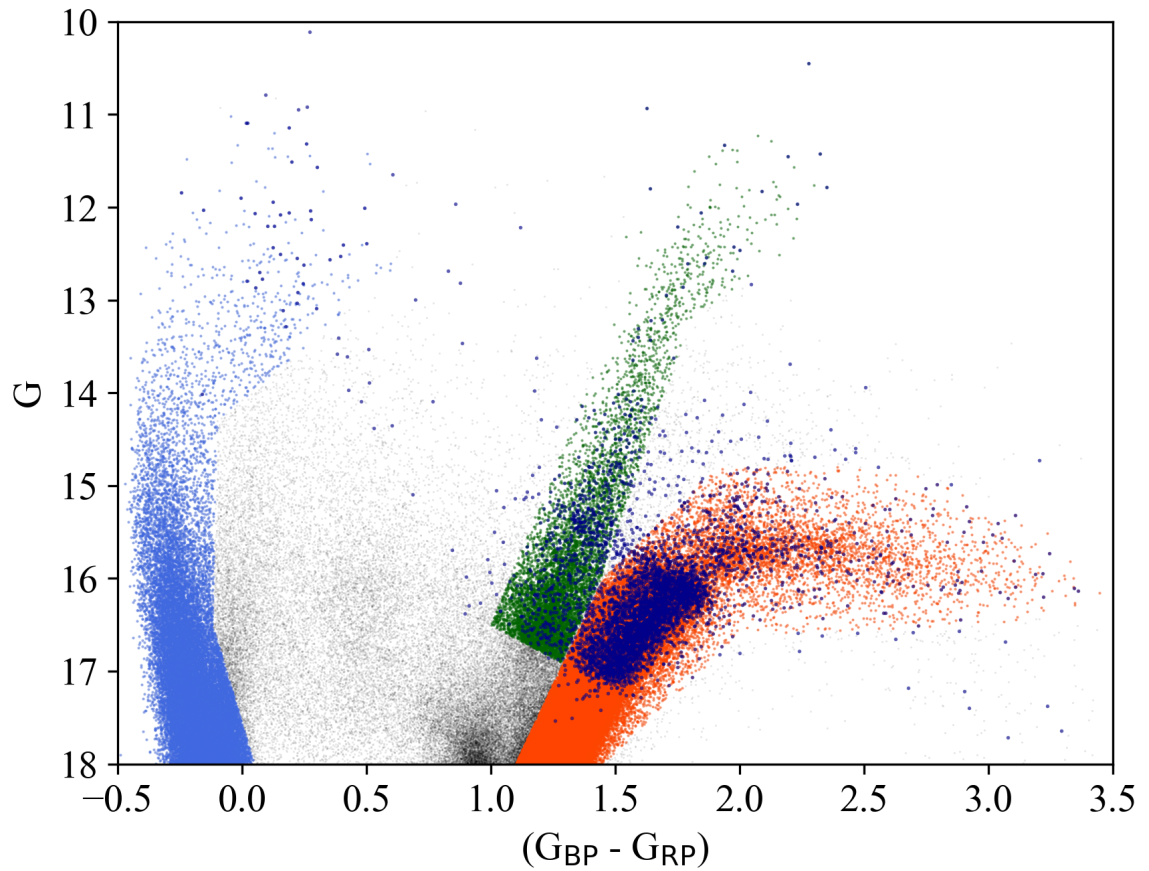


Fig. 5.2.— Color-Magnitude Diagram of all sources present in the top left panel of Figure 5.1. Three separate stellar sequences have been marked: the main sequence (MS) stars in light blue on the left side, the red supergiants (RSG) in green near the center, and the red giants (RG) on the right side. All sources that have been matched to an existing RV measurement (described in Section 5.2.2) are marked in dark blue, which can be seen to mostly sample the RGs but do extend into the RSGs.

## 5.3 Data Analysis

### 5.3.1 Systemic Properties

To better understand the distribution of the RSGs and suitability of different fitting techniques to determine systemic properties, we begin by creating simple binned plots of the RSG positions and PMs (Figures 5.3 and 5.4, respectively). For the positions, we see there appears to be a clear overdensity located in the southwest area of the SMC, while the rest of the area appears to be more uniform in density. When the the H I and RG kinematic centers for previous models of the SMC are overplotted on the spatial density, we see that the RG center appears to agree well with the largest spatial overdensity (for exact values for the RG and H I models, refer to Table 5.1). Similarly, the binned distribution of the RSG PMs has a clear central overdensity with an asymmetric halo of stars around it. When the systemic PMs are overplotted, once again we see that the RG center appears to agree well with the central overdensity, while attempting a 2D Gaussian fit of the data (the green diamond in Figure 5.4) results in a center, that while representative of the total distribution, does not capture the center of the overdensity.

As a brief aside on the PMs, as we will be using the framework for analyzing PMs for an extended body on the sky from van der Marel et al. (2002), to keep consistent with the notation, from here we will refer to  $\mu_{\alpha} \cos \delta$  and  $\mu_{\delta}$  as  $\mu_E$  and  $\mu_N$  respectively.

Beyond utilizing the systemic properties to learn more about the Magellanic system, assumptions for the kinematic center and bulk PM are crucial in properly correcting for the viewing perspective. As the SMC is a large, resolved 3D structure on the night sky, the bulk PM vector that is subtracted from each star to shift to a relative SMC frame must be modified to account for changes in the decomposition of

the SMC 3D velocity into observed quantities. Correspondingly, misidentifying either the kinematic center or systemic PM can lead to misinterpretations of the internal kinematics. As the RG center and PM both appear to agree with the notable spatial and kinematic overdensities, we choose to use these properties when we move to examining the internal kinematics of the SMC RSGs.

### 5.3.2 Internal Kinematics

With the systemic properties determined, we subtract the systemic PM from the individual stellar motions, correcting for viewing perspective. The resulting relative PM plot for the RSGs can be seen in the left panel of Figure 5.5. Immediately we observe, similar to previous studies of SMC *Gaia* PMs, that there is a large outward motion towards the southeast, in the direction of the Magellanic Bridge and consistent with the direction of relative motion between the LMC and SMC. This relative LMC-SMC motion has been calculated using the assumed RG values as well (as shifts to the kinematic center/PM could in turn impact the direction and magnitude of the relative velocity).

However, the inner 1-2 degrees of the SMC reveals an unexpected kinematic behavior: apparent rotation in the central 1 degree. In Figure 5.6, this apparent rotation is clear, though the exact geometry and magnitude of the rotation cannot be immediately discerned. This rotation quickly disappears as one moves past 0.5 kpc in radius from the assumed RG center. The northeast section in particular presents an interesting challenge in understanding how the kinematics appear to shift so dramatically over such a short range.

Given that the motion appears to be consistent with the relative LMC-SMC velocity, attributing the largely linear motion to a tidal expansion-related mechanism

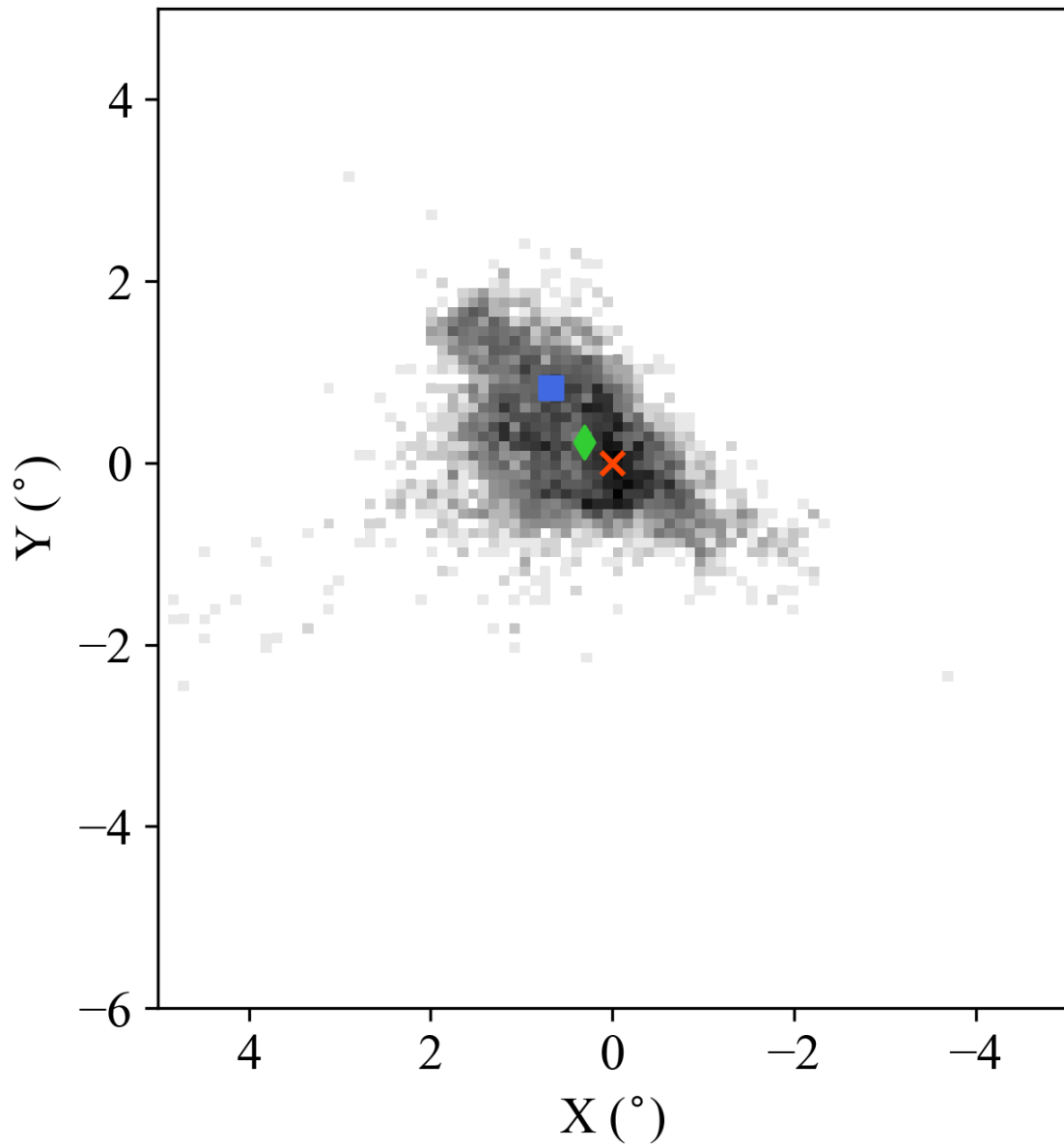


Fig. 5.3.— Binned spatial distribution of the SMC RSG population. The H I and RG centers (blue square and red “x”) from Figure 5.1 are displayed for reference along with the center from a 2D Gaussian fit to the RSG data (green diamond).

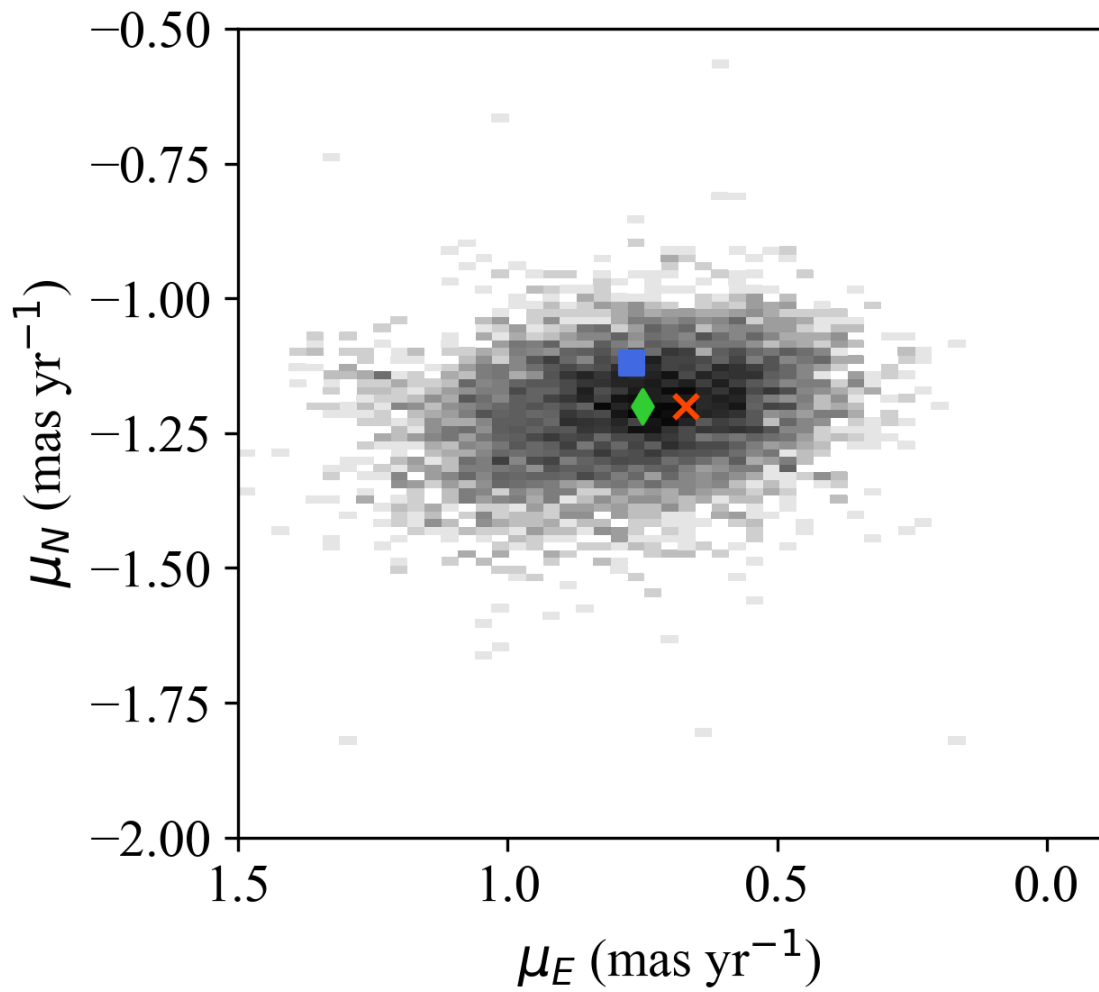


Fig. 5.4.— Binned PM distribution of the SMC RSG population. The systemic PM for the RGs is marked by the red “x”, the systemic PM assumed for H I models is marked by the blue square, and the mean location from a 2D Gaussian fit to the RSG PM data (green diamond).

would appear reasonable. In Z20, we examined applying this linear expansion to the RG population, finding that a combination of tidal expansion and rotation was required to examine the signals in the PM data. The formal best-fit model for the RGs can be seen in the right panel of Figure 5.5 for reference. In this Figure, much of the motion on the eastern side of the modeled SMC is attributable to the tidal expansion. However, for this model, we used a linear tidal expansion, where the magnitude of the motion increases as a function of distance from the assumed kinematic center of the SMC. As a result, even out to 2 degrees from the center, the contribution from the tidal expansion is still relatively minimal.

When we compare this to the residual RSG PMs in the same region though, we find the RSG residuals to be significantly larger than the RG residuals, beginning roughly 0.5 degrees from the center. To quantify this behavior, we adopt a similar spatial-kinematic set of distributions as in Z20, using the RG geometry to assign a new  $X/Y$  frame, as marked by the dashed black line in the left panel of Figure 5.5. The RSG stars are binned with widths calculated using the Freedom-Draconis Rule (Freedman & Diaconis 1981), to avoid potentially overfitting the data. The simple average in each bin is calculated and the associated standard deviation is displayed as the error bar.

The resulting residual PMs in  $X$  and  $Y$  as a function of spatial position in  $X$  and  $Y$  can be seen in Figure 5.7. Along the  $Y$ -axis, the RSGs are relatively tightly clustered, making it difficult to discern any distinct kinematic subgroups. As expected, as one moves negative in  $Y$  spatially, closer towards the Magellanic Bridge, the residual PM in  $Y$  grows larger and larger.

However, in the  $X$  direction, two different kinematic groups appear to exist. One appears to be located near the center of the SMC, and the second appears to start

about 0.5 degrees from the center. The outer group also appears to have a flat offset in PM, as opposed to a smoother transition that would be consistent with a single kinematic group. This picture is in keeping with the original insight gleaned from the averaged residual vector plot. However, the staggered appearance of the spatial-kinematic plots suggests that attempting to fit the entire RSG population as a single kinematic system would be insufficient to properly constrain the internal kinematics.

### 5.3.3 Radial Velocity Structure

With the hints of distinct kinematic populations in the SMC RSGs present in the PMs, we turn to the RVs to further investigate. Similar to the PMs, we subtract the systemic SMC RG RV (listed in Table 4.1) and correct for viewing perspective effects to create residual RVs for analysis. The resulting residual RVs are displayed in Figure 5.8, with the spatial location of each star with a matched RV marked and the color of the star corresponding to the residual RV. Immediately we see that there appears to be a clearly offset group of RSG stars, by nearly 40-50 km s<sup>-1</sup> from the systemic RV, in a direction opposite from the observer.

In contrast, most of the stars located within the inner 0.5 degrees that possess the apparent rotation seem to have a relatively small residual RV. To the southwest, an equally discrepant population appears, moving towards the observer at nearly 40-50 km s<sup>-1</sup>. To the northeast, where the large PM offset originally appeared, the residual RVs do not appear to have a coherent behavior to them, with many of them lying near 0 km s<sup>-1</sup>.

For comparison, the full PM+RV sample from Z20 appears in the right panel of Figure 5.8. Here, despite including more than five times as many sources, no such obvious offset in RVs occurs as with the RSGs. In turn this suggests that there may a

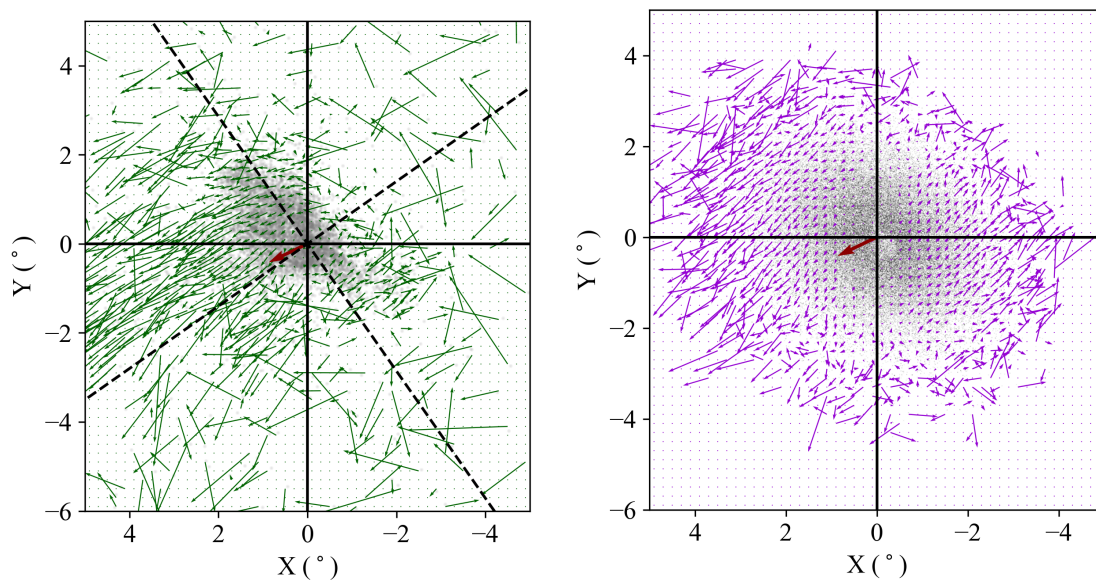


Fig. 5.5.— Averaged residual PM vectors in a Cartesian coordinate system, every 0.2 degrees for easier display of the kinematic behavior. The dark red vector indicates the direction of relative LMC-SMC motion, assuming the RG systemic PM from Z20. For both plots, the assumed kinematic center and systemic PM are the same, and the solid black line provides a guide for the eye for the  $x$ - and  $y$ -axes. **(Left)** RSG *Gaia* PM vectors are marked in green. The dashed black line indicates the rotated coordinate system used for the spatial-kinematic quantification, as described in Section 5.3.2. **(Right)** Residual PM vectors (in purple) for the best-fit kinematic model to the SMC RG population from Z20 as a demonstration of the capabilities and limitations of the current modeling.

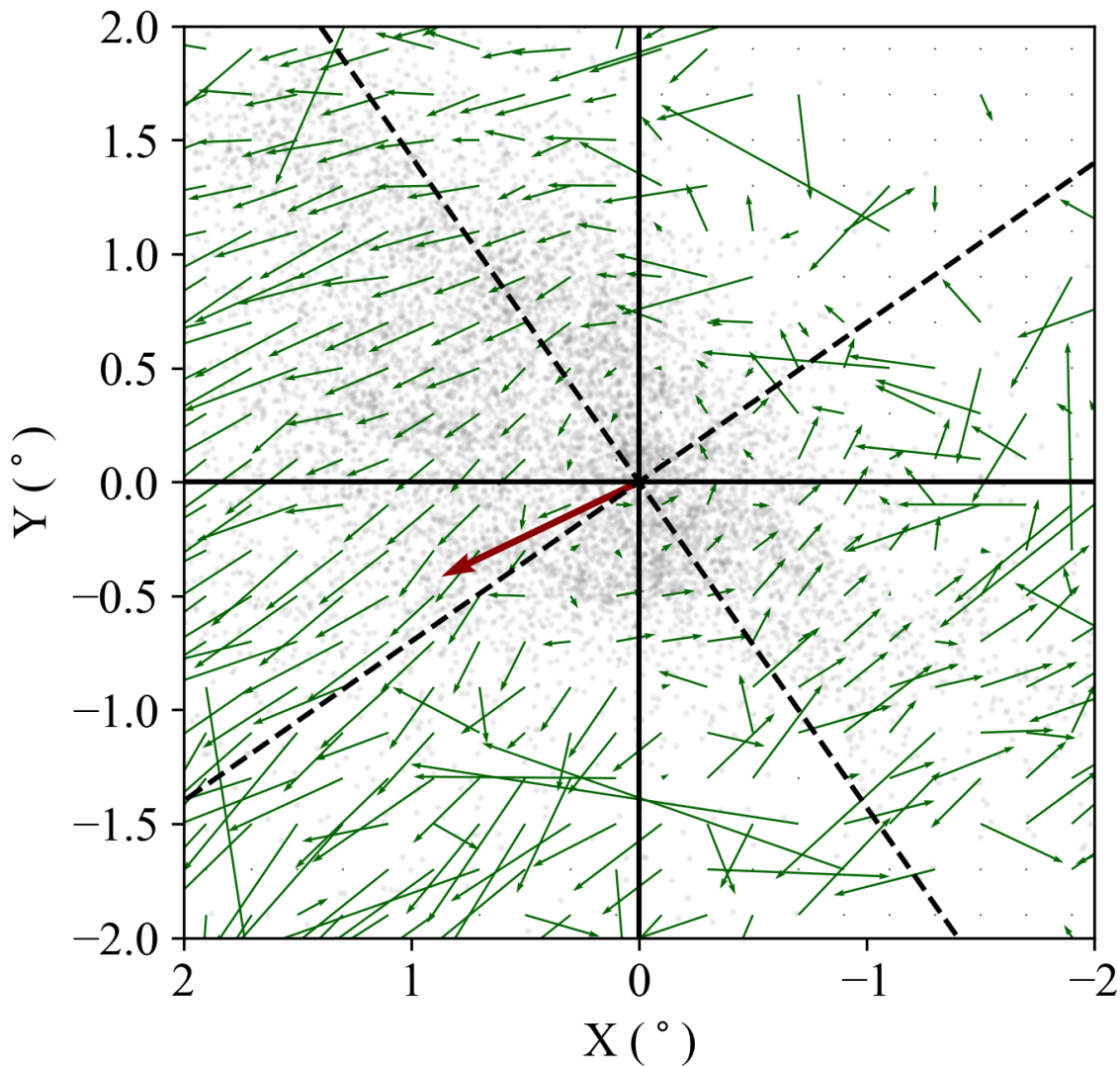


Fig. 5.6.— Averaged residual PM vectors in the same Cartesian frame as displayed in Figure 5.5. To gain a clearer insight into the central internal kinematic of the SMC RSGs, the field of view has been shrunk to only encompass the inner 4 degrees. The relative LMC-SMC vector and dashed black lines are the same as the previous Figure.

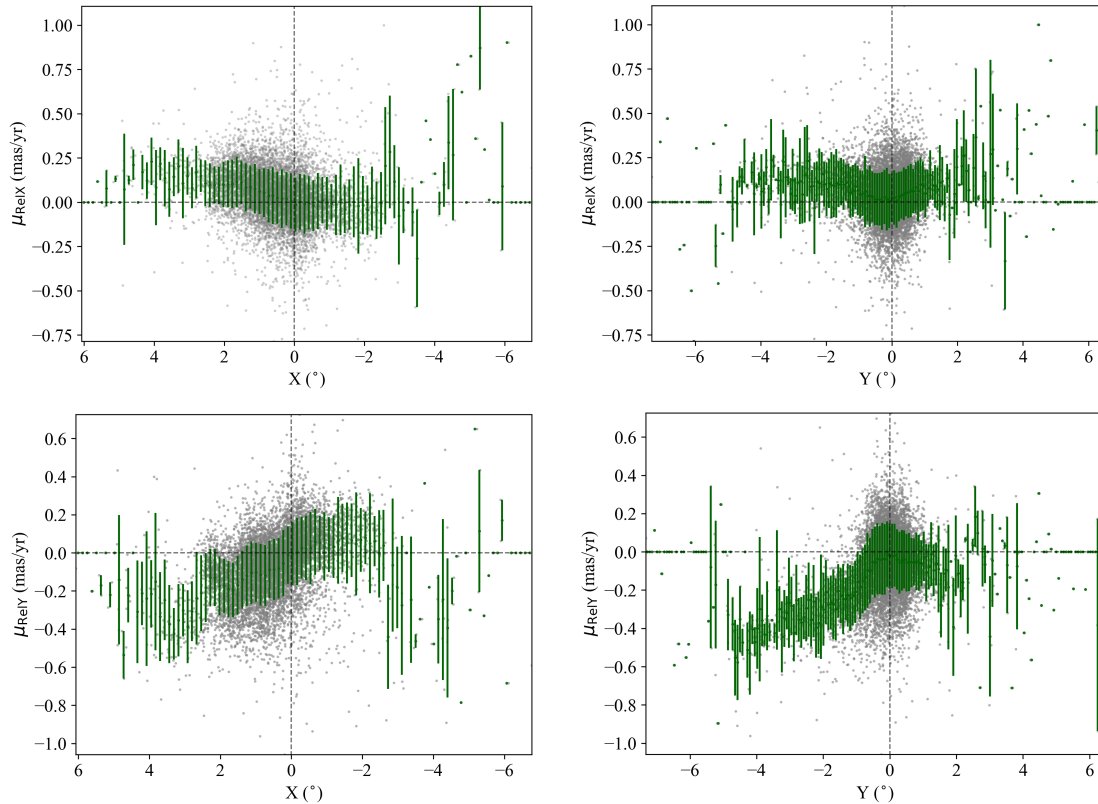


Fig. 5.7.— Residual PMs plotted against spatial position in the SMC RG geometric major/minor axis frame. The gray points are all of the RSG stars in the same. The stars are binned accordingly to the spatial sampling, which is about 0.13 degrees in X and 0.07 degrees in Y. A simple average is taken for each bin, marked by the green point, and the standard deviation of the bin is shown as the error bar. **(Top Left)** Residual PM in X (which spans the major axis of the SMC, with the positive X direction north of the Magellanic Bridge) as a function of position in X. **(Top Right)** Residual PM in X as a function of spatial position in Y (which is roughly along the axis of the relative LMC-SMC motion). **(Bottom Left)** Residual PM in Y as a function of spatial position in X. **(Bottom Right)** Residual PM in Y as a function of position in Y.

unique mechanism that has led to these two concentrated outflow points in the RSG population. However, the exact statistical significance of these small areas remains uncertain and will require future work, both in observations and modeling, to better characterize this.

## 5.4 Implications and Future Work

Here we have demonstrated the potential existence of coherent rotation in the RSG. This rotation appears when RG systemic properties (the kinematic center, PM, distance, and RV) are used in calculating the viewing perspective corrections. In order to quantify the statistical significance of this rotation, more sophisticated techniques will be required, as each individual kinematic group should require a unique set of systemic properties for accurate analysis.

This may prove especially important for the SMC RSG population as the kinematic evidence suggests that there may be at least two distinct populations. As seen in the decomposed  $X/Y$  frame, there appears to be a fixed offset among groups of stars with a spatial dependence. Complicating the picture, there appear to be two coherent streams of residual RVs in the RSG populations, one moving away from the observer in the eastern part of the SMC and one moving towards the observer in the southwest portion of the SMC. Intriguingly, or perhaps reassuringly, these two areas also correspond to the bounds of the line-of-sight depth identified in the Cepheid populations (Ripepi et al. 2017). Taken together with age and other non-kinematic information, it may be possible to properly identify multiple distinct populations (e.g., pre-interaction stream formation/post-interaction formation) using this higher dimension parameter space.

The existence of the coherent rotation may also shed insight on the larger struc-

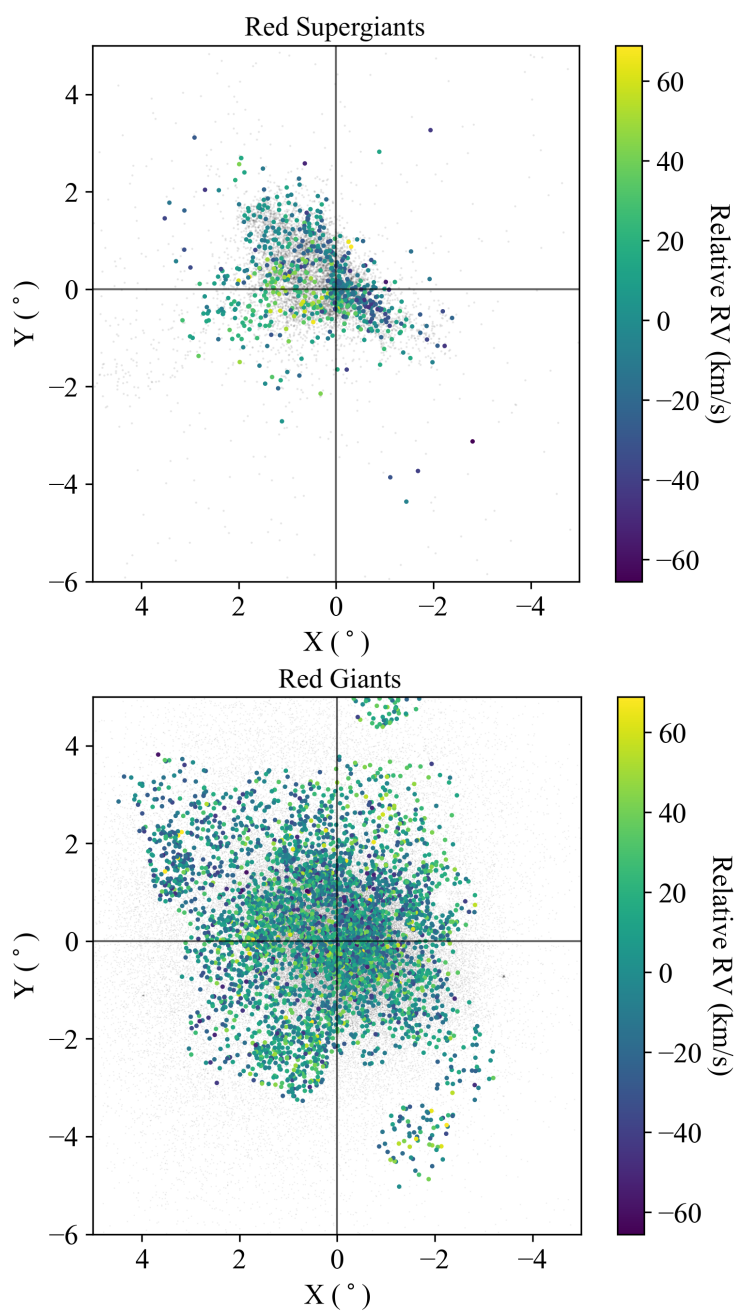


Fig. 5.8.— Spatial positions of the *Gaia* sample with cross-matched RVs, color coded by the residual RV (after removing the SMC systemic RV and correcting for viewing perspective). The non-RV stars for each respectively stellar population are marked by the grey points in the background. **(Left)** All RSGs with residual RVs. **(Right)** All RGs with residual RVs.

ture and interaction between the LMC and SMC. As the rotation appears to have a significant magnitude in the plane of the sky with relatively minimal scatter in RV, we hypothesize that the gas that formed the stars may have remained completely bound to the SMC throughout the interaction process, setting a hard limit on the tidal radius for the SMC. With potential improvements to the interaction scenario from other kinematic populations (e.g., the RGs), this constraint on the tidal radius may in turn place a new constraint on the mass of the SMC, a difficult challenge given the complexity of the overall system.

Moving forward, future work to improve this understanding will rely on a few different areas. Continued RV measurements for the SMC, across all stellar populations, will allow us to further limit potential degeneracies between different geometric models. In particular, RVs measured for the already-identified Cepheid population would place us as close as possible to having true 6D phase space information, a powerful tool to have in comparing to numerical simulations. With the improvements in constraining the stellar systemic properties, updated simulations that factor in these improvements will be crucial for continuing to develop our intuition for this interaction. And finally, future data releases from the *Gaia* mission will continue to shrink the individual errors for stellar PMs, slowly bringing into focus what was once thought to be an intractable kinematic environment.

This work has made use of data from the European Space Agency (ESA) mission *Gaia* (<https://www.cosmos.esa.int/gaia>), processed by the *Gaia* Data Processing and Analysis Consortium (DPAC, <https://www.cosmos.esa.int/web/gaia/dpac/consortium>). Funding for the DPAC has been provided by national institutions, in particular the institutions participating in the *Gaia* Multilateral Agreement.

Funding for the Sloan Digital Sky Survey IV has been provided by the Alfred P.

Sloan Foundation, the U.S. Department of Energy Office of Science, and the Participating Institutions. SDSS acknowledges support and resources from the Center for High-Performance Computing at the University of Utah. The SDSS web site is [www.sdss.org](http://www.sdss.org).

SDSS is managed by the Astrophysical Research Consortium for the Participating Institutions of the SDSS Collaboration including the Brazilian Participation Group, the Carnegie Institution for Science, Carnegie Mellon University, the Chilean Participation Group, the French Participation Group, Harvard-Smithsonian Center for Astrophysics, Instituto de Astrofísica de Canarias, The Johns Hopkins University, Kavli Institute for the Physics and Mathematics of the Universe (IPMU) / University of Tokyo, the Korean Participation Group, Lawrence Berkeley National Laboratory, Leibniz Institut für Astrophysik Potsdam (AIP), Max-Planck-Institut für Astronomie (MPIA Heidelberg), Max-Planck-Institut für Astrophysik (MPA Garching), Max-Planck-Institut für Extraterrestrische Physik (MPE), National Astronomical Observatories of China, New Mexico State University, New York University, University of Notre Dame, Observatório Nacional / MCTI, The Ohio State University, Pennsylvania State University, Shanghai Astronomical Observatory, United Kingdom Participation Group, Universidad Nacional Autónoma de México, University of Arizona, University of Colorado Boulder, University of Oxford, University of Portsmouth, University of Utah, University of Virginia, University of Washington, University of Wisconsin, Vanderbilt University, and Yale University.

Table 5.1: SMC Systemic Model Properties.

(1)	Model		Di Teodoro et al. (2019)	Z20
(2)	Distance $D_0$	kpc	63	60.6 <sup>a</sup>
(3)	Proper motion $\mu_W$	mas yr <sup>-1</sup>	-0.77	-0.67 <sup>b</sup>
(4)	Proper motion $\mu_N$	mas yr <sup>-1</sup>	-1.12	-1.20 <sup>b</sup>
(5)	RA $\alpha_0$ (J2000)	deg	15.24	13.04 <sup>b</sup>
(6)	Dec $\delta_0$ (J2000)	deg	-72.27	-73.10 <sup>b</sup>
(7)	Systemic Velocity $V_{\text{sys}}$	km s <sup>-1</sup>	148	148 <sup>c</sup>

Note. — For Di Teodoro et al. (2019) and Dobbie et al. (2014), all listed values are sourced from the original works.

a. From Jacyszyn-Dobrzeniecka et al. (2017).

b. Measured from the *Gaia* RG data.

c. From Dobbie et al. (2014).

# Chapter 6

## Summary

### 6.1 Satellites in a New Age of Astrometry

The evolution of our understanding of the SMC kinematics mirrors that of Local Group astrometry. A decade ago, we were limited to intensive observing campaigns with *HST* measuring PMs over a relatively small field of view and often averaging over tens or hundreds of stars. Slowly we expanded the known catalog of PMs for MW satellites, both measuring multiple points within the SMC and LMC and measuring new systemic PMs for other MW satellites, including most of the classical satellites and a few of the fainter dwarfs. The release of *Gaia* DR2 reset the Local Group astrometry paradigm with the more than one billion sources with PMs. As a result, dozens of MW satellites had for the first time a systemic PM measurement. This new data set opened the door for exciting discoveries, like the first kinematic evidence for a satellite galaxy, the LMC, possessing satellites of its own, a key prediction of  $\Lambda$ CDM.

Similar, it brought the number of SMC PM measurements from  $\sim 40$  data points to well over 100,000 unique stellar PMs. Far from simplifying our view of the SMC,

this SMC catalog revealed the degree of turbulence the dwarf galaxy is undergoing, with clear outflows of stars away from the SMC. With the massive influx of PMs we also gained the ability to examine the kinematics of distinct stellar populations, a previously daunting task. This new separation of the sources has in turn revealed a dwarf galaxy that appears to noticeably different kinematic populations. Each of these populations offers a new constraint on the interaction history between the LMC and SMC, which in turn may provide new insight on the structure of the MW halo (e.g., MW mass versus LMC mass, number of expected satellites, location of tidal debris).

As we move forward from this point, the future of astrometry appears bright and exciting. On the near horizon, the Early Data Release 3 for *Gaia* (EDR3) will become available. With just an additional year of data, the expected PM precisions are projected to decrease by a factor of 2, which will once again increase the number of stars appropriate for including in astrometric analyses (like the red clump stars in the SMC). Perhaps more excitingly is the promise of the full release of RVs for stars (which currently are limited to stars brighter than the *Gaia* magnitude of about 14-15). With significantly more uniform coverage across the whole of the sky with 3D motions available, we may unlock yet more previously hidden tidal scars and debris in and around the MW and its satellites. Eventually Data Release 4 will also be made public, encompassing the full five years of data from the original mission, and is projected to increase the precision for PMs by nearly a factor of 5, compared to the current DR2 errors. For many of the classical satellites and even some of the fainter ones, this degree of precision will truly enable proper internal kinematic studies, comparable to the large and very bright LMC and SMC. This is to say nothing of the approved (and anticipated-to-be-approved) mission extensions for *Gaia* that

will provide a 10 year baseline, improving PM precisions by a factor of 12. With such a dramatic improvement, it would be possible to measure internal kinematics for many of the nearby satellites (within 50-60 kpc) with an error of only a  $\sim$ few km  $s^{-1}$ , comparable to the typical RV error.

However, while *Gaia* has excelled and will continue to excel at measuring systemic properties (and eventually internal kinematics) for MW satellites within 100 kpc, it is ultimately limited by the size of its mirror. As such, for many of the most recently discovered dwarf galaxy satellites, often referred to as “ultra-faint dwarfs” (UFDs), it has not been possible to identify stars in the *Gaia* catalog belonging to the UFDs. For this, it will require a new space-based telescope with a significantly larger primary mirror, capable of accurately observing stars multiple magnitudes fainter than is possible for *Gaia*. Fortunately such a telescope is near completion with the James Webb Space Telescope (JWST). With techniques first pioneered through *HST* data, JWST will be capable of measuring PMs for all known satellites in the MW halo, and potentially even measuring PMs for satellites of our neighbor Andromeda, providing a crucial second test for building our view of galaxy satellite kinematics.

Finally, in addition to the missions we have in place that will be able to study the kinematics of the known MW satellites, the community is on the cusp of discovering even more potential MW satellites. For ground-based observatories, the Large Synoptic Survey Telescope (LSST) is the flagship effort to provide a deep, all-sky survey of the southern hemisphere. Just as we could not anticipate the discoveries that would be made with SDSS, LSST will likely feature heavily in serendipitous and unexpected science in the following decade. For space-based missions, the Wide Field Infrared Survey Telescope (WFIRST) and Euclid will plan to survey large swathes of the night sky, offering a similar potential as LSST to find new satellite candidates

and perhaps other exotic dynamical objects orbiting the MW. The full potential of modern-era astrometry is only just beginning to be unlocked and all indications point to a bright future for Local Group kinematics.

## 6.2 Outstanding $\Lambda$ CDM Challenges

While great strides have been made in understanding the dynamics of MW satellites, significant work remains in the interpretation and application of these dynamics to constraining the broad cosmological paradigm. Many of the  $\Lambda$ CDM questions raised in the Introduction still remain unresolved to varying degrees. For example, in the case of the “missing satellites” problem, though it appears that the inclusion of baryonic physics is capable of creating broad agreement between simulations and observations, the exact agreement remains uncertain. A significant factor in play is the uncertainty surrounding the MW mass, as the full halo mass remains uncertain at potentially up to the 50% level (Fritz et al. 2020). As simulations have shown, the range of masses covered by this uncertainty can produce significant differences in the expected satellite population, especially at the lower mass end of the scale in the UFD regime.

Ultimately solving the question of the MW mass will require a combination of multiple factors. Currently the number of dynamic tracers, like the satellite galaxies, with measured PMs in the outer part of the MW halo is relatively small. Continuing to measure systemic PMs for the faint satellites, both the known and the potential waiting-to-be-discovered, will be crucial for better sampling the halo phase space and better constraining the total mass within their orbits. However, even if a total mass out to  $\sim 300$  kpc is able to be determined, a second complicating aspect has already presented itself: the presence of the LMC, which some studies have suggested may be up to 10% or more of the MW’s mass (Erkal et al. 2020). It will require significantly

more satellite PMs with higher precision in order to properly disentangle the mass contributions from these two interacting galaxies (Garavito-Camargo et al. 2019). Improved understanding of the interaction history of the LMC-SMC, and in turn the Magellanic Clouds and the MW, will play a vital role in this goal as well.

Beyond the “missing satellites” problem, others remain as well. One problem that improved modeling of satellite kinematics is well-suited to inform is the “too big to fail” problem. As previously explained, the inferred halo masses of the classical MW satellites appear to be too small for the largest halos found in simulations. Currently we are only able to measure the halo masses for these larger systems, limiting our ability to compare the full extent of the MW halo mass function to that of simulated MWs (which the above discussion on MW mass will also ultimately inform). However, as our ability to measure the internal kinematics of fainter and fainter MW satellites improves, we will be able to better describe the full halo mass function, without needing to rely on mass-to-light estimates in a regime that we have not been able to observationally test. By developing a proper 3D model capable of capturing different contributions to a satellite’s kinematic structure, we will be better positioned to properly assess the satellite mass at ever larger radii (thus a more accurate measurement of the total halo mass, similar to the uncertainties in measuring the MW halo mass).

We are closer than ever to answering some of the fundamental questions posed in near-field cosmology, and Local Group astrometry will play a critical role in the final formulation of those answers.

# References

Ahumada, R., Allende Prieto, C., Almeida, A., Anders, F., Anderson, S. F., Andrews, B. H., Anguiano, B., Arcodia, R., Armengaud, E., Aubert, M., Avila, S., Avila-Reese, V., Badenes, C., Balland, C., Barger, K., Barrera-Ballesteros, J. K., Basu, S., Bautista, J., Beaton, R. L., Beers, T. C., Benavides, B. I. T., Bender, C. F., Bernardi, M., Bershady, M., Beutler, F., Moni Bidin, C., Bird, J., Bizyaev, D., Blanc, G. A., Blanton, M. R., Boquien, M., Borissova, J., Bovy, J., Brandt, W. N., Brinkmann, J., Brownstein, J. R., Bundy, K., Bureau, M., Burgasser, A., Burtin, E., Cano-Diaz, M., Capasso, R., Cappellari, M., Carrera, R., Chabanier, S., Chaplin, W., Chapman, M., Cherinka, B., Chiappini, C., Choi, P. D., Chojnowski, S. D., Chung, H., Clerc, N., Coffey, D., Comerford, J. M., Comparat, J., da Costa, L., Cousinou, M.-C., Covey, K., Crane, J. D., Cunha, K., da Silva Ilha, G., Dai, Y. S., Damsted, S. B., Darling, J., Horta Darrington, D., Davidson, James W., J., Davies, R., Dawson, K., De, N., de la Macorra, A., De Lee, N., Queiroz, A. B. d. A., Deconto Machado, A., de la Torre, S., Dell'Agli, F., du Mas des Bourboux, H., Diamond-Stanic, A. M., Dillon, S., Donor, J., Drory, N., Duckworth, C., Dwelly, T., Ebelke, G., Eftekharzadeh, S., Davis Eigenbrot, A., Elsworth, Y. P., Eracleous, M., Erfanianfar, G., Escoffier, S., Fan, X., Farr, E., Fernandez-Trincado, J. G., Feuillet, D., Finoguenov, A., Fofie, P., Fraser-McKelvie, A., Frinchaboy, P. M., Fromenteau, S., Fu, H., Galbany, L., Garcia, R. A., Garcia-Hernandez, D. A.,

Garma Oehmichen, L. A., Ge, J., Geimba Maia, M. A., Geisler, D., Gelfand, J., Goddy, J., Le Goff, J.-M., Gonzalez-Perez, V., Grabowski, K., Green, P., Grier, C. J., Guo, H., Guy, J., Harding, P., Hasselquist, S., Hawken, A. J., Hayes, C. R., Hearty, F., Hekker, S., Hogg, D. W., Holtzman, J., Hou, J., Hsieh, B.-C., Huber, D., Hunt, J. A. S., Ider Chitham, J., Imig, J., Jaber, M., Jimenez Angel, C. E., Johnson, J. A., Jones, A. M., Jonsson, H., Jullo, E., Kim, Y., Kinemuchi, K., Kirkpatrick, Charles C., I., Kite, G. W., Klaene, M., Kneib, J.-P., Kollmeier, J. A., Kong, H., Kounkel, M., Krishnarao, D., Lacerna, I., Lan, T.-W., Lane, R. R., Law, D. R., Leung, H. W., Lewis, H., Li, C., Lian, J., Lin, L., Long, D., Longa-Pena, P., Lundgren, B., Lyke, B. W., Mackereth, J. T., MacLeod, C. L., Majewski, S. R., Manchado, A., Maraston, C., Martini, P., Masseron, T., Masters, K. L., Mathur, S., McDermid, R. M., Merloni, A., Merrifield, M., Meszaros, S., Miglio, A., Minniti, D., Minsley, R., Miyaji, T., Gohar Mohammad, F., Mosser, B., Mueller, E.-M., Muna, D., Munoz-Gutierrez, A., Myers, A. D., Nadathur, S., Nair, P., Correa do Nascimento, J., Nevin, R. J., Newman, J. A., Nidever, D. L., Nitschelm, C., Noterdaeme, P., O'Connell, J. E., Olmstead, M. D., Oravetz, D., Oravetz, A., Osorio, Y., Pace, Z. J., Padilla, N., Palanque-Delabrouille, N., Palicio, P. A., Pan, H.-A., Pan, K., Parker, J., Paviot, R., Peirani, S., Pena Ramirez, K., Penny, S., Percival, W. J., Perez-Fournon, I., Perez-Rafols, I., Petitjean, P., Pieri, M. M., Pinsonneault, M., Poovelil, V. J., Povick, J. T., Prakash, A., Price-Whelan, A. M., Raddick, M. J., Raichoor, A., Ray, A., Barboza Rembold, S., Rezaie, M., Riffel, R. A., Riffel, R., Rix, H.-W., Robin, A. C., Roman-Lopes, A., Roman-Zuniga, C., Rose, B., Ross, A. J., Rossi, G., Rowlands, K., Rubin, K. H. R., Salvato, M., Sanchez, A. G., Sanchez-Menguiano, L., Sanchez-Gallego, J. R., Sayres, C., Schaefer, A., Schiavon, R. P., Schimoia, J. S., Schlafly, E., Schlegel, D., Schneider, D. P., Schultheis, M.,

- Schwobe, A., Seo, H.-J., Serenelli, A., Shafieloo, A., Shamsi, S. J., Shao, Z., Shen, S., Shetrone, M., Shirley, R., Silva Aguirre, V., Simon, J. D., Skrutskie, M. F., Slosar, A., Smethurst, R., Sobek, J., Cervantes Sodi, B., Souto, D., Stark, D. V., Stassun, K. G., Steinmetz, M., Stello, D., Stermer, J., Storchi-Bergmann, T., Streblyanska, A., Stringfellow, G. S., Stutz, A., Suarez, G., Sun, J., Taghizadeh-Popp, M., Talbot, M. S., Tayar, J., Thakar, A. R., Theriault, R., Thomas, D., Thomas, Z. C., Tinker, J., Tojeiro, R., Hernandez Toledo, H., Tremonti, C. A., Troup, N. W., Tuttle, S., Unda-Sanzana, E., Valentini, M., Vargas-Gonzalez, J., Vargas-Magana, M., Vazquez-Mata, J. A., Vivek, M., Wake, D., Wang, Y., Weaver, B. A., Weijmans, A.-M., Wild, V., Wilson, J. C., Wilson, R. F., Wolthuis, N., Wood-Vasey, W. M., Yan, R., Yang, M., Yeche, C., Zamora, O., Zarrouk, P., Zasowski, G., Zhang, K., Zhao, C., Zhao, G., Zheng, Z., Zheng, Z., Zhu, G., & Zou, H. 2019, arXiv e-prints, arXiv:1912.02905
- Anderson, J. 2014, The Impact of x-CTE in the WFC3/UVIS detector on Astrometry, Tech. rep.
- Anderson, J. & King, I. R. 2004, Multi-filter PSFs and Distortion Corrections for the HRC, Tech. rep.
- . 2006, PSFs, Photometry, and Astronomy for the ACS/WFC, Tech. rep.
- Bagheri, G., Cioni, M.-R. L., & Napiwotzki, R. 2013, *A&A*, 551, A78
- Bekki, K. & Chiba, M. 2007, *PASA*, 24, 21
- Bellini, A., Anderson, J., & Bedin, L. R. 2011, *PASP*, 123, 622
- Belokurov, V., Erkal, D., Deason, A. J., Koposov, S. E., De Angeli, F., Evans, D. W., Fraternali, F., & Mackey, D. 2017, *MNRAS*, 466, 4711

- Belokurov, V. & Koposov, S. E. 2016, *MNRAS*, 456, 602
- Belokurov, V. A. & Erkal, D. 2019, *MNRAS*, 482, L9
- Besla, G. 2011, PhD thesis, Harvard University
- Besla, G., Kallivayalil, N., Hernquist, L., Robertson, B., Cox, T. J., van der Marel, R. P., & Alcock, C. 2007, *ApJ*, 668, 949
- Besla, G., Kallivayalil, N., Hernquist, L., van der Marel, R. P., Cox, T. J., & Kereš, D. 2012, *MNRAS*, 421, 2109
- Besla, G., Martínez-Delgado, D., van der Marel, R. P., Beletsky, Y., Seibert, M., Schlafly, E. F., Grebel, E. K., & Neyer, F. 2016, *ApJ*, 825, 20
- Bland-Hawthorn, J. & Gerhard, O. 2016, *ARA&A*, 54, 529
- Blanton, M. R., Bershady, M. A., Abolfathi, B., Albareti, F. D., Allende Prieto, C., Almeida, A., Alonso-García, J., Anders, F., Anderson, S. F., Andrews, B., Aquino-Ortíz, E., Aragón-Salamanca, A., Argudo-Fernández, M., Armengaud, E., Aubourg, E., Avila-Reese, V., Badenes, C., Bailey, S., Barger, K. A., Barrera-Ballesteros, J., Bartosz, C., Bates, D., Baumgarten, F., Bautista, J., Beaton, R., Beers, T. C., Belfiore, F., Bender, C. F., Berlind, A. A., Bernardi, M., Beutler, F., Bird, J. C., Bizyaev, D., Blanc, G. A., Blomqvist, M., Bolton, A. S., Boquien, M., Borissova, J., van den Bosch, R., Bovy, J., Brandt, W. N., Brinkmann, J., Brownstein, J. R., Bundy, K., Burgasser, A. J., Burtin, E., Busca, N. G., Cappellari, M., Delgado Carigi, M. L., Carlberg, J. K., Carnero Rosell, A., Carrera, R., Chanover, N. J., Cherinka, B., Cheung, E., Gómez Maqueo Chew, Y., Chiappini, C., Choi, P. D., Chojnowski, D., Chuang, C.-H., Chung, H., Cirolini, R. F., Clerc, N., Cohen, R. E., Comparat, J., da Costa, L., Cousinou, M.-C., Covey, K., Crane,

J. D., Croft, R. A. C., Cruz-Gonzalez, I., Garrido Cuadra, D., Cunha, K., Damke, G. J., Darling, J., Davies, R., Dawson, K., de la Macorra, A., Dell'Agli, F., De Lee, N., Delubac, T., Di Mille, F., Diamond-Stanic, A., Cano-Díaz, M., Donor, J., Downes, J. J., Drory, N., du Mas des Bourboux, H., Duckworth, C. J., Dwelly, T., Dyer, J., Ebelke, G., Eigenbrot, A. D., Eisenstein, D. J., Emsellem, E., Eracleous, M., Escoffier, S., Evans, M. L., Fan, X., Fernández-Alvar, E., Fernandez-Trincado, J. G., Feuillet, D. K., Finoguenov, A., Fleming, S. W., Font-Ribera, A., Fredrickson, A., Freischlad, G., Frinchaboy, P. M., Fuentes, C. E., Galbany, L., Garcia-Dias, R., García-Hernández, D. A., Gaulme, P., Geisler, D., Gelfand, J. D., Gil-Marín, H., Gillespie, B. A., Goddard, D., Gonzalez-Perez, V., Grabowski, K., Green, P. J., Grier, C. J., Gunn, J. E., Guo, H., Guy, J., Hagen, A., Hahn, C., Hall, M., Harding, P., Hasselquist, S., Hawley, S. L., Hearty, F., Gonzalez Hernández, J. I., Ho, S., Hogg, D. W., Holley-Bockelmann, K., Holtzman, J. A., Holzer, P. H., Huehnerhoff, J., Hutchinson, T. A., Hwang, H. S., Ibarra-Medel, H. J., da Silva Ilha, G., Ivans, I. I., Ivory, K., Jackson, K., Jensen, T. W., Johnson, J. A., Jones, A., Jönsson, H., Jullo, E., Kamble, V., Kinemuchi, K., Kirkby, D., Kitaura, F.-S., Klaene, M., Knapp, G. R., Kneib, J.-P., Kollmeier, J. A., Lacerna, I., Lane, R. R., Lang, D., Law, D. R., Lazarz, D., Lee, Y., Le Goff, J.-M., Liang, F.-H., Li, C., Li, H., Lian, J., Lima, M., Lin, L., Lin, Y.-T., Bertran de Lis, S., Liu, C., de Icaza Lizaola, M. A. C., Long, D., Lucatello, S., Lundgren, B., MacDonald, N. K., Deconto Machado, A., MacLeod, C. L., Mahadevan, S., Geimba Maia, M. A., Maiolino, R., Majewski, S. R., Malanushenko, E., Malanushenko, V., Manchado, A., Mao, S., Maraston, C., Marques-Chaves, R., Masseron, T., Masters, K. L., McBride, C. K., McDermid, R. M., McGrath, B., McGreer, I. D., Medina Peña, N., Melendez, M., Merloni, A., Merrifield, M. R., Meszaros, S., Meza, A., Minchev, I., Minniti, D., Miyaji, T.,

More, S., Mulchaey, J., Müller-Sánchez, F., Muna, D., Munoz, R. R., Myers, A. D., Nair, P., Nandra, K., Correa do Nascimento, J., Negrete, A., Ness, M., Newman, J. A., Nichol, R. C., Nidever, D. L., Nitschelm, C., Ntelis, P., O'Connell, J. E., Oelkers, R. J., Oravetz, A., Oravetz, D., Pace, Z., Padilla, N., Palanque-Delabrouille, N., Alonso Palicio, P., Pan, K., Parejko, J. K., Parikh, T., Pâris, I., Park, C., Patten, A. Y., Peirani, S., Pellejero-Ibanez, M., Penny, S., Percival, W. J., Perez-Fournon, I., Petitjean, P., Pieri, M. M., Pinsonneault, M., Pisani, A., Poleski, R., Prada, F., Prakash, A., Queiroz, A. B. d. A., Raddick, M. J., Raichoor, A., Barboza Rembold, S. r., Richstein, H., Riffel, R. A., Riffel, R., Rix, H.-W., Robin, A. C., Rockosi, C. M., Rodríguez-Torres, S., Roman-Lopes, A., Román-Zúñiga, C., Rosado, M., Ross, A. J., Rossi, G., Ruan, J., Ruggeri, R., Rykoff, E. S., Salazar-Albornoz, S., Salvato, M., Sánchez, A. G., Aguado, D. S., Sánchez-Gallego, J. R., Santana, F. A., Santiago, B. X., Sayres, C., Schiavon, R. P., da Silva Schimoia, J., Schlafly, E. F., Schlegel, D. J., Schneider, D. P., Schultheis, M., Schuster, W. J., Schwobe, A., Seo, H.-J., Shao, Z., Shen, S., Shetrone, M., Shull, M., Simon, J. D., Skinner, D., Skrutskie, M. F., Slosar, A., Smith, V. V., Sobek, J. S., Sobreira, F., Somers, G., Souto, D., Stark, D. V., Stassun, K., Stauffer, F., Steinmetz, M., Storchi-Bergmann, T., Streblyanska, A., Stringfellow, G. S., Suárez, G., Sun, J., Suzuki, N., Szigeti, L., Taghizadeh-Popp, M., Tang, B., Tao, C., Tayar, J., Tembe, M., Teske, J., Thakar, A. R., Thomas, D., Thompson, B. A., Tinker, J. L., Tissera, P., Tojeiro, R., Hernandez Toledo, H., de la Torre, S., Tremonti, C., Troup, N. W., Valenzuela, O., Martinez Valpuesta, I., Vargas-González, J., Vargas-Magaña, M., Vazquez, J. A., Villanova, S., Vivek, M., Vogt, N., Wake, D., Walterbos, R., Wang, Y., Weaver, B. A., Weijmans, A.-M., Weinberg, D. H., Westfall, K. B., Whelan, D. G., Wild, V., Wilson, J., Wood-Vasey, W. M., Wylezalek, D., Xiao, T., Yan,

- R., Yang, M., Ybarra, J. E., Yèche, C., Zakamska, N., Zamora, O., Zarrouk, P., Zasowski, G., Zhang, K., Zhao, G.-B., Zheng, Z., Zheng, Z., Zhou, X., Zhou, Z.-M., Zhu, G. B., Zoccali, M., & Zou, H. 2017, *AJ*, 154, 28
- Bovy, J., Allende Prieto, C., Beers, T. C., Bizyaev, D., da Costa, L. N., Cunha, K., Ebelke, G. L., Eisenstein, D. J., Frinchaboy, P. M., García Pérez, A. E., Girardi, L., Hearty, F. R., Hogg, D. W., Holtzman, J., Maia, M. A. G., Majewski, S. R., Malanushenko, E., Malanushenko, V., Mészáros, S., Nidever, D. L., O’Connell, R. W., O’Donnell, C., Oravetz, A., Pan, K., Rocha-Pinto, H. J., Schiavon, R. P., Schneider, D. P., Schultheis, M., Skrutskie, M., Smith, V. V., Weinberg, D. H., Wilson, J. C., & Zasowski, G. 2012, *ApJ*, 759, 131
- Boylan-Kolchin, M., Besla, G., & Hernquist, L. 2011, *MNRAS*, 414, 1560
- Boylan-Kolchin, M., Bullock, J. S., & Kaplinghat, M. 2012, *MNRAS*, 422, 1203
- Bullock, J. S. & Boylan-Kolchin, M. 2017, *ARA&A*, 55, 343
- Carrera, R., Conn, B. C., Noël, N. E. D., Read, J. I., & López Sánchez, Á. R. 2017, ArXiv e-prints
- Choi, Y., Nidever, D. L., Olsen, K., Besla, G., Blum, R. D., Zaritsky, D., Cioni, M.-R. L., van der Marel, R. P., Bell, E. F., Johnson, L. C., Vivas, A. K., Walker, A. R., de Boer, T. J. L., Noel, N. E. D., Monachesi, A., Gallart, C., Monelli, M., Stringfellow, G. S., Massana, P., & Martinez-Delgado, D. 2018a, ArXiv e-prints
- Choi, Y., Nidever, D. L., Olsen, K., Blum, R. D., Besla, G., Zaritsky, D., van der Marel, R. P., Bell, E. F., Gallart, C., Cioni, M.-R. L., Johnson, L. C., Vivas, A. K., Saha, A., de Boer, T. J. L., Noel, N. E. D., Monachesi, A., Massana, P., Conn, B. C., Martinez-Delgado, D., & Munoz, R. R. 2018b, ArXiv e-prints

- Cioni, M.-R. L., Bekki, K., Girardi, L., de Grijs, R., Irwin, M. J., Ivanov, V. D., Marconi, M., Oliveira, J. M., Piatti, A. E., Ripepi, V., & van Loon, J. T. 2016, *A&A*, 586, A77
- Cioni, M.-R. L., van der Marel, R. P., Loup, C., & Habing, H. J. 2000, *A&A*, 359, 601
- de Blok, W. J. G., Walter, F., Brinks, E., Trachternach, C., Oh, S. H., & Kennicutt, R. C., J. 2008, *AJ*, 136, 2648
- De Leo, M., Carrera, R., Noel, N. E. D., Read, J. I., Erkal, D., & Gallart, C. 2020, arXiv e-prints, arXiv:2002.11138
- Deason, A. J., Mao, Y.-Y., & Wechsler, R. H. 2016, *ApJ*, 821, 5
- Demers, S. & Battinelli, P. 1998, *AJ*, 115, 154
- Di Teodoro, E. M., McClure-Griffiths, N. M., Jameson, K. E., Dénes, H., Dickey, J. M., Stanimirović, S., Staveley-Smith, L., Anderson, C., Bunton, J. D., Chippendale, A., Lee-Waddell, K., MacLeod, A., & Voronkov, M. A. 2019, *MNRAS*, 483, 392
- Dias, B., Kerber, L., Barbuy, B., Bica, E., & Ortolani, S. 2016, *A&A*, 591, A11
- Diaz, J. D. & Bekki, K. 2012, *ApJ*, 750, 36
- Dobbie, P. D., Cole, A. A., Subramaniam, A., & Keller, S. 2014, *MNRAS*, 442, 1663
- Dotter, A., Chaboyer, B., Jevremović, D., Kostov, V., Baron, E., & Ferguson, J. W. 2008, *ApJS*, 178, 89

Drlica-Wagner, A., Bechtol, K., Rykoff, E. S., Luque, E., Queiroz, A., Mao, Y. Y., Wechsler, R. H., Simon, J. D., Santiago, B., Yanny, B., Balbinot, E., Dodelson, S., Fausti Neto, A., James, D. J., Li, T. S., Maia, M. A. G., Marshall, J. L., Pieres, A., Stringer, K., Walker, A. R., Abbott, T. M. C., Abdalla, F. B., Allam, S., Benoit-Lévy, A., Bernstein, G. M., Bertin, E., Brooks, D., Buckley-Geer, E., Burke, D. L., Carnero Rosell, A., Carrasco Kind, M., Carretero, J., Croce, M., da Costa, L. N., Desai, S., Diehl, H. T., Dietrich, J. P., Doel, P., Eifler, T. F., Evrard, A. E., Finley, D. A., Flaughner, B., Fosalba, P., Frieman, J., Gaztanaga, E., Gerdes, D. W., Gruen, D., Gruendl, R. A., Gutierrez, G., Honscheid, K., Kuehn, K., Kuropatkin, N., Lahav, O., Martini, P., Miquel, R., Nord, B., Ogando, R., Plazas, A. A., Reil, K., Roodman, A., Sako, M., Sanchez, E., Scarpine, V., Schubnell, M., Sevilla-Noarbe, I., Smith, R. C., Soares-Santos, M., Sobreira, F., Suchyta, E., Swanson, M. E. C., Tarle, G., Tucker, D., Vikram, V., Wester, W., Zhang, Y., Zuntz, J., & DES Collaboration. 2015, *ApJ*, 813, 109

Erkal, D., Belokurov, V., & Parkin, D. L. 2020, arXiv e-prints, arXiv:2001.11030

Evans, C. J. & Howarth, I. D. 2008, *MNRAS*, 386, 826

Feast, M. W., Thackeray, A. D., & Wesselink, A. J. 1961, *MNRAS*, 122, 433

Freedman, D. & Diaconis, P. Z. 1981, *Wahrscheinlichkeitstheorie verw Gebiete*, 57

Freedman, W. L., Madore, B. F., Gibson, B. K., Ferrarese, L., Kelson, D. D., Sakai, S., Mould, J. R., Kennicutt, Jr., R. C., Ford, H. C., Graham, J. A., Huchra, J. P., Hughes, S. M. G., Illingworth, G. D., Macri, L. M., & Stetson, P. B. 2001, *ApJ*, 553, 47

- Fritz, T. K., Di Cintio, A., Battaglia, G., Brook, C., & Taibi, S. 2020, arXiv e-prints, arXiv:2001.02651
- Fritz, T. K., Linden, S. T., Zivick, P., Kallivayalil, N., Beaton, R. L., Bovy, J., Sales, L. V., Sohn, T., Angell, D., Boylan-Kolchin, M., Carrasco, E. R., Damke, G., Davies, R., Majewski, S., Neichel, B., & van der Marel, R. 2017a, *ApJ*, 840, 30
- Fritz, T. K., Lokken, M., Kallivayalil, N., Wetzell, A., Linden, S. T., Zivick, P., & Tollerud, E. J. 2017b, ArXiv e-prints
- Fukui, Y., Tokuda, K., Saigo, K., Harada, R., Tachihara, K., Tsuge, K., Inoue, T., Torii, K., Nishimura, A., Zahorecz, S., Nayak, O., Meixner, M., Minamidani, T., Kawamura, A., Mizuno, N., Indebetouw, R., Sewiło, M., Madden, S., Galametz, M., Lebouteiller, V., Chen, C.-H. R., & Onishi, T. 2018, ArXiv e-prints
- Gaia Collaboration, Babusiaux, C., van Leeuwen, F., Barstow, M. A., Jordi, C., Vallenari, A., Bossini, D., Bressan, A., Cantat-Gaudin, T., van Leeuwen, M., & et al. 2018a, *A&A*, 616, A10
- Gaia Collaboration, Brown, A. G. A., Vallenari, A., Prusti, T., de Bruijne, J. H. J., Babusiaux, C., Bailer-Jones, C. A. L., Biermann, M., Evans, D. W., Eyer, L., & et al. 2018b, *A&A*, 616, A1
- Gaia Collaboration, Brown, A. G. A., Vallenari, A., Prusti, T., de Bruijne, J. H. J., Mignard, F., Drimmel, R., Babusiaux, C., Bailer-Jones, C. A. L., Bastian, U., & et al. 2016a, *A&A*, 595, A2
- Gaia Collaboration, Helmi, A., van Leeuwen, F., McMillan, P. J., Massari, D., Antoja, T., Robin, A. C., Lindegren, L., Bastian, U., Arenou, F., & et al. 2018c, *A&A*, 616, A12

- Gaia Collaboration, Prusti, T., de Bruijne, J. H. J., Brown, A. G. A., Vallenari, A., Babusiaux, C., Bailer-Jones, C. A. L., Bastian, U., Biermann, M., Evans, D. W., & et al. 2016b, *A&A*, 595, A1
- . 2016c, *A&A*, 595, A1
- Garavito-Camargo, N., Besla, G., Laporte, C. F. P., Johnston, K. V., Gómez, F. A., & Watkins, L. L. 2019, *ApJ*, 884, 51
- Gardiner, L. T. & Noguchi, M. 1996, *MNRAS*, 278, 191
- Garrison-Kimmel, S., Boylan-Kolchin, M., Bullock, J. S., & Lee, K. 2014, *MNRAS*, 438, 2578
- Garrison-Kimmel, S., Bullock, J. S., Boylan-Kolchin, M., & Bardwell, E. 2017, *MNRAS*, 464, 3108
- Gnedin, O. Y., Kravtsov, A. V., Klypin, A. A., & Nagai, D. 2004, *ApJ*, 616, 16
- Gómez, F. A., Besla, G., Carpinero, D. D., Villalobos, Á., O’Shea, B. W., & Bell, E. F. 2015, *ApJ*, 802, 128
- Gonzaga, S. & et al. 2012, *The DrizzlePac Handbook*
- Guglielmo, M., Lewis, G. F., & Bland-Hawthorn, J. 2014, *MNRAS*, 444, 1759
- Harris, J. 2007, *ApJ*, 658, 345
- Harris, J. & Zaritsky, D. 2006, *AJ*, 131, 2514
- Hernquist, L. 1990, *ApJ*, 356, 359
- Hindman, J. V., Kerr, F. J., & McGee, R. X. 1963, *Australian Journal of Physics*, 16, 570

- Høg, E., Fabricius, C., Makarov, V. V., Urban, S., Corbin, T., Wycoff, G., Bastian, U., Schwekendiek, P., & Wicenec, A. 2000, *A&A*, 355, L27
- Homma, D., Chiba, M., Komiyama, Y., Tanaka, M., Okamoto, S., Tanaka, M., Ishigaki, M. N., Hayashi, K., Arimoto, N., Carlsten, S. G., Lupton, R. H., Strauss, M. A., Miyazaki, S., Torrealba, G., Wang, S.-Y., & Murayama, H. 2019, *PASJ*, 71, 94
- Homma, D., Chiba, M., Okamoto, S., Komiyama, Y., Tanaka, M., Tanaka, M., Ishigaki, M. N., Hayashi, K., Arimoto, N., Garmilla, J. A., Lupton, R. H., Strauss, M. A., Miyazaki, S., Wang, S.-Y., & Murayama, H. 2018, *PASJ*, 70, S18
- Irwin, M. J., Kunkel, W. E., & Demers, S. 1985, *Nature*, 318, 160
- Jacyszyn-Dobrzaniecka, A. M., Skowron, D. M., Mróz, P., Soszyński, I., Udalski, A., Pietrukowicz, P., Skowron, J., Poleski, R., Kozłowski, S., Wyrzykowski, Ł., Pawlak, M., Szymański, M. K., & Ulaczyk, K. 2017, *AcA*, 67, 1
- Jethwa, P., Erkal, D., & Belokurov, V. 2016, *MNRAS*, 461, 2212
- Joshi, Y. C. & Panchal, A. 2019, *A&A*, 628, A51
- Kallivayalil, N., Sales, L. V., Zivick, P., Fritz, T. K., Del Pino, A., Sohn, S. T., Besla, G., van der Marel, R. P., Navarro, J. F., & Sacchi, E. 2018, *ApJ*, 867, 19
- Kallivayalil, N., van der Marel, R. P., & Alcock, C. 2006a, *ApJ*, 652, 1213
- Kallivayalil, N., van der Marel, R. P., Alcock, C., Axelrod, T., Cook, K. H., Drake, A. J., & Geha, M. 2006b, *ApJ*, 638, 772
- Kallivayalil, N., van der Marel, R. P., Besla, G., Anderson, J., & Alcock, C. 2013, *ApJ*, 764, 161

- Koposov, S. E., Belokurov, V., Torrealba, G., & Evans, N. W. 2015, *ApJ*, 805, 130
- Kozłowski, S., Onken, C. A., Kochanek, C. S., Udalski, A., Szymański, M. K., Ku-  
biak, M., Pietrzyński, G., Soszyński, I., Wyrzykowski, Ł., Ulaczyk, K., Poleski,  
R., Pietrukowicz, P., Skowron, J., OGLE Collaboration, Meixner, M., & Bonanos,  
A. Z. 2013, *ApJ*, 775, 92
- Kunkel, W. E. & Demers, S. 1976, in *The Galaxy and the Local Group*, Vol. 182, 241
- Lamb, J. B., Oey, M. S., Segura-Cox, D. M., Graus, A. S., Kiminki, D. C., Golden-  
Marx, J. B., & Parker, J. W. 2016, *ApJ*, 817, 113
- Laporte, C. F. P., Gómez, F. A., Besla, G., Johnston, K. V., & Garavito-Camargo,  
N. 2018, *MNRAS*, 473, 1218
- Laporte, C. F. P., Johnston, K. V., Gómez, F. A., Garavito-Camargo, N., & Besla,  
G. 2017, *ArXiv e-prints*
- Lindegren, L., Hernández, J., Bombrun, A., Klioner, S., Bastian, U., Ramos-Lerate,  
M., de Torres, A., Steidelmüller, H., Stephenson, C., Hobbs, D., Lammers, U.,  
Biermann, M., Geyer, R., Hilger, T., Michalik, D., Stampa, U., McMillan, P. J.,  
Castañeda, J., Clotet, M., Comoretto, G., Davidson, M., Fabricius, C., Gracia, G.,  
Hambly, N. C., Hutton, A., Mora, A., Portell, J., van Leeuwen, F., Abbas, U.,  
Abreu, A., Altmann, M., Andrei, A., Anglada, E., Balaguer-Núñez, L., Barache,  
C., Becciani, U., Bertone, S., Bianchi, L., Bouquillon, S., Bourda, G., Brüsemeister,  
T., Bucciarelli, B., Busonero, D., Buzzi, R., Cancelliere, R., Carlucci, T., Charlot,  
P., Cheek, N., Crosta, M., Crowley, C., de Bruijne, J., de Felice, F., Drimmel, R.,  
Esquej, P., Fienga, A., Fraile, E., Gai, M., Garralda, N., González-Vidal, J. J.,  
Guerra, R., Hauser, M., Hofmann, W., Holl, B., Jordan, S., Lattanzi, M. G.,

- Lenhardt, H., Liao, S., Licata, E., Lister, T., Löffler, W., Marchant, J., Martin-Fleitas, J.-M., Messineo, R., Mignard, F., Morbidelli, R., Poggio, E., Riva, A., Rowell, N., Salguero, E., Sarasso, M., Sciacca, E., Siddiqui, H., Smart, R. L., Spagna, A., Steele, I., Taris, F., Torra, J., van Elteren, A., van Reeve, W., & Vecchiato, A. 2018, *A&A*, 616, A2
- Lindegren, L., Lammers, U., Bastian, U., Hernández, J., Klioner, S., Hobbs, D., Bombrun, A., Michalik, D., Ramos-Lerate, M., Butkevich, A., Comoretto, G., Joliet, E., Holl, B., Hutton, A., Parsons, P., Steidelmüller, H., Abbas, U., Altmann, M., Andrei, A., Anton, S., Bach, N., Barache, C., Becciani, U., Berthier, J., Bianchi, L., Biermann, M., Bouquillon, S., Bourda, G., Brüsemeister, T., Bucciarelli, B., Busonero, D., Carlucci, T., Castañeda, J., Charlot, P., Clotet, M., Crosta, M., Davidson, M., de Felice, F., Drimmel, R., Fabricius, C., Fienga, A., Figueras, F., Fraile, E., Gai, M., Garralda, N., Geyer, R., González-Vidal, J. J., Guerra, R., Hambly, N. C., Hauser, M., Jordan, S., Lattanzi, M. G., Lenhardt, H., Liao, S., Löffler, W., McMillan, P. J., Mignard, F., Mora, A., Morbidelli, R., Portell, J., Riva, A., Sarasso, M., Serraller, I., Siddiqui, H., Smart, R., Spagna, A., Stampa, U., Steele, I., Taris, F., Torra, J., van Reeve, W., Vecchiato, A., Zschocke, S., de Bruijne, J., Gracia, G., Raison, F., Lister, T., Marchant, J., Messineo, R., Soffel, M., Osorio, J., de Torres, A., & O'Mullane, W. 2016, *A&A*, 595, A4
- Mackey, A. D., Kozlov, S. E., Erkal, D., Belokurov, V., Da Costa, G. S., & Gómez, F. A. 2016, *MNRAS*, 459, 239
- Mackey, D., Kozlov, S., Da Costa, G., Belokurov, V., Erkal, D., & Kuzma, P. 2018, *ApJ*, 858, L21
- Majewski, S. R., Schiavon, R. P., Frinchaboy, P. M., Allende Prieto, C., Barkhouser,

- R., Bizyaev, D., Blank, B., Brunner, S., Burton, A., Carrera, R., Chojnowski, S. D., Cunha, K., Epstein, C., Fitzgerald, G., García Pérez, A. E., Hearty, F. R., Henderson, C., Holtzman, J. A., Johnson, J. A., Lam, C. R., Lawler, J. E., Mase-man, P., Mészáros, S., Nelson, M., Nguyen, D. C., Nidever, D. L., Pinsonneault, M., Shetrone, M., Smee, S., Smith, V. V., Stolberg, T., Skrutskie, M. F., Walker, E., Wilson, J. C., Zasowski, G., Anders, F., Basu, S., Beland, S., Blanton, M. R., Bovy, J., Brownstein, J. R., Carlberg, J., Chaplin, W., Chiappini, C., Eisenstein, D. J., Elsworth, Y., Feuillet, D., Fleming, S. W., Galbraith-Frew, J., García, R. A., García-Hernández, D. A., Gillespie, B. A., Girardi, L., Gunn, J. E., Hasselquist, S., Hayden, M. R., Hekker, S., Ivans, I., Kinemuchi, K., Klaene, M., Mahadevan, S., Mathur, S., Mosser, B., Muna, D., Munn, J. A., Nichol, R. C., O’Connell, R. W., Parejko, J. K., Robin, A. C., Rocha-Pinto, H., Schultheis, M., Serenelli, A. M., Shane, N., Silva Aguirre, V., Sobek, J. S., Thompson, B., Troup, N. W., Weinberg, D. H., & Zamora, O. 2017, *AJ*, 154, 94
- Marigo, P., Girardi, L., Bressan, A., Rosenfield, P., Aringer, B., Chen, Y., Dussin, M., Nanni, A., Pastorelli, G., Rodrigues, T. S., Trabucchi, M., Bladh, S., Dalcanton, J., Groenewegen, M. A. T., Montalbán, J., & Wood, P. R. 2017, *ApJ*, 835, 77
- Martinez-Delgado, D., Vivas, A. K., Grebel, E. K., Gallart, C., Pieres, A., Bell, C. P. M., Zivick, P., Lemasle, B., Johnson, L. C., Carballo-Bello, J. A., Noel, N. E. D., Cioni, M.-R. L., Choi, Y., Besla, G., Schmidt, J., Zaritsky, D., Gruendl, R. A., Seibert, M., Nidever, D., Monteagudo, L., Monelli, M., Hubl, B., van der Marel, R., Ballesteros, F. J., Stringfellow, G., Walker, A., Blum, R., Bell, E. F., Conn, B. C., Olsen, K., Martin, N., Chu, Y.-H., Inno, L., Boer, T. J. L., Kallivayalil, N., De Leo, M., Beletsky, Y., & Munoz, R. R. 2019, arXiv e-prints, arXiv:1907.02264

- McClure-Griffiths, N. M., Dénes, H., Dickey, J. M., Stanimirović, S., Staveley-Smith, L., Jameson, K., Di Teodoro, E., Allison, J. R., Collier, J. D., Chippendale, A. P., Franzen, T., Gürkan, G., Heald, G., Hotan, A., Kleiner, D., Lee-Waddell, K., McConnell, D., Popping, A., Rhee, J., Riseley, C. J., Voronkov, M. A., & Whiting, M. 2018, *Nature Astronomy*, 2, 901
- McMillan, P. J. 2011, *MNRAS*, 414, 2446
- Miyamoto, M. & Nagai, R. 1975, *PASJ*, 27, 533
- Moster, B. P., Naab, T., & White, S. D. M. 2013, *MNRAS*, 428, 3121
- Murray, C. E., Peek, J. E. G., Di Teodoro, E. M., McClure-Griffiths, N. M., Dickey, J. M., & Dénes, H. 2019, *ApJ*, 887, 267
- Navarro, J. F., Frenk, C. S., & White, S. D. M. 1996, *ApJ*, 462, 563
- . 1997, *ApJ*, 490, 493
- Navarro, J. F., Ludlow, A., Springel, V., Wang, J., Vogelsberger, M., White, S. D. M., Jenkins, A., Frenk, C. S., & Helmi, A. 2010, *MNRAS*, 402, 21
- Nidever, D. L., Monachesi, A., Bell, E. F., Majewski, S. R., Muñoz, R. R., & Beaton, R. L. 2013, *ApJ*, 779, 145
- Nidever, D. L., Olsen, K., Choi, Y., de Boer, T. J. L., Blum, R. D., Bell, E. F., Zaritsky, D., Martin, N. F., Saha, A., Conn, B. C., Besla, G., van der Marel, R. P., Noel, N. E. D., Monachesi, A., Stringfellow, G. S., Massana, P., Cioni, M.-R. L., Gallart, C., Monelli, M., Martinez-Delgado, D., Munoz, R. R., Majewski, S. R., Vivas, A. K., Walker, A. R., Kaleida, C., & Chu, Y.-H. 2018, *ArXiv e-prints*

- Niederhofer, F., Cioni, M.-R. L., Rubele, S., Schmidt, T., Bekki, K., Grijs, R. d., Emerson, J., Ivanov, V. D., Marconi, M., Oliveira, J. M., Petr-Gotzens, M. G., Ripepi, V., van Loon, J. T., & Zaggia, S. 2018, *A&A*, 613, L8
- Noël, N. E. D., Conn, B. C., Carrera, R., Read, J. I., Rix, H.-W., & Dolphin, A. 2013, *ApJ*, 768, 109
- Noël, N. E. D., Conn, B. C., Read, J. I., Carrera, R., Dolphin, A., & Rix, H.-W. 2015, *MNRAS*, 452, 4222
- Oey, M. S., Dorigo Jones, J., Castro, N., Zivick, P., Besla, G., Januszewski, H. C., Moe, M., Kallivayalil, N., & Lennon, D. J. 2018, *ApJ*, 867, L8
- Olsen, K. A. G., Zaritsky, D., Blum, R. D., Boyer, M. L., & Gordon, K. D. 2011, *ApJ*, 737, 29
- Pardy, S. A., D'Onghia, E., Athanassoula, E., Wilcots, E. M., & Sheth, K. 2016, *ApJ*, 827, 149
- Pardy, S. A., D'Onghia, E., & Fox, A. J. 2018, *ArXiv e-prints*
- Patel, E., Besla, G., & Mandel, K. 2017, *MNRAS*, 468, 3428
- Pawlowski, M. S., Kroupa, P., & Jerjen, H. 2013, *MNRAS*, 435, 1928
- Pawlowski, M. S., Pflamm-Altenburg, J., & Kroupa, P. 2012, *MNRAS*, 423, 1109
- Peñarrubia, J., Gómez, F. A., Besla, G., Erkal, D., & Ma, Y.-Z. 2016, *MNRAS*, 456, L54
- Peñarrubia, J., Navarro, J. F., McConnachie, A. W., & Martin, N. F. 2009, *ApJ*, 698, 222

- Pedrerros, M. H., Anguita, C., & Maza, J. 2002, *AJ*, 123, 1971
- Piatek, S., Pryor, C., & Olszewski, E. W. 2008, *AJ*, 135, 1024
- Platais, I., van der Marel, R. P., Lennon, D. J., Anderson, J., Bellini, A., Sabbi, E., Sana, H., & Bedin, L. R. 2015, *AJ*, 150, 89
- Putman, M. E., Staveley-Smith, L., Freeman, K. C., Gibson, B. K., & Barnes, D. G. 2003, *ApJ*, 586, 170
- Ripepi, V., Cioni, M.-R. L., Moretti, M. I., Marconi, M., Bekki, K., Clementini, G., de Grijs, R., Emerson, J., Groenewegen, M. A. T., Ivanov, V. D., Molinaro, R., Muraveva, T., Oliveira, J. M., Piatti, A. E., Subramanian, S., & van Loon, J. T. 2017, *MNRAS*, 472, 808
- Růžička, A., Theis, C., & Palouš, J. 2010, *ApJ*, 725, 369
- Sales, L. V., Navarro, J. F., Cooper, A. P., White, S. D. M., Frenk, C. S., & Helmi, A. 2011, *MNRAS*, 418, 648
- Sales, L. V., Navarro, J. F., Kallivayalil, N., & Frenk, C. S. 2017, *MNRAS*, 465, 1879
- Sawala, T., Frenk, C. S., Fattahi, A., Navarro, J. F., Bower, R. G., Crain, R. A., Dalla Vecchia, C., Furlong, M., Helly, J. C., Jenkins, A., Oman, K. A., Schaller, M., Schaye, J., Theuns, T., Trayford, J., & White, S. D. M. 2016, *MNRAS*, 457, 1931
- Schlafly, E. F. & Finkbeiner, D. P. 2011, *ApJ*, 737, 103
- Schlegel, D. J., Finkbeiner, D. P., & Davis, M. 1998, *ApJ*, 500, 525
- Schmidt, T., Cioni, M.-R., Niederhofer, F., Diaz, J., & Matijevic, G. 2018, ArXiv e-prints

- Schönrich, R., Binney, J., & Dehnen, W. 2010, MNRAS, 403, 1829
- Sewilo, M., Carlson, L. R., Seale, J., Indebetouw, R., Meixner, M., Whitney, B., Robitaille, T. P., Oliveira, J. M., & Gordon, K. 2013, in Protostars and Planets VI Posters
- Sirianni, M., Jee, M. J., Benítez, N., Blakeslee, J. P., Martel, A. R., Meurer, G., Clampin, M., De Marchi, G., Ford, H. C., Gilliland, R., Hartig, G. F., Illingworth, G. D., Mack, J., & McCann, W. J. 2005, PASP, 117, 1049
- Skowron, D. M., Jacyszyn, A. M., Udalski, A., Szymański, M. K., Skowron, J., Poleski, R., Kozłowski, S., Kubiak, M., Pietrzyński, G., Soszyński, I., Mróz, P., Pietrukowicz, P., Ulaczyk, K., & Wyrzykowski, Ł. 2014, ApJ, 795, 108
- Sohn, S. T., Besla, G., van der Marel, R. P., Boylan-Kolchin, M., Majewski, S. R., & Bullock, J. S. 2013, ApJ, 768, 139
- Sohn, S. T., van der Marel, R. P., Carlin, J. L., Majewski, S. R., Kallivayalil, N., Law, D. R., Anderson, J., & Siegel, M. H. 2015, ApJ, 803, 56
- Sohn, S. T., van der Marel, R. P., Kallivayalil, N., Majewski, S. R., Besla, G., Carlin, J. L., Law, D. R., Siegel, M. H., & Anderson, J. 2016, ApJ, 833, 235
- Stanimirović, S., Staveley-Smith, L., & Jones, P. A. 2004, ApJ, 604, 176
- Subramanian, S. & Subramaniam, A. 2012, ApJ, 744, 128
- Tollerud, E. J., Boylan-Kolchin, M., & Bullock, J. S. 2014, MNRAS, 440, 3511
- van der Marel, R. P., Alves, D. R., Hardy, E., & Suntzeff, N. B. 2002, AJ, 124, 2639
- van der Marel, R. P. & Franx, M. 1993, ApJ, 407, 525

- van der Marel, R. P. & Kallivayalil, N. 2014, *ApJ*, 781, 121
- van der Marel, R. P., Kallivayalil, N., & Besla, G. 2009, in *IAU Symposium*, Vol. 256, *The Magellanic System: Stars, Gas, and Galaxies*, ed. J. T. Van Loon & J. M. Oliveira, 81–92
- van der Marel, R. P. & Sahlmann, J. 2016, *ApJ*, 832, L23
- Vera-Ciro, C. A., Helmi, A., Starkenburg, E., & Breddels, M. A. 2013, *MNRAS*, 428, 1696
- Vieira, K., Girard, T. M., van Altena, W. F., Zacharias, N., Casetti-Dinescu, D. I., Korchagin, V. I., Platais, I., Monet, D. G., López, C. E., Herrera, D., & Castillo, D. J. 2010, *AJ*, 140, 1934
- Wilson, J. C., Hearty, F. R., Skrutskie, M. F., Majewski, S. R., Holtzman, J. A., Eisenstein, D., Gunn, J., Blank, B., Henderson, C., Smee, S., Nelson, M., Nidever, D., Arns, J., Barkhouser, R., Barr, J., Beland, S., Bershady, M. A., Blanton, M. R., Brunner, S., Burton, A., Carey, L., Carr, M., Colque, J. P., Crane, J., Damke, G. J., Davidson, J. W., J., Dean, J., Di Mille, F., Don, K. W., Ebelke, G., Evans, M., Fitzgerald, G., Gillespie, B., Hall, M., Harding, A., Harding, P., Hammond, R., Hancock, D., Harrison, C., Hope, S., Horne, T., Karakla, J., Lam, C., Leger, F., MacDonald, N., Maseman, P., Matsunari, J., Melton, S., Mitcheltree, T., O'Brien, T., O'Connell, R. W., Patten, A., Richardson, W., Rieke, G., Rieke, M., Roman-Lopes, A., Schiavon, R. P., Sobek, J. S., Stolberg, T., Stoll, R., Tembe, M., Trujillo, J. D., Uomoto, A., Vernieri, M., Walker, E., Weinberg, D. H., Young, E., Anthony-Brumfield, B., Bizyaev, D., Breslauer, B., De Lee, N., Downey, J., Halverson, S., Huehnerhoff, J., Klaene, M., Leon, E., Long, D., Mahadevan, S., Malanushenko, E., Nguyen, D. C., Owen, R., Sánchez-Gallego, J. R., Sayres, C.,

- Shane, N., Sheckman, S. A., Shetrone, M., Skinner, D., Stauffer, F., & Zhao, B. 2019, *PASP*, 131, 055001
- Yoshizawa, A. M. & Noguchi, M. 2003, *MNRAS*, 339, 1135
- Yozin, C. & Bekki, K. 2015, *MNRAS*, 453, 2302
- Zivick, P., Kallivayalil, N., Besla, G., Sohn, S. T., van der Marel, R. P., del Pino, A., Linden, S. T., Fritz, T. K., & Anderson, J. 2019, *ApJ*, 874, 78
- Zivick, P., Kallivayalil, N., & van der Marel, R. P. in prep.
- Zivick, P., Kallivayalil, N., van der Marel, R. P., Besla, G., Linden, S. T., Kozłowski, S., Fritz, T. K., Kochanek, C. S., Anderson, J., Sohn, S. T., Geha, M. C., & Alcock, C. R. 2018, *ApJ*, 864, 55